

QUANTITATIVE MR T1 MEASUREMENTS WITH TOWERS: T-ONE WITH ENHANCED  
ROBUSTNESS AND SPEED

Cihat Eldeniz

A dissertation submitted to the faculty at the University of North Carolina at Chapel Hill in partial fulfillment of the requirements for the degree of Doctor of Philosophy in the Department of Biomedical Engineering in the School of Medicine.

Chapel Hill  
2014

Approved by:

Weili Lin

Hongyu An

Dinggang Shen

David S. Lalush

Hongtu Zhu

© 2014  
Cihat Eldeniz  
ALL RIGHTS RESERVED

## ABSTRACT

Cihat Eldeniz: Quantitative MR T1 Measurements With  
TOWERS: T-One With Enhanced Robustness And Speed  
(Under the direction of Weili Lin and Hongyu An)

T1 mapping can be beneficial for many applications in magnetic resonance imaging. Such applications include sequence optimization, clinical utility and tissue segmentation. However, the methods in the T1 mapping literature proposed to date either take a great deal of time to acquire or suffer from fundamental shortcomings. In addition, if significant motion occurs even once early in the scan, the operator needs to rerun the sequence, which is costly and time-consuming. Therefore, it is desirable to design a sequence that is not only fast, but also reliable to yield a good-quality T1 map, even in the presence of motion. In this study, we propose an EPI-based sequence with an efficient slice reordering scheme introduced relatively recently. The proposed sequence acquires saturation recovery samples that not only help improve estimation accuracy, but also serve as references for estimating motion parameters that will be used for mitigating the effects of motion. Furthermore, the reconstruction parameters are updated in the middle and at the end of the scan, and are used to retrospectively correct for motion. Phantom and *in vivo* experiments show the promise of the method.

To my mother, Aybegül Eldeniz,  
and  
to my father, Atik Eldeniz

## ACKNOWLEDGEMENTS

First of all, I would like to thank Dr. Weili Lin who supported me for years, provided an extremely productive environment with tons of resources, especially MR scanners, and made key suggestions that made my study stand on firmer ground.

Making research is like walking in a virgin forest. Quite strange and unexpected problems are not uncommon. Once these unprecedented problems get resolved, however, they lead to substantial progress. In this respect, I would like to thank my co-advisor Dr. Hongyu An for her tremendous support. She discussed with me every single problem I encountered and made solid suggestions that could eventually lead to a solution.

I would like to thank Dr. David Lalush as well, who critically revised my dissertation as more of an advisor rather than a committee member. My dissertation looked more like a dissertation after implementing his suggestions and answering his well-thought questions.

I would also like to thank two other faculty members that were in my committee: Dr. Dinggang Shen and Dr. Hongtu Zhu. They asked me very good questions, especially during my defense. Some of these questions helped reveal the utility of this PhD work while some of them helped uncover some crucial implementation details.

About two years ago, Dr. Jürgen Finsterbusch of Institut für Systemische Neurowissenschaften Universitätsklinikum Hamburg-Eppendorf developed a technique and that technique has been used in this study while dealing with subject motion. While trying to reproduce his solution, Dr. Finsterbusch did his best to help me, for which I am grateful.

I had many labmates who directly or indirectly contributed to this work. Dr. Yasheng Chen helped me in ways that I cannot forget. Li Wang and Yaozong Gao were perhaps the most frequent volunteers for my experiments. True Price gave me the most fantastic motion data set, which let me show that the proposed scheme can work even in the case of very-large-scale motion. I am thankful to numerous other volunteers who include Xiaodong Zhang, Qian Wang, Carlos Hernández, Chong Yaw Wee, KimHan Thung, Pei Zhang, Yuai Hua, Chunjun Qian, Shaoyi Du, Xiaopeng Zong, Hongyang Yuan, Bo Li, Heung-Il Suk, Daihui Peng, Rohit Kumar Gupta, Huynh Van Luong and Yu Ming. I would also like to thank Bryant Mersereau, Meher Juttukonda, Chris Pecora, Jason Brown, Sarael Alcauter-Solórzano, Gerard Sanroma and Guorong Wu for the contributions they made while I was practicing for the defense. In addition, I am grateful to Jeremy Boomhower for the editorial corrections.

90% of success is morale. In this respect, I would like to acknowledge my family, relatives, friends and many other precious people who bring happiness to my life.

## TABLE OF CONTENTS

LIST OF TABLES .....	x
LIST OF FIGURES .....	xi
LIST OF ABBREVIATIONS AND SYMBOLS .....	xvi
CHAPTER 1: INTRODUCTION .....	1
CHAPTER 2: MR BASICS .....	3
2.1 Introduction to MRI .....	3
2.2 Image Acquisition .....	8
2.3 Partial Fourier Acquisition .....	12
2.4 Parallel Imaging .....	12
CHAPTER 3: BACKGROUND AND LITERATURE REVIEW .....	16
3.1 Underlying Physical Principles .....	16
3.2 Applications of $T_1$ Measurement .....	17
3.3 Inversion Recovery: The Gold Standard .....	18
3.4 Progressive Saturation .....	19
3.5 Two-point Methods .....	20
3.6 Look-Locker .....	20
3.7 Slice Reordering Methods .....	21
CHAPTER 4: DESIGN AND DEVELOPMENT .....	22
4.1 Design Objective .....	22
4.2 Data Collection Scheme .....	22
4.3 Design trade-offs .....	26

4.4 More on the usefulness of SR repetitions .....	27
CHAPTER 5: T <sub>1</sub> MAPPING .....	34
5.1 Weighted least-squares (WLS) .....	34
5.2 Ordinary least-squares (OLS) .....	37
5.3 Comparison of WLS and OLS .....	40
5.4 Comparison with the gold standard in phantom .....	42
5.5 Comparison with the gold standard <i>in vivo</i> .....	45
5.6 Reproducibility .....	49
CHAPTER 6: MOTION .....	51
6.1 Effects of motion .....	57
6.2 Redoing the GRAPPA calibration .....	52
6.3 Importance of the retrospective approach .....	52
6.4 Usefulness of the SR repetitions .....	53
6.5 Saving the calibration data .....	53
6.6 Semi-automatic motion detection .....	54
6.7 Retrospective reconstruction: An example .....	56
6.8 Motion relocates spins .....	64
6.9 Spin tracking .....	64
6.10 Experiments .....	68
6.11 Sub-voxel smoothing .....	80
CHAPTER 7: SUMMARY AND CONCLUSION .....	88
7.1 Major contributions.....	88
7.2 Clinical applications.....	90

7.3 Limitations .....	92
7.4 Future work.....	94
REFERENCES .....	95

## LIST OF TABLES

Table 6.1 – Estimated motion parameters for the cases to be presented .....	69
Table 6.2 – T1 measurements in white matter .....	86
Table 6.3 – T1 measurements in putamen .....	86
Table 6.4 – T1 measurements in thalamus.....	86
Table 6.5 – T1 measurements in caudate.....	87
Table 6.6 – T1 measurements in cerebrospinal fluid.....	87

## LIST OF FIGURES

Figure 2.1 – Spins before and after the application of the external magnetic field  $B_0$ . The black arrows pointing upward in the “AFTER” image show the parallel spins whereas those pointing downward show the anti-parallel spins.  $M_0$  is the resulting net magnetization.....3

Figure 2.2 – Trajectory of the net magnetization vector as it is being tipped by 90 degrees away from the z-axis. Each cycle around the z-axis along the spiral trajectory is completed within one Larmour period which can be expressed as  $T_0 = 2\pi/\omega_0$ .....5

Figure 2.3 – The tipping of the magnetization in the rotating reference frame .....7

Figure 2.4 – Longitudinal and transverse components of magnetization .....7

Figure 2.5 – Illustration of k-space line acquisition for a gradient echo sequence. The area under each waveform was indicated for convenience. The green dashed line marks the time at which  $k_x = 0$ . The red asterisks mark the sampling times.  $k_x$  takes negative values at the points to the left of the dashed line.....10

Figure 2.6 – EPI sequence structure. The green dashed line marks the time at which  $k_x = k_y = 0$ , the center of k-space .....11

Figure 2.7 – Illustration of GRAPPA reconstruction.....14

Figure 2.8 – Illustration of GRAPPA calibration .....15

Figure 4.1 – Slice reordering scheme for 4 slices only (for the sake of simplicity). INV indicates the non-slice-selective inversion pulse applied at the beginning of every repetition that inverts the magnetization of all slices. This scheme allows each of the 4 slices to be sampled at each of the 4 possible effective inversion times (TI). If the repetition time (TR) is short, it is clear that this acquisition will take a very short time.....23

Figure 4.2 – Basic slice reordering scheme. Slices are circularly shifted by 4 within each section while a circular shift of 2 takes place while transitioning from Section 1 to Section 2.....24

Figure 4.3 – Inversion and saturation recovery processes as a function of time for  $T1 = 1650$  ms. Note the intensity difference between the IR and the SR samples at the same time point, namely 4000 ms, that makes the SR sample valuable for estimation.....25

Figure 4.4 – Overall acquisition scheme.....	26
Figure 4.5 – EPI phase correction fails when some tissues are within the negative portion of the inversion recovery process .....	29
Figure 4.6 – The in-house reconstruction module successfully overcomes the problem shown in Figure 4.5.....	29
Figure 4.7 – SR repetition images (Slices 1-24) when an inversion pulse is placed before the GRAPPA calibration scan. The red arrows indicate the artifacts due to GRAPPA failure caused by poor calibration data .....	31
Figure 4.8 – The IR repetition right after the first SR repetition. This repetition closely represents the situation in the GRAPPA calibration repetition. Low-signal slices experience GRAPPA failure as shown by Figure 4.7.....	32
Figure 4.9 – SR repetition images when no inversion pulse is placed before the GRAPPA calibration scan. GRAPPA calibration data is now high-SNR for all slices.....	33
Figure 5.1 – Various phases of inversion recovery for a middle slice which clearly shows the putamen going through intensity variations .....	38
Figure 5.2 – Average SNR in the putamen as a function of sequence repetitions. The red band shows the SNR range for which the Gaussianity assumption is invalid.....	39
Figure 5.3 – Average $T_1$ values as measured by WLS and OLS with error bars. Because the standard deviations are small, the error bars are barely visible.....	40
Figure 5.4 – Histograms of $T_1$ values as measured by WLS and OLS. The distribution of the WLS values shows a very slight shift towards right .....	41
Figure 5.5 – Structure of the proposed sequence .....	43
Figure 5.6 – Means and standard deviations for the gold standard IR method and the proposed method .....	44
Figure 5.7 – Bland-Altman plot .....	44
Figure 5.8 – Comparison of the $T_1$ values obtained by the proposed method (right column) with those obtained by the gold standard method (left column). The values are in milliseconds .....	46

Figure 5.9 – Comparison of the $T_1$ values obtained by the proposed method with those obtained by the gold standard method across four subjects and in four anatomical regions .....	47
Figure 5.10 – Correlation between the $T_1$ values obtained by the proposed method with those obtained by the gold standard method across four subjects and in four anatomical regions .....	47
Figure 5.11 – Demonstration of the effect of lengthening the repetition time of the sequence in one of the subjects.....	48
Figure 5.12 – Coefficients of variation across four identical scans .....	50
Figure 6.1 – Overall acquisition scheme.....	53
Figure 6.2 – Retrospective reconstruction in the presence of motion. Arrows show to which IR repetitions a given set of calibration data is applied. Hands represent the High5 slices. The change of position is indicated by the change in the orientation of the hands .....	56
Figure 6.3 – A motion-corrupted data set. Red squares indicate the SR repetitions where the GRAPPA coefficients are being calculated and updated. ....	57
Figure 6.4 – Correlations with the first SR repetition.....	58
Figure 6.5 – Correlations with the second SR repetition .....	58
Figure 6.6 – Correlations with the third SR repetition .....	59
Figure 6.7 – The data set in Figure 6.3 after retrospective reconstruction .....	60
Figure 6.8 – Comparison at 13 <sup>th</sup> image. The dashed orange line helps notice the shift of location .....	60
Figure 6.9 – Original (left) and retrospectively-reconstructed (right) images. The red arrows indicate the reconstruction artifacts.....	62
Figure 6.10 – Original (left) and retrospectively-reconstructed (right) images. The red arrows indicate the reconstruction artifacts.....	63
Figure 6.11 – Three consecutively-acquired slices from the retrospectively-reconstructed data set.....	63
Figure 6.12 – Change of slice location as a result of motion. The bright cyan spot represents a spin on Slice 4 that gets relocated onto Slice 5 after motion. For ease of demonstration, the slices were drawn much thicker than they actually are. ....	65

Figure 6.13 – The magnetization pathways of a spin on two neighboring slices, namely Slices 40 and 41 .....	65
Figure 6.14 – Demonstration of spin relocation due to motion. A, B and C represent three spins on the same slice that get relocated on different slices after the subject moves once before and once after the second SR repetition. ....	66
Figure 6.15 – Same spins as in Figure 6.14 with an alternative demonstration where the focus is slice relocation. After the first motion, the slice locations for A, B and C respectively become 30, 32 and 34. And after the second motion, the slice locations become 31, 32 and 33 in respective order. ....	67
Figure 6.16 – Magnetization pathways for Spin A that was introduced in Figure 6.14 .....	68
Figure 6.17 – Slice 29 across all repetitions .....	69
Figure 6.18 – High5 correlations with SRs across all repetitions .....	70
Figure 6.19 – $T_1$ maps computed using the original (top) and motion-corrupted (bottom) data sets .....	71
Figure 6.20 – A sample slice showing the banded pattern due to motion .....	71
Figure 6.21 – Slice 31 across all repetitions .....	72
Figure 6.22 – High5 correlations with SRs across all repetitions .....	73
Figure 6.23 – $T_1$ maps computed using the original (top) and motion-corrupted (bottom) data sets .....	73
Figure 6.24 – Comparison of the $T_1$ maps computed using the original (left) and motion-corrupted (right) data sets. A single slice is shown for better visualization .....	74
Figure 6.25 – Cost functions for a well-behaved voxel (left) and a noise-like voxel (right). The fitting algorithm converged to the points indicated by the red asterisks.....	74
Figure 6.26 – Slice 31 across all repetitions .....	75
Figure 6.27 – High5 correlations with SRs across all repetitions .....	75
Figure 6.28 – $T_1$ maps computed using the original (top) and motion-corrupted (bottom) data sets .....	76

Figure 6.29 – Comparison of the $T_1$ maps computed using the original (left) and motion-corrupted (right) data sets. A single slice is shown for better visualization. ....	76
Figure 6.30 – Slice 31 across all repetitions .....	77
Figure 6.31 – High5 correlations with SRs across all repetitions .....	78
Figure 6.32 – High5 correlations with a different display window .....	78
Figure 6.33 – $T_1$ maps computed using the original (top) and motion-corrupted (bottom) data sets .....	79
Figure 6.34 – A sample slice showing the banded pattern due to motion. The banding in this case is in two different directions .....	79
Figure 6.35 – Lattice configurations for a single spin (a), for $3 \times 3 \times 3 = 27$ spins (b) and for $5 \times 5 \times 5 = 125$ spins (c) .....	81
Figure 6.36 – Redistribution of same-voxel spins into 6 different voxels in 2 different slices after motion .....	82
Figure 6.37 – Case 1: Motion-free (left), Motion-corrupted with $N_{Spins}=1$ (middle), Motion-corrupted with $N_{Spins}=3$ (right) .....	83
Figure 6.38 – Case 2: Motion-free (left), Motion-corrupted with $N_{Spins}=1$ (middle), Motion-corrupted with $N_{Spins}=3$ (right) .....	83
Figure 6.39 – Case 3: Motion-free (left), Motion-corrupted with $N_{Spins}=1$ (middle), Motion-corrupted with $N_{Spins}=3$ (right) .....	84
Figure 6.40 – Case 4: Motion-free (left), Motion-corrupted with $N_{Spins}=1$ (middle), Motion-corrupted with $N_{Spins}=3$ (right) .....	84
Figure 6.41 – Case 1: Motion-corrupted with $N_{Spins}=3$ (left), Motion-corrupted with $N_{Spins}=5$ (right) .....	85
Figure 6.42 – Computation times for Case 1: Motion-corrupted with $N_{Spins}=1$ (left), Motion-corrupted with $N_{Spins}=3$ (middle), Motion-corrupted with $N_{Spins}=5$ (right) .....	85
Figure 7.1 – Comparison of segmentation results. Green arrows: Cortical structures, Red arrows: Putamen, Cyan arrows: Thalamus .....	91
Figure 7.2 – Computation times for Case 1: Motion-corrupted with $N_{Spins}=1$ (left), Motion-corrupted .....	93

## LIST OF ABBREVIATIONS AND SYMBOLS

*	Complex conjugation operator
$\  \cdot \ _F$	Frobenius norm
$\mathbf{A}$	Vector of individual coil signals
$A$	Noise-free signal
$A_{\text{SOS}}$	Noise-free image reconstructed from individual coil images using the sum-of-squares method
$\beta$	Flip angle
$B_0$	Main magnetic field strength
$B_1$	Radiofrequency magnetic field
$\mathbf{C}$	Covariance matrix
$C$	Coil sensitivity
CV	Coefficient of variation
$dS(\vec{r}, t)$	Infinitesimal signal from a single spin as a function of space and time
EPI	Echo-planar imaging
FAST	FMRIB's Automated Segmentation Tool
FLIRT	FMRIB's Linear Image Registration Tool
FOV	Field of view
FSL	FMRIB Software Library
$\vec{\mathbf{G}}$	Gradient field vector
GB	Gigabyte
GRAPPA	Generalized autocalibrating partially parallel acquisitions
$G_x$	Gradient magnetic field along the $x$ axis

$G_y$	Gradient magnetic field along the $y$ axis
$\gamma$	Gyromagnetic ratio
High5	The five highest-intensity slices at any given repetition
I	Intensity
INV	Inversion
IR	Inversion recovery
$I_{\text{SOS}}$	Noisy image reconstructed from individual coil images using the sum-of-squares method
$J_{\text{OLS}}$	Cost function to be minimized during ordinary least-squares fitting
$J_{\text{WLS}}$	Cost function to be minimized during weighted least-squares fitting
K	Number of individual coil elements
$\vec{k}$	Spatial frequency vector
$k_x$	Spatial frequency along the $x$ axis
$k_y$	Spatial frequency along the $y$ axis
MB	Megabyte
$M_0$	Effective magnetization
MR	Magnetic resonance
MRI	Magnetic resonance imaging
$M_{x'y'}$	Transverse magnetization in the rotating reference frame
$M_z$	Longitudinal magnetization
$n$	Noise
N	Number of data points to be used during curve-fitting
$N_c$	Number of receiver coils
$N_{\text{spins}}$	Hypothesized number of spins in a voxel

$N_{SpinsPerDim}$	Hypothesized number of spins along each of the three axes
OLS	Ordinary least-squares
$\omega$	Precessional angular frequency
$\omega_o$	Larmor frequency
PE	Phase encoding
R	Parallel imaging acceleration factor
ROI	Region of interest
$\vec{r}$	Position vector
$\rho$	Spin density
RF	Radiofrequency
$S(t)$	Received signal as a function of time
$S(\vec{k})$	Received signal as a function of spatial frequency
SENSE	Sensitivity encoding
SNR	Signal-to-noise ratio
SOS	Sum-of-squares
SR	Saturation recovery
$T_1$	Longitudinal relaxation time
$T_2$	Transverse relaxation time
$T_2^*$	Transverse relaxation time in the presence of field inhomogeneity
TE	Echo time
TI	Inversion time
$TI_{prev}$	Inversion time for the previous sequence repetition
$T_o$	Larmor period

TR	Repetition time
$t$	time
tr(.)	Trace operation, or equivalently, sum of diagonal elements
WLS	Weighted least-squares

## CHAPTER 1: INTRODUCTION

Magnetic resonance imaging (MRI) is in ubiquitous use today. Although it is difficult to enumerate the imaging techniques currently being used in research centers and hospitals, all of these techniques rely upon the very basic parameters discovered in the early days of nuclear magnetic resonance. Therefore, the quantification of these parameters will always be important no matter towards which direction MR research will proceed. This study is aiming at quantifying one such fundamental parameter –  $T_1$ , the longitudinal relaxation time.

Having accurate measurements of  $T_1$  can serve many purposes ranging from sequence optimization to clinical use and from temperature measurements to tissue segmentation. Currently, the methods for mapping  $T_1$  throughout the whole brain stand on a balance point between accuracy and acquisition time. Nevertheless, to the best of our knowledge, no group has specifically dealt with motion. Thus, should significant motion occur during the MR scan, the sequence needs to be rerun from the beginning.

In this study, we propose an EPI-based sequence with an efficient slice reordering scheme introduced relatively recently. When the acquisition is high-speed, the dynamic range of the experiment and hence the accuracy is reduced because the system is never allowed to get back to equilibrium. As a remedy to this problem, the proposed sequence acquires equilibrium-like samples. Interestingly, these samples also serve as references for estimating motion parameters. Moreover, the segmented structure of the proposed scheme allows for the

updating of the reconstruction parameters which can be used retrospectively to correct for motion.

This dissertation is organized as follows: Chapter 2 covers the MR basics. Chapter 3 reviews the existing methods in the  $T_1$  mapping literature. Chapter 4 discusses the design decisions and the trade-offs involved. Chapter 5 details the estimation procedure. Chapter 6 handles motion in depth. Finally, Chapter 7 provides a summary, discusses the limitations and indicates future research directions.

## CHAPTER 2: MR BASICS

### 2.1 Introduction to MRI

Nuclei have electrical charges and rotate about their own axes. This leads to the so-called *magnetic moment*, a physical vector quantity whose magnitude is proportional to the angular momentum with the proportionality constant being dependent on the type of nucleus (1). The direction of the magnetic moment is along the axis of rotation and follows the thumb of the right hand when the other four fingers follow the direction of rotation. When no external magnetic field exists, each individual spin in a volume of interest will have a random orientation. If, on the other hand, an external magnetic field,  $B_0$ , is applied, the spins will now align with this field; either in a parallel manner or in an anti-parallel manner. Figure 2.1 depicts this phenomenon.

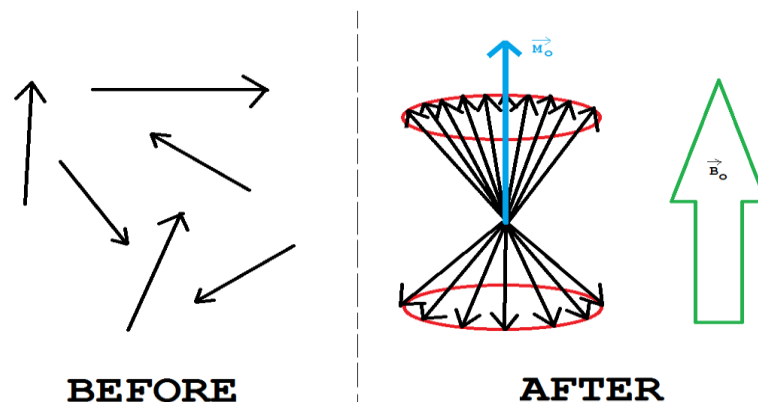


Figure 2.1 – Spins before and after the application of the external magnetic field  $B_0$ . The black arrows pointing upward in the “AFTER” image show the parallel spins whereas those pointing downward show the anti-parallel spins.  $M_0$  is the resulting net magnetization.

The spins are going to *precess* about the magnetic field in a clockwise direction. That is, they are not only going to rotate around themselves, but they will also rotate about the external magnetic field. The trajectory of this second rotation is indicated with the two red circles in Figure 2.1 and the angular frequency of rotation is given by the Larmour equation:

$$\omega_o = \gamma B_o \quad (2.1)$$

where  $\gamma$  is the *gyromagnetic ratio*, which is nucleus-specific and has the units of *radians/second/Tesla*. The spins aligned parallelly will be slightly larger in number, yielding a *net magnetization* vector,  $M_o$ , along the direction of the main magnetic field.

The spins aligned anti-parallelly with the external magnetic field, that is, the ones pointing downward on the right-hand side of Figure 2.1, possess higher potential energy than those aligned parallelly. This means that, if it is desired to have the net magnetization point in a different direction, say in the direction exactly opposite to the external magnetic field, energy should be injected into the system so that the low-energy parallel spins shall switch to the high-energy state and the number of the anti-parallel spins shall exceed the number of parallel spins. For the sake of simplicity, the rest of the discussion is going to be centered on the net magnetization, rather than the state of individual spins. Also, without loss of generality, the main magnetic field,  $B_o$ , is assumed to point in the direction of the positive  $z$ -axis.

The net equilibrium magnetization along  $z$ ,  $M_o$ , manifests no detectable change. In order to make measurements, however, a changing magnetic flux is needed (2). This is accomplished by tipping  $M_o$  away from  $z$  by injecting energy into the system; in which case, the magnetization begins to rotate around  $z$ , inducing a changing flux and hence a detectable

signal in the receiver coil(s). In order for the magnetization to be tipped away from the  $z$ -axis by a desired angle, the energy injection should be performed via a radiofrequency (RF) pulse whose frequency is matched to the Larmour frequency. Otherwise, the tipping will not be effective (2). This matching condition is known as the *on-resonance condition* and gives MRI its name: *magnetic resonance imaging*. Figure 2.2 demonstrates what the trajectory of the magnetization would look like during this process in the fixed laboratory frame of reference.

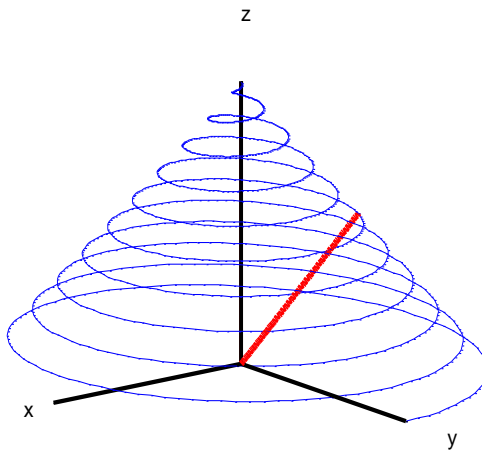


Figure 2.2 – Trajectory of the net magnetization vector as it is being tipped by 90 degrees away from the  $z$ -axis. Each cycle around the  $z$ -axis along the spiral trajectory is completed within one Larmour period which can be expressed as  $T_0 = 2\pi/\omega_0$ .

If a rotating frame of reference is chosen, the tipping process can be visualized in a much clearer way. Considering a frame of reference  $(x',y',z')$ , whose  $z'$ -axis coincides with the  $z$ -axis of the fixed reference frame and which rotates around the  $z$ -axis in a clockwise direction with the Larmour frequency, the spins visualized in this newly-defined rotating reference frame do not precess around the  $z'$ -axis. In addition, the RF field oscillating with

the Larmour frequency is stationary in this rotating reference frame and, thus, behaves as a constant magnetic field around which the net magnetization is going to rotate clockwise. Figure 2.3 plots the same tipping procedure as in Figure 2.2, but now in the rotating reference frame. The RF field along the  $x'$ -axis is usually denoted by  $B_1$ . Because the precession frequency depends on the magnetic field strength, due to the Larmour relation in Equation (2.1), how long the tipping will take depends on the  $B_1$  amplitude.

After any tipping procedure, the system of spins will try to get back to the original, low-energy equilibrium state where the net magnetization is  $M_0$  and points along the positive  $z$ -axis. This process is called *relaxation*. In order to analyze how relaxation occurs, we need to decompose the magnetization vector into two perpendicular components, as Figure 2.4 exhibits: the longitudinal component ( $M_{z'}$ ) and the transverse component ( $M_{x'y'}$ ).  $M_{z'}$  will relax back to  $M_0$  whereas  $M_{x'y'}$  will relax back to zero. It is clear that, by the end of the tipping procedure, the two components of magnetization will become  $M_{z'} = M_0 \cos(\beta)$  and  $M_{x'y'} = M_0 \sin(\beta)$ , where  $\beta$  is the flip angle.

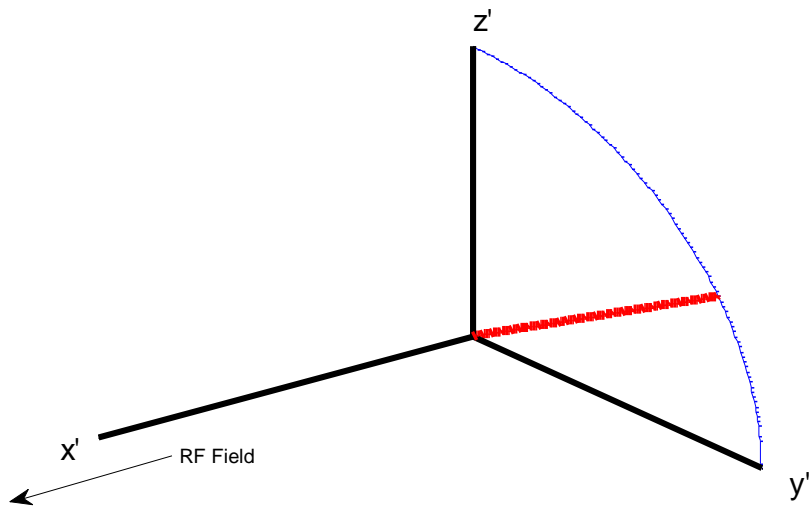


Figure 2.3 – The tipping of the magnetization in the rotating reference frame.

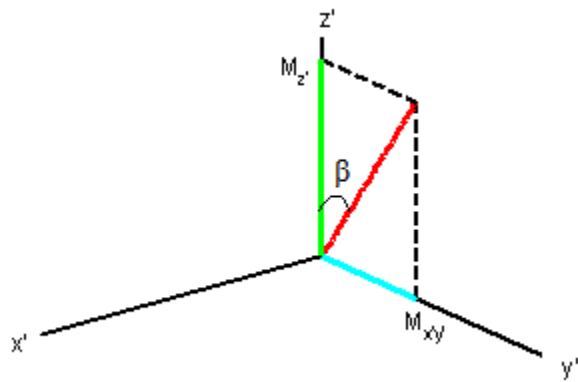


Figure 2.4 – Longitudinal and transverse components of magnetization.

The relaxation processes are governed by the following first-order differential equations (1):

$$\frac{dM_{z'}}{dt} = -\frac{M_{z'} - M_0}{T_1} \quad (2.2)$$

$$\frac{dM_{x'y'}}{dt} = -\frac{M_{x'y'}}{T_2} \quad (2.3)$$

where  $T_1$  is called *the longitudinal relaxation time* and  $T_2$  is called *the transverse relaxation time*. Due to the nature of the interactions behind the relaxation phenomena,  $T_1$  and  $T_2$  are also called, respectively, *the spin-lattice relaxation time* and *the spin-spin relaxation time*. In this study, it is  $T_1$  that is to be measured.

The solution of Equation (2.2) for an initial longitudinal magnetization value of

$$M_{z'}(0) = M_{z',0} = M_0 \cos(\beta)$$

is given by:

$$M_{z'}(t) = M_{z',0}e^{-t/T_1} + M_0(1 - e^{-t/T_1}) = M_0[1 - (1 - \cos(\beta))e^{-t/T_1}] \quad (2.4)$$

$\beta = 90^\circ$  and  $\beta = 180^\circ$  yield the two special cases encountered the most in the  $T_1$  measurement literature.

## 2.2 Image Acquisition

In the presence of a linear gradient field vector,  $\vec{G}$ , superimposed on the main magnetic field, a spatially varying precessional angular frequency is achieved:

$$\omega(\vec{r}) = \gamma(B_0 + \vec{G} \cdot \vec{r}) \quad (2.5)$$

In the rotating reference frame, the contribution of the main magnetic field can be dropped, yielding:

$$\omega(\vec{r}) = \gamma \vec{G} \cdot \vec{r} \quad (2.6)$$

This precessional angular frequency will determine the phase of the spins. If the spin density at  $\vec{r}$  is given by  $\rho(\vec{r})$ , the signal collected within an infinitesimal  $d\vec{r}$  is given by (1):

$$dS(\vec{r}, t) = \rho(\vec{r}) e^{-j\omega(\vec{r})t} d\vec{r} = \rho(\vec{r}) e^{-j\gamma(\vec{G} \cdot \vec{r})t} d\vec{r} \quad (2.7)$$

which leads to the following signal equation when integrated:

$$S(t) = \int \rho(\vec{r}) e^{-i\gamma(\vec{G} \cdot \vec{r})t} d\vec{r} = \int \rho(\vec{r}) e^{-j\vec{k} \cdot \vec{r}} d\vec{r} = S(\vec{k}) \quad (2.8)$$

where  $\vec{k}(t) = \gamma \vec{G} t$  is in units of *radians/meter* and hence denotes spatial angular frequency. Equation (2.8) clearly shows that  $\rho(\vec{r})$  and  $S(\vec{k})$  constitute a Fourier transform pair and that the measured signal is in the spatial angular frequency domain, or, equivalently, in the so-called *k-space*. After digitization and assuming a 2D image, the following discrete Fourier transform pair is obtained:

$$S[k_x, k_y] = \sum_{x=1}^{N_x} \sum_{y=1}^{N_y} \rho[x, y] e^{-j(k_x x + k_y y)} \quad (2.9)$$

$$\rho[x, y] = \frac{1}{N_x N_y} \sum_{k_x=1}^{N_x} \sum_{k_y=1}^{N_y} S[k_x, k_y] e^{j(k_x x + k_y y)} \quad (2.10)$$

Signal acquisition results in  $[k_x, k_y]$ , and an inverse 2D Fourier transform yields  $\rho[x, y]$ .

Since  $k$  is directly proportional to the time integral of the gradient waveform, one can use gradient lobes in any direction to achieve any desired  $k$  value to the extent that practical constraints permit. Figure 2.5 exhibits the gradient waveforms for the acquisition of a single row in the k-space table, or, in more simple and convenient terms, a single k-space line. Each line is acquired with an associated RF pulse. For gradient echo sequences of this type, the time it takes from the center of RF excitation to the center of the  $k_x = 0$  point is called *echo time* (TE).

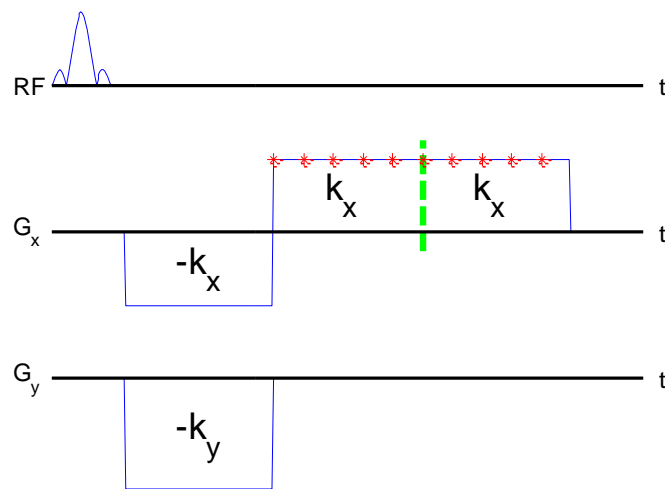


Figure 2.5 – Illustration of k-space line acquisition for a gradient echo sequence. The area under each waveform was indicated for convenience. The green dashed line marks the time at which  $k_x = 0$ . The red asterisks mark the sampling times.  $k_x$  takes negative values at the points to the left of the dashed line.

Echo-planar imaging (EPI) sequences, on the other hand, acquire all lines with a single RF excitation and, therefore, are very fast (3). As Figure 2.6 shows, the k-space lines are acquired one after the other with neighboring lines being traversed in opposite directions. In this case, TE is defined as the time between the center of the RF pulse and the origin of the

whole k-space,  $k_x = k_y = 0$ . Short TE values are desirable for accelerating image acquisition. In addition, the signals measured in the transverse plane have an exponential dependence on TE which may be expressed as  $e^{-TE/T_2^*}$  where  $T_2^*$  is the transverse relaxation time in the presence of field inhomogeneities and is smaller than  $T_2$ . Therefore, short TE values are desirable to avoid signal loss in the vicinity of the sinus cavity and the temporal bones where field inhomogeneity is an issue, due to the air-tissue interfaces.

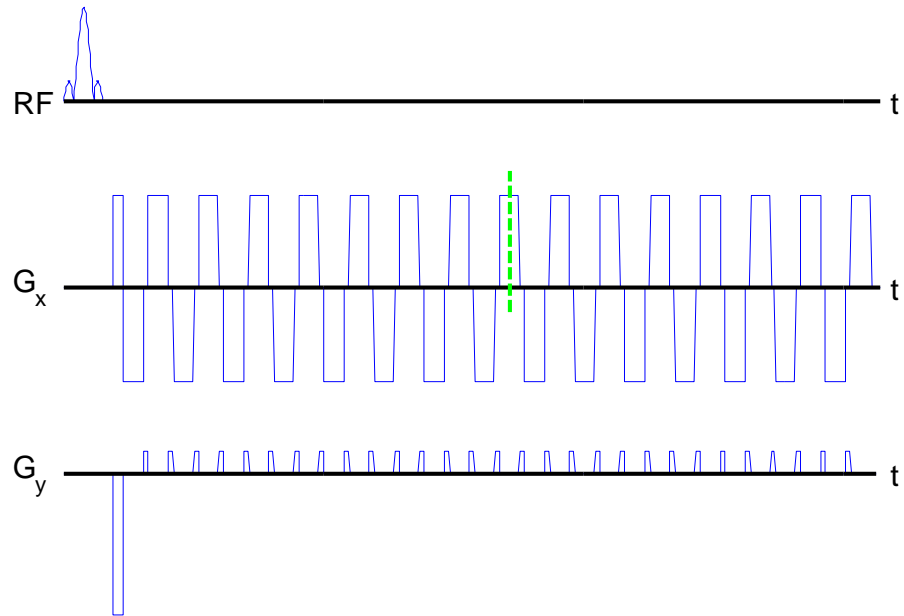


Figure 2.6 – EPI sequence structure. The green dashed line marks the time at which  $k_x = k_y = 0$ , the center of k-space.

### 2.3 Partial Fourier Acquisition

The k-space of a real image exhibits Hermitian symmetry. That is,

$$S(-k_x, -k_y) = S^*(k_x, k_y)$$

where  $*$  denotes complex conjugation. In this respect, it is possible to perfectly reconstruct a real image from only half of its k-space. However, k-space data acquired by MRI almost never exhibit such symmetry, due to a number of reasons, including resonance frequency offsets,  $B_1$ -field inhomogeneity, eddy currents, and hardware group delays (4). It is, therefore, necessary to acquire at least slightly more than half of the k-space data in order to deal with these problems.

The reconstruction algorithm commonly used is an iterative one where high-frequency content is used for estimating magnitude and low-frequency content is used for estimating phase (4). The missing portion of k-space is then filled with these new estimates and the iterations continue until a user-specified stopping criterion is satisfied.

In an EPI sequence, partial Fourier acquisition in the  $k_y$ -direction decreases the number of lines prior to the central line and, hence, decreases TE, the time to reach the k-space center, at the expense of the reduction in the amount of data being acquired, which leads to lower SNR in the resulting MR images.

### 2.4 Parallel Imaging

The main idea underlying data collection in k-space is spatial encoding, which is performed with the use of imaging gradients. However, it is also possible to accomplish part

of the spatial encoding through the use of multiple coils around the volume of interest. This is because each coil is more sensitive to the regions closer to it and, therefore, introduces its own spatial encoding. When the collection of all coils is considered, this makes it possible to skip some of the k-space lines, leading to an acceleration in data acquisition.

The field of MR imaging techniques that make use of this additional spatial encoding provided by different coils is referred to as parallel MR imaging (pMRI). Many pMRI methods have been proposed to date (4). pMRI can be implemented in the image domain, in the frequency domain or in both domains. Today, two methods are being widely used: Sensitivity encoding (SENSE) (5), an image domain method, and Generalized autocalibrating partially parallel acquisitions (GRAPPA) (6), a frequency domain method. Since GRAPPA is being utilized in this study, only this method is going to be briefly explained.

GRAPPA interpolates the missing lines in the k-space of each coil by linearly weighting the non-missing lines. However, the key point is that a missing line in a given coil is reconstructed not only by weighting the neighboring lines in the same coil, but also by weighting the same set of non-missing lines in the other coils as Figure 2.7 illustrates. The weighted sum of Lines  $a_7, a_9, a_{11}, a_{13}, b_7, b_9, \dots, d_{11}, d_{13}$  are being used to reconstruct a single line, namely Line  $a_{10}$  in Coil 1. A similar weighted sum operation is going to be performed for every single missing line in every single coil. However, in order to perform this operation, the weights need to be determined. Figure 2.8 demonstrates how this can be achieved. In this so-called *calibration scan*, the outer portion of k-space is skipped and the central portion is acquired. The central portion is preferred because the SNR in this portion is high and this helps more accurately estimate the weights. Line  $a_{10}$  and all other

lines in the central portion of all coils (shown in red in Figure 2.8) that are normally skipped are acquired during this calibration scan. This way, the reconstruction coefficients can be learned via an inverse problem and applied later during the actual imaging scans.

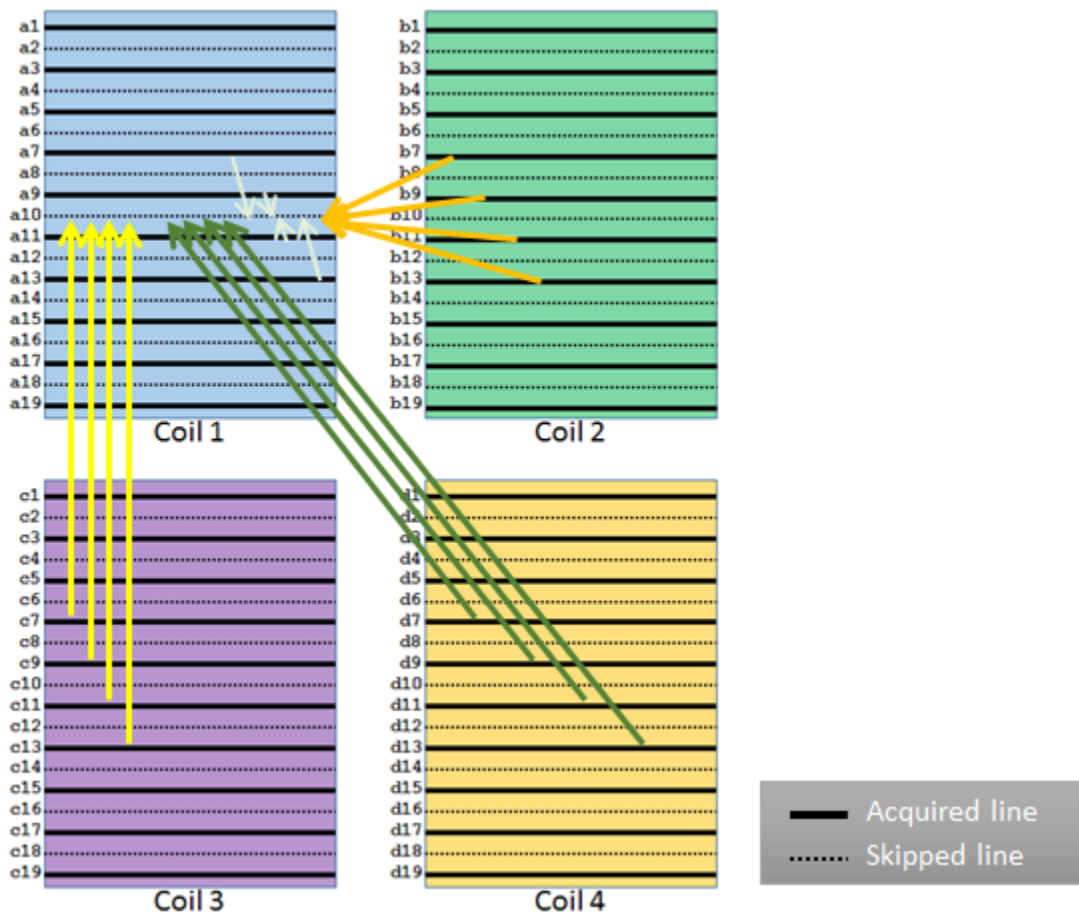


Figure 2.7 – Illustration of GRAPPA reconstruction.

By enabling the skipping of many k-space lines, the use of GRAPPA is going to decrease the number of lines to be acquired until the k-space center is reached and, thus, reduce TE. As an added benefit, the geometric distortion inherent to EPI sequences, due to the very low bandwidth along the phase encode direction, will also be alleviated with the

increased sampling bandwidth in the same direction. However, the SNR will decrease due to the reduction in the amount of data being acquired.

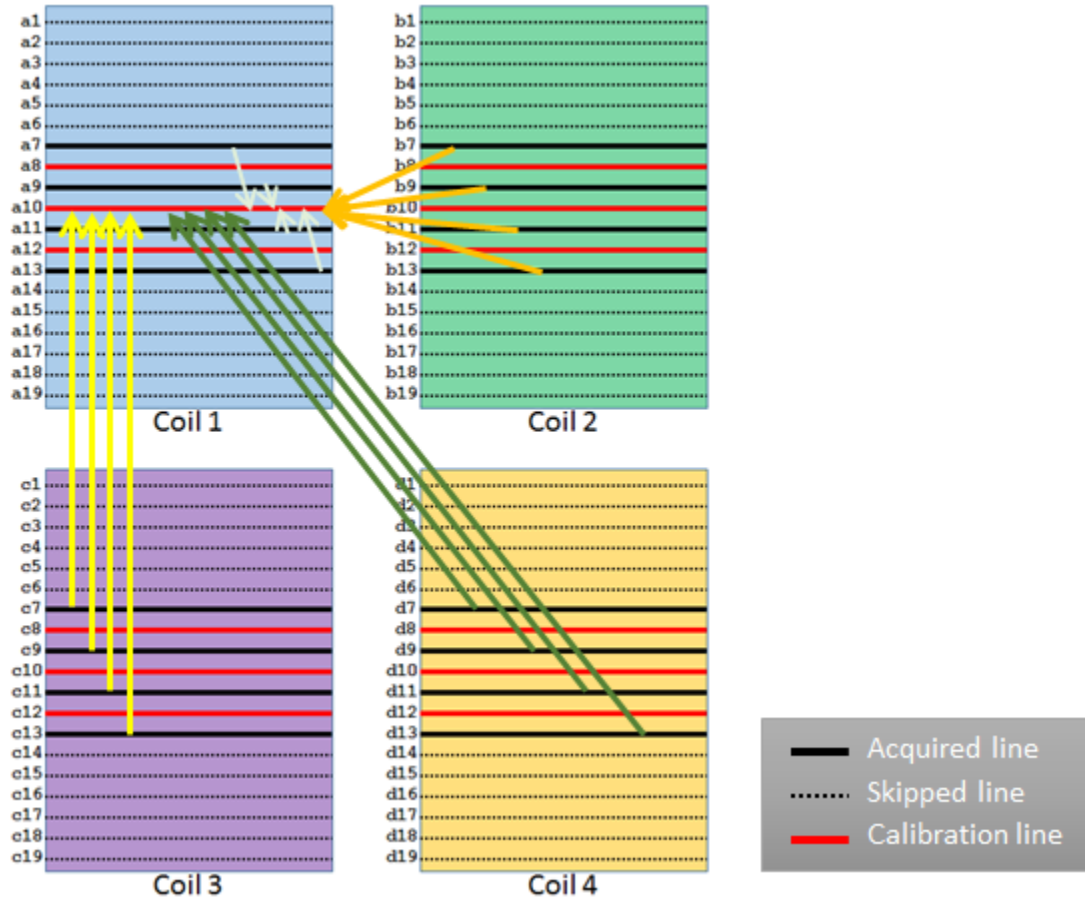


Figure 2.8 – Illustration of GRAPPA calibration

## CHAPTER 3: BACKGROUND AND LITERATURE REVIEW

### 3.1 Underlying Physical Principles

Longitudinal relaxation is one of the fundamental processes in MRI (1,2) and can be explained as follows. The strong magnetic field along the longitudinal axis of an MR machine causes MR-active nuclei, such as hydrogen nuclei, to become aligned and yield a net amount of magnetization in the same direction as the magnetic field. However, the receiver coils are sensitive only to the magnetization in the transverse direction. Therefore, a measurement can only be performed by tipping the net magnetization so as to have a transverse component. This can be achieved with the use of an excitatory RF pulse tuned to the Larmour frequency, whose value is proportional to the field strength. The resulting high-energy state is unstable. In order to reestablish stability, the energy injected into the system of protons, via the RF pulse, is given away to the surrounding molecules, *the lattice*. In other words, the spin system recovers back to its original equilibrium state through an energetic interaction with the surroundings. This recovery process is called *longitudinal relaxation*, *spin-lattice relaxation*, or *T<sub>1</sub> relaxation*, and is governed by the following first-order differential equation:

$$\frac{dM_z}{dt} = -\frac{M_z - M_o}{T_1} \quad (3.1)$$

where  $M_o$  is the net equilibrium magnetization,  $M_z$  is the magnetization along the longitudinal axis, and  $T_1$  is the *longitudinal relaxation time*.

The value of  $T_1$  depends on many factors, such as macromolecule concentration, water content, water binding, paramagnetic substance concentration, temperature, and the field strength of the MR machine (7,8). The larger the  $T_1$  value, the longer it takes the net magnetization to get back to equilibrium.

### **3.2 Applications of $T_1$ Measurement**

$T_1$  is a very fundamental parameter in MR and the measurement of  $T_1$  is, thus, vital for many MR applications. One such application is the measurement of the blood-brain barrier (BBB) permeability (7,9-11). Healthy BBB does not allow for the passage of the contrast agent to the intercellular space, but, if the BBB is broken, the contrast agent accumulates inside the tissue, causing a decrease in the apparent  $T_1$  value. In order to estimate the BBB leakage, the  $T_1$  map of the volume of interest is computed first. Later, a  $T_1$ -shortening contrast agent is injected into the subject and the effect on the signal is screened periodically. The permeability constant can then be obtained through a model equation that involves the baseline  $T_1$  value. The accuracy of the permeability constant estimate, therefore, strongly depends on the accuracy of the precontrast  $T_1$  map.

$T_1$  maps have also been used for diagnosis or to gauge the effectiveness of treatment for some diseases. Multiple sclerosis, intracranial tumors, epilepsy, stroke, dementia, schizophrenia, depression, Parkinson's disease, and acquired immunodeficiency syndrome (AIDS) are among such diseases (7). Because of the inconsistency regarding the  $T_1$  values reported by different clinical centers and because of the fact that significant overlap exists

between normal and diseased tissue  $T_1$  values, healthy vs. diseased tissue classification based on a single  $T_1$  map is not reliable (8,12). However, a longitudinal study of the  $T_1$  maps for a given patient imaged at a certain clinical center should provide information concerning the status of the disease.

Other applications of  $T_1$  mapping include temperature mapping (13-15), tissue segmentation (16,17), and suppression of signals coming from tissues that are not of interest (18,19).

### 3.3 Inversion Recovery: The Gold Standard

Numerous  $T_1$  mapping methods have been proposed in the literature. Among these methods, the inversion recovery (IR) sequence (20) remains the gold standard, due to the fact that it provides the highest possible dynamic temporal dynamic range for  $T_1$  recovery. In this sequence, the longitudinal magnetization is inverted by an RF pulse and, after a certain time period called the inversion time (TI), it is sampled by a second RF pulse that tips the magnetization to the transverse magnetization. Assuming that the first RF pulse yields perfect inversion, the differential equation given in Equation (3.1) can be solved for  $M_z$  with the initial condition  $M_z(0) = -M_o$ . Sampling  $M_z$  at  $t=TI$  yields:

$$M_z(T_1) = M_o \left( 1 - 2e^{-\frac{TI}{T_1}} \right) \quad (3.2)$$

The experiment is repeated for a set of TI values and the system of spins is set idle for at least five times the maximum  $T_1$  in the system after each measurement so that the equilibrium is practically restored by the beginning of the next measurement. The  $T_1$  value is then obtained through a least-squares fit to Equation (3.2). Although this scheme allows for a fairly good sampling of the recovery curve, the long acquisition time limits its use *in vivo*.

The fast inversion recovery (FIR) is a modified version of this gold standard where the repetition time (TR) of the sequence is kept much shorter (21). This version is certainly faster; however, high signal-to-noise ratio (SNR) requirements imposed by the desire to collect good-quality samples, places a lower limit on how short the TR can be made because the net magnetization cannot recover enough to yield high signal if the TR is too small, which in return limits the *in-vivo* use of this version as well.

### **3.4 Progressive Saturation**

The progressive saturation (PS) sequence (22) is a faster alternative where a comb of nullifying, rather than inverting, RF pulses is applied. The recovery begins with zero net magnetization each time and the measurement is performed after a steady state is established over the course a few repetitions. The sequence can be run with different TR values, yielding the required data for fitting a curve over the TR space. This scheme is fast, however, TR cannot be very short in a multi-slice acquisition, making it difficult to collect samples from the early phase of the recovery curve and, hence, imposing a lower limit on the minimum  $T_1$  that can be measured. In addition, the dynamic range of the PS sequence is much lower than that of the IR sequence, making it more prone to noise.

The variable flip angle (VFA) method (23) is a variation of the PS sequence where the experiment is repeated with a number of various flip angles rather than various repetition times. Although a set of images can be collected in only a few minutes with the use of a short TR value, this sequence is very sensitive to  $B_1$  field inhomogeneity.

### **3.5 Two-point Methods**

Two-point methods have also been proposed (24-26). Two PS images, two IR images, or one PS and one IR image can be divided into one another and a look up table can then be used to compute the  $T_1$  maps. The PS/IR pair has been shown to be the most optimal choice (27,28). Although these two-point methods require the acquisition of two images only, and, under certain conditions, can yield  $T_1$  maps that are comparable in quality to those obtained by multi-point FIR sequences, these methods can be very sensitive to systematic errors such as inversion profile imperfections (7,29,30).

Stimulated echo (STE) imaging (31,32) is yet another two-point method. Being a single-shot method, STE can yield two images in a single experiment. The fundamental building block of an STE sequence is an additional RF pulse that is used to store half of the magnetization along the longitudinal axis for later use. The STE method is fast, but suffers from poor signal-to-noise ratio (SNR) since only half of the magnetization leads to the stimulated echo.

### **3.6 Look-Locker**

Look-Locker (LL) sequences sample the longitudinal magnetization at various stages of  $T_1$  recovery via the use of low flip angles (33-39). However, LL sequences suffer from flip angle errors. Furthermore, the images collected with the use of low flip angles are low-SNR in nature and averaging is needed to establish a clinically acceptable level of SNR, which negate the advantage of fast acquisition. It is also worth noting that low flip angles reduce the dynamic range of the experiment, making the data more prone to noise.

### **3.7 Slice Reordering Methods**

Another class of sequences makes use of slice reordering (40-42). The slices of interest are inverted in groups and then sampled in an order that is circularly-shifted from repetition to repetition. This way, all slices are given the chance to be sampled at different phases of  $T_1$  recovery. During postprocessing, it is important to take into account the fact that the slices will never fully  $T_1$ -recover, especially if the TR is short.

## CHAPTER 4: DESIGN AND DEVELOPMENT

### 4.1 Design Objective

$T_1$  mapping is basically a curve-fitting problem. The relaxation process is sampled at various stages and the  $T_1$  value is then obtained through a fit to the model equation. Therefore, it is almost always beneficial to collect more samples to improve the quality of the estimates. However, time is a significant constraint.

In this study, the acquisition objective is to develop a sequence that can collect a high number of samples in only a few minutes while making sure that the samples being collected are of good quality.

### 4.2 Data Collection Scheme

Single-shot methods are well-suited for high-speed acquisition. These methods need only one RF excitation to collect all of the k-space data needed to reconstruct a single slice. Although spin-echo-based and gradient-echo-based sequences exist, the fastest possible option is the echo planar imaging, or EPI, and was described in Chapter 2.

In a conventional repeated MR acquisition, the order of slices being acquired is kept fixed across all repetitions of the sequence. However, changing the order of slices from repetition to repetition offers a unique opportunity to accelerate acquisition. The  $T_1$  mapping methods proposed in (40-42) are good examples for this kind of approach. Figure 4.1

illustrates this family of acquisitions. In this scheme, the order of slices is circularly shifted from repetition to repetition so that different slices have a chance to be sampled at different temporal locations with respect to the non-slice-selective inversion pulse. Defining the temporal distance of a given slice to the inversion pulse as the effective inversion time (TI), this scheme makes it possible for each slice to be sampled at all possible effective TI's if the slices are circularly shifted by 1, as in Figure 4.1.

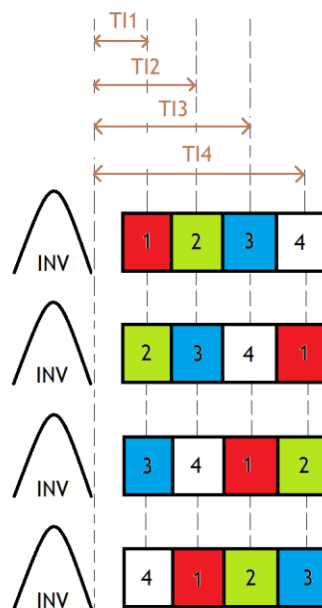


Figure 4.1 – Slice reordering scheme for 4 slices only (for the sake of simplicity). INV indicates the non-slice-selective inversion pulse applied at the beginning of every repetition that inverts the magnetization of all slices. This scheme allows each of the 4 slices to be sampled at each of the 4 possible effective inversion times (TI). If the repetition time (TR) is short, it is clear that this acquisition will take a very short time.

In our acquisition scheme, which typically involves 60 slices, we are deploying the same principle. Figure 4.2 shows the slice reordering scheme in this case. At each repetition, the slices are circularly shifted by 4, which is, in fact, a large amount of shift that limits the set of possible effective TI's to 15 per slice, but the complete acquisition of the volume is

performed twice with a shift of 2 slices in between. This way, 30 distinct effective TI's exist for all slices.

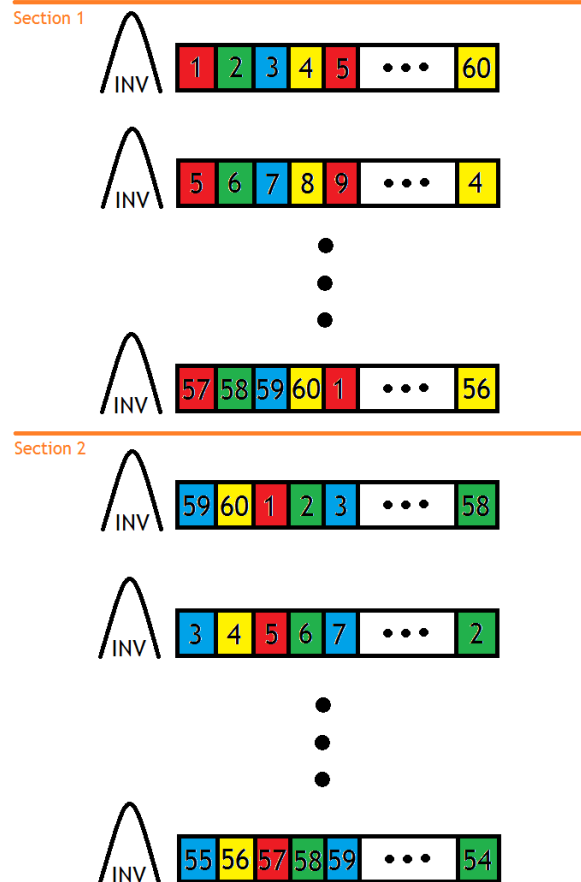


Figure 4.2 – Basic slice reordering scheme. Slices are circularly shifted by 4 within each section while a circular shift of 2 takes place while transitioning from Section 1 to Section 2.

A rapid sequence requires a short repetition time. It is clear that a short repetition time imposes a natural limit on how large the maximum effective TI can be, and this constraint decreases the dynamic range of the samples collected, making the estimation more prone to noise. In this respect, in addition to the inversion recovery (IR) repetitions depicted in Figure 4.2 that include an inversion pulse, it is beneficial to place at the beginning of each section

one saturation recovery (SR) measurement that does not include an inversion pulse. Figure 4.3 exhibits that a higher signal intensity value is obtained by SR.

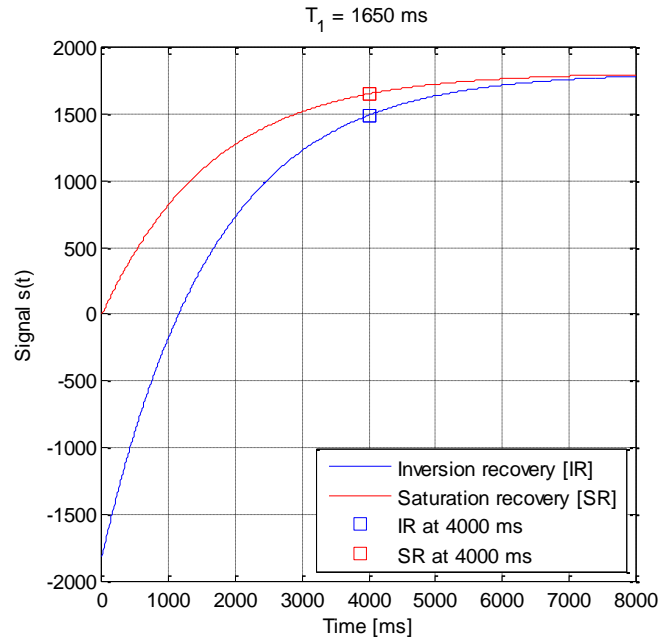


Figure 4.3 – Inversion and saturation recovery processes as a function of time for  $T_1 = 1650$  ms. Note the intensity difference between the IR and the SR samples at the same time point, namely 4000 ms, that makes the SR sample valuable for estimation

In Chapter 5, the experimental results will show that these SR samples alleviate the underestimation problem. However, the SR samples are going to find their actual use in dealing with motion, as to be described in Chapter 6, where it will be shown that the addition of the third SR repetition is very useful for artifact reduction purposes. Figure 4.4 demonstrates the final sequence diagram after incorporating the SR repetitions.

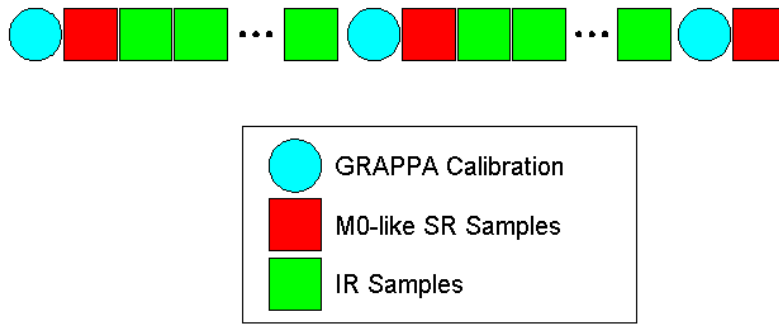


Figure 4.4 – Overall acquisition scheme

### 4.3 Design trade-offs

Although EPI offers fast acquisition, it suffers from a number of drawbacks. Firstly, the sampling bandwidth along the phase encoding (PE) direction is low, leading to geometric distortion in that direction (4). Secondly, the  $T_2^*$  relaxation taking place throughout the data acquisition window causes blurring. Finally, the relatively long echo times (TE) associated with EPI sequences cause undesired  $T_2^*$ -weighting in the images.

The parallel imaging method GRAPPA, mentioned in Chapter 2, is a remedy for all of these issues. Skipping lines in the PE direction doubles the bandwidth along that direction, lessening geometric distortion. Moreover, with the number of k-space lines being acquired being reduced to one half, the acquisition window is also halved, which reduces  $T_2^*$  blurring. Lastly, the time it takes to get to the center of the k-space is significantly shortened, decreasing TE, and hence the  $T_2^*$ -weighting in the images. Although GRAPPA brings in many advantages, the drawback is the reduced amount of data, decreasing SNR. Furthermore, GRAPPA relies on the spatial encoding capabilities of the multi-channel coils. For a reduction factor of  $R = 2$ , the noise enhancement should be quite uniform, as to be

demonstrated in Chapter 5. However, reduction factors larger than 2 may cause localized noise enhancement patterns, depending on the design of the coil. In this study, R is set to 2.

In addition to GRAPPA, the sequence is also employing partial Fourier acquisition. As described in Chapter 2, Hermitian symmetry allows reduction of the amount of data by skipping some of the lines towards the edges of k-space. This shortens the acquisition window, and hence TE, alleviating both the  $T_2^*$  blurring and the  $T_2^*$ -weighting; however, this does not help with the low bandwidth along the PE direction since the spacing between the adjacent lines remains the same. The partial Fourier factor used in this study is 3/4.

The TE of the sequence can be further reduced by increasing the bandwidth along the readout direction. This is because each k-space line will be acquired faster. Nevertheless, the disadvantage is that, since the spectral window is widened, a higher amount of noise is spectrally welcomed into the acquisition. Despite this fact, doubling the bandwidth does not halve the SNR. That is, the effect of increasing the bandwidth does not very substantially decrease the SNR. In addition, a high number of samples are going to be collected by the sequence, introducing an intrinsic averaging effect during estimation. In this respect, a high bandwidth value yielding the shortest possible TE is preferred in this study.

#### **4.4 More on the usefulness of SR repetitions**

The SR repetitions shown in Figure 4.4 serves two very useful purposes in terms of sequence design – providing high-SNR phase correction scans for low-SNR or negated slices, and providing high-SNR GRAPPA calibration data. These two issues will be detailed next.

In EPI, the k-space lines are acquired in alternating directions. That is, if one line is acquired in the negative-to-positive direction, to form one of the so-called *odd echoes*, the next line is acquired in the positive-to-negative direction, to form one of the so-called *even echoes*. Before applying an inverse Fourier transform operation, the even echoes have to be flipped. This leads to phase inconsistencies caused by factors such as eddy currents,  $B_0$ -field inhomogeneity, group delays in circuitry, and concomitant magnetic fields (4).

The sequence in this study involves an inversion pulse, meaning that the spins in the volume of interest will experience inversion recovery and be sampled at different phases of this recovery process. The data used in this study was collected on a Siemens Tim Trio 3T MR scanner (Siemens Healthcare, Erlangen, Germany). By default, a number of phase correction scans are acquired before each slice and these scans are used to infer the phase correction to be applied to the true imaging scans. As Figure 4.5 depicts, when a slice goes through the negative portion of the inversion recovery process, that is, when the longitudinal magnetization vectors point in the negative z direction, the phase correction algorithm fails.

In order to overcome this surprising problem, an in-house reconstruction module with memory is developed and integrated into the reconstruction chain. As spins go through various portions of the recovery process, the SNR can become very low, especially while passing through the zero-crossing point. The custom module developed for this study simply stores the phase correction scans coming with the high-signal SR repetitions and, for any other repetition, determines whether or not the phase correction scans need to be negated. The module then sends the stored phase correction scans accordingly. As Figure 4.6 indicates, this solution works very well.

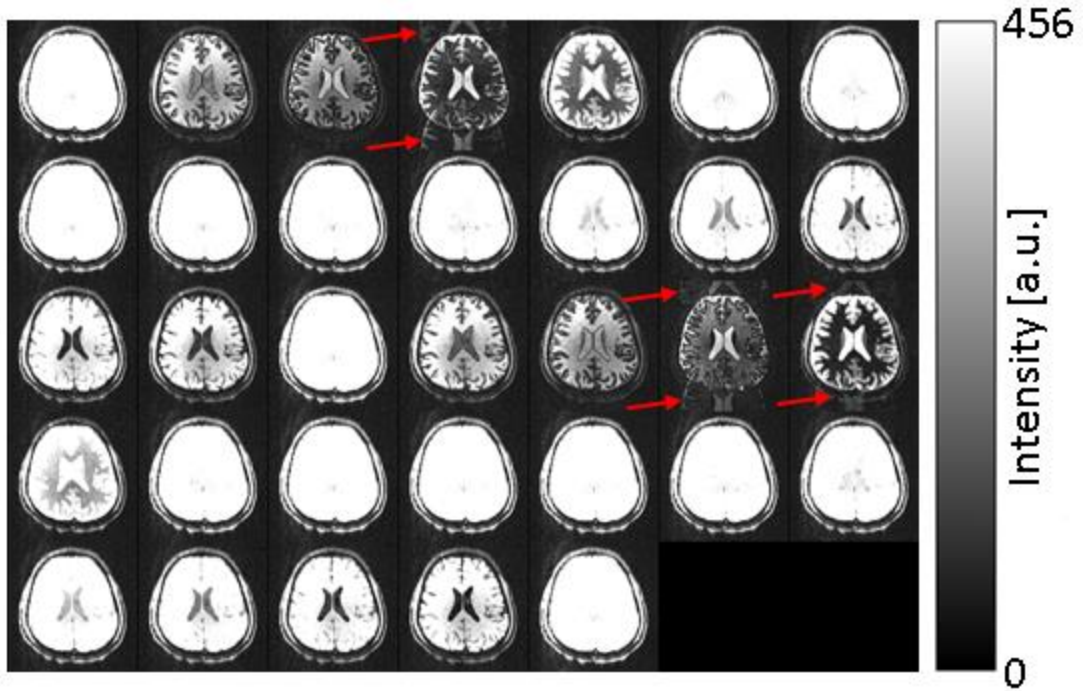


Figure 4.5 – EPI phase correction fails when some tissues are within the negative portion of the inversion recovery process.

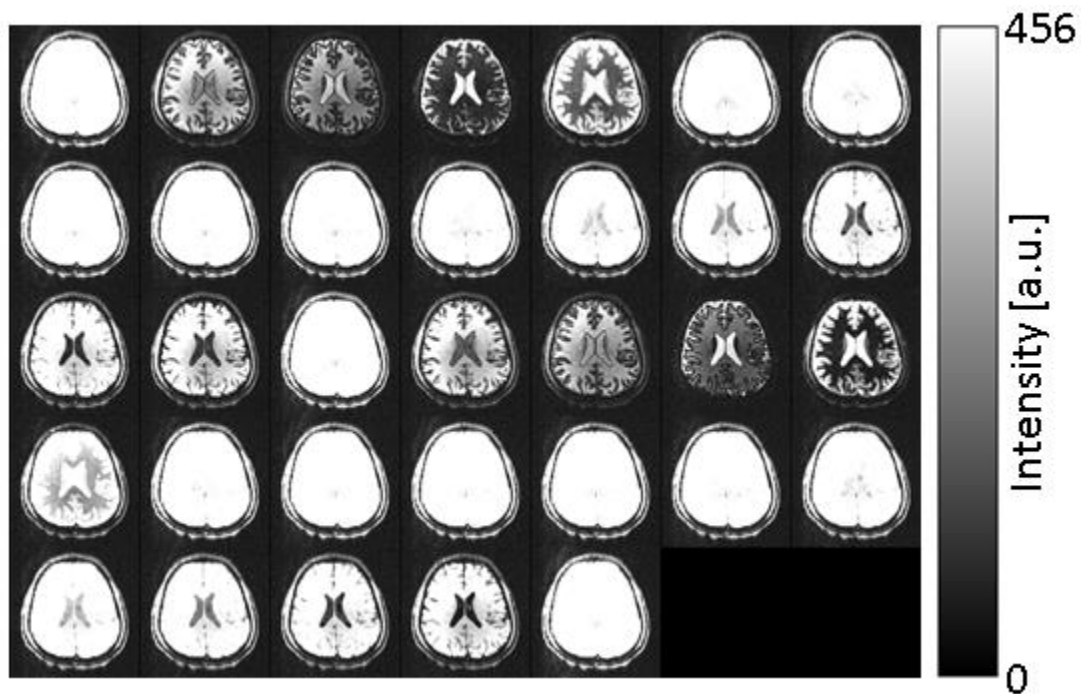


Figure 4.6 – The in-house reconstruction module successfully overcomes the problem shown in Figure 4.5.

In addition to the good-quality phase correction scans, SR repetitions are also useful for obtaining good-quality GRAPPA calibration data. By default, the GRAPPA calibration repetitions possess the same magnetization preparation scheme as the repetitions to which they are attached. For example, if the imaging repetition has an inversion pulse, so does the GRAPPA calibration repetition prepended to it. Since the SR repetitions do not have any inversion pulses, the GRAPPA calibrations attached to them do not have them either. Because the GRAPPA calibration scans are performed at the beginning, it is a prudent selection to place the SR repetitions at the beginning of each segment of the sequence. Otherwise, if an IR repetition is used, the GRAPPA calibration repetition will also have an inversion pulse and, depending on the temporal order of acquisition, some slices may very well go through the zero-crossing point during calibration. The end result is that the GRAPPA calibration data acquired for such slices will be very low-SNR and the GRAPPA reconstruction for that slice will be problematic. Figure 4.7 illustrates this problem. An inversion pulse was intentionally placed at the GRAPPA calibration repetition. It can be seen that some slices show severe ghosting. The reason why neighboring slices do not manifest this problem is that the even slices are acquired first and the odd slices are acquired later. Figure 4.8 closely represents the GRAPPA calibration repetition, and hence explains why ghosting takes place. The slices with failing GRAPPA reconstruction in Figure 4.7 show moderate to low SNR values in Figure 4.8, implying that the SNR of the GRAPPA calibration data will be low for those slices. However, as Figure 4.9 demonstrates, when the inversion pulse is removed from the GRAPPA calibration repetition, the artifacts disappear.

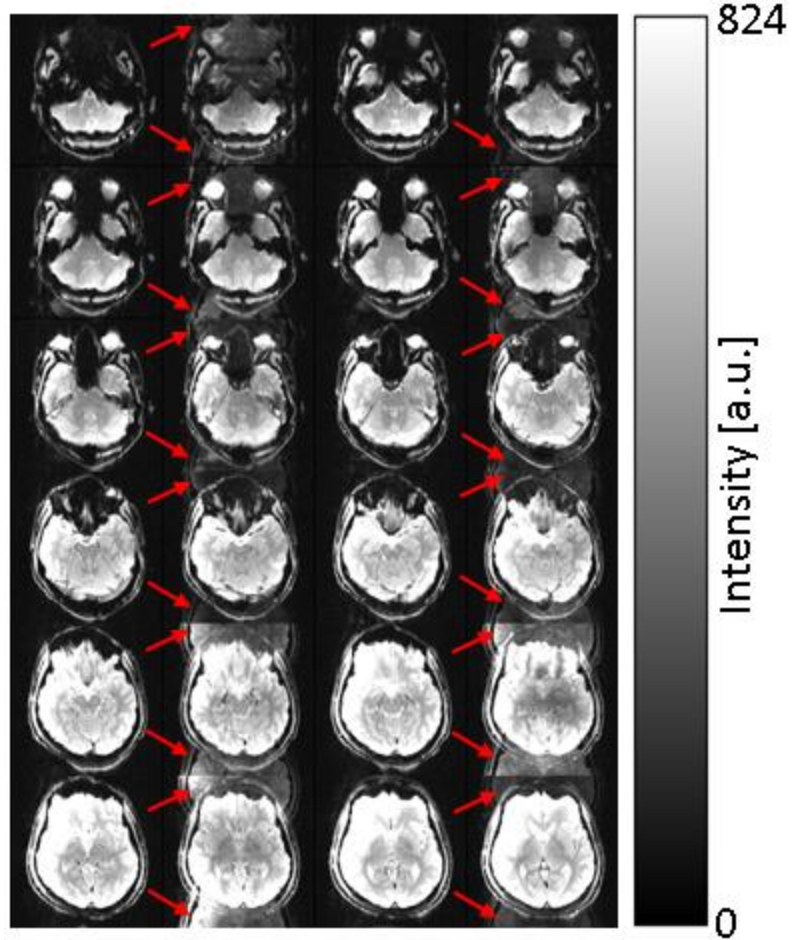


Figure 4.7 – SR repetition images (Slices 1-24) when an inversion pulse is placed before the GRAPPA calibration scan. The red arrows indicate the artifacts due to GRAPPA failure caused by poor calibration data.

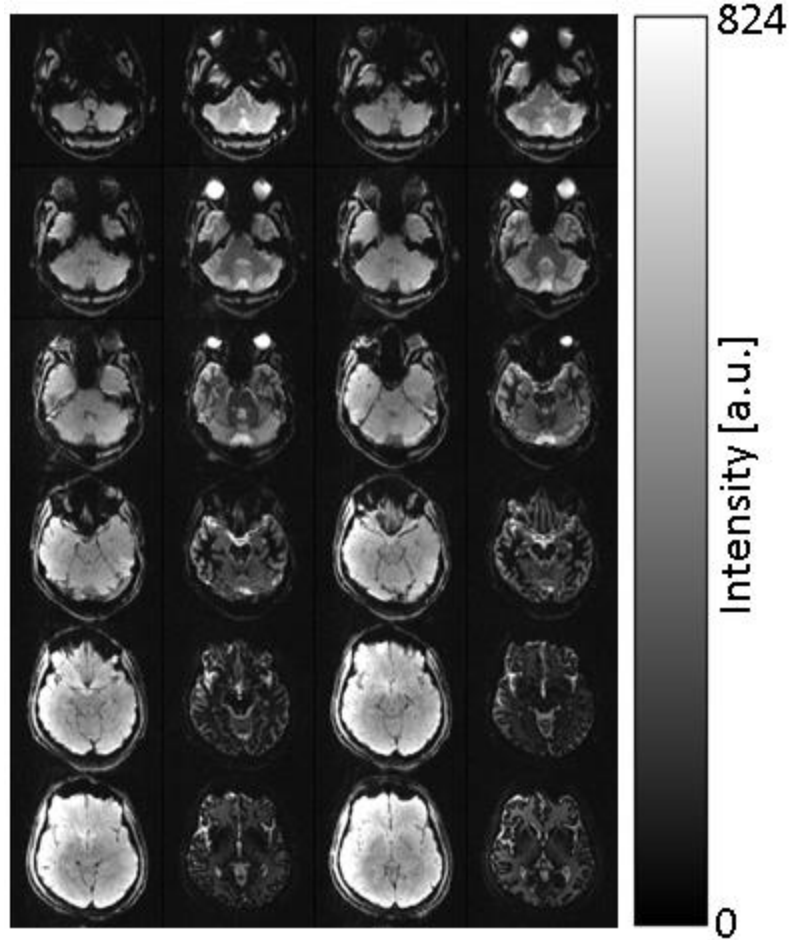


Figure 4.8 – The IR repetition right after the first SR repetition. This repetition closely represents the situation in the GRAPPA calibration repetition. The low-signal slices experience GRAPPA failure as shown in Figure 4.7, with the impact being stronger for the slices with even lower intensities

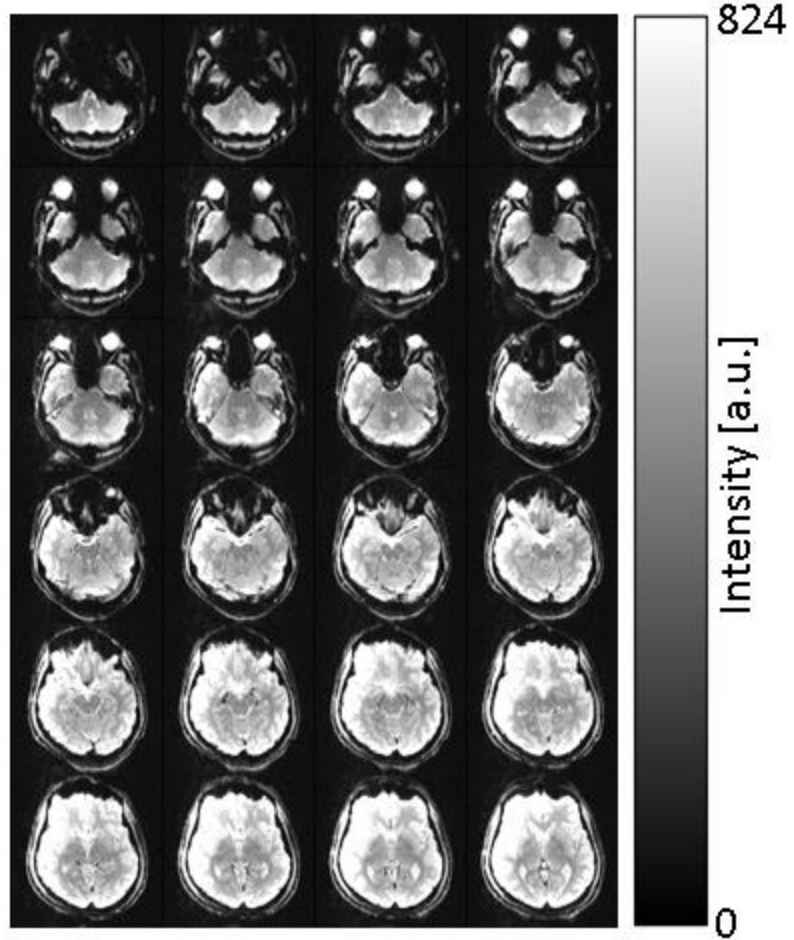


Figure 4.9 – SR repetition images when no inversion pulse is placed before the GRAPPA calibration scan. GRAPPA calibration data is now high-SNR for all slices and the issue in Figure 4.8 is resolved.

## CHAPTER 5: T<sub>1</sub> MAPPING

### 5.1 Weighted least-squares (WLS)

The longitudinal recovery process is governed by the following first-order differential equation (1):

$$\frac{dM_z}{dt} = -\frac{M_z - M_o}{T_1} \quad (5.1)$$

where  $M_o$  is the net equilibrium magnetization,  $M_z$  is the magnetization along the longitudinal axis at any given time, and  $T_1$  is the longitudinal relaxation time. The solution of Equation (5.1) for an initial longitudinal magnetization value of  $M_{z'}(0) = M_{z',0}$  is given by:

$$M_{z'}(t) = M_{z',0}e^{-t/T_1} + M_o(1 - e^{-t/T_1}) \quad (5.2)$$

The first thing to realize is that, when a slice is sampled, the longitudinal magnetization is nullified for all spins and they will start to recover from  $M_{z',0} = 0$ , which implies that the governing equation from the time of being sampled to the time of being sampled again or being inverted by the inversion pulse becomes:

$$M_{z'}(t) = M_o(1 - e^{-t/T_1}) \quad (5.3)$$

Remembering that no inversion pulses are played during the GRAPPA calibration repetitions or the SR repetitions, a given slice has a whole repetition time (TR) to relax before being sampled at these repetitions. Therefore, we are able to express the magnetization sampled at these repetitions as:

$$M_{z'}(TR) = M_o(1 - e^{-TR/T_1}) \quad (5.4)$$

For the IR repetitions, however, the issue is a bit more complicated. The time the spins spend relaxing in the preceding repetition and the inversion pulse being played in the current repetition are the two critical points. The former determines the magnitude of the magnetization before it hits the inversion pulse, and the latter negates it and yields an initial condition for the recovery process. More formally, right after the application of the inversion pulse, the longitudinal relaxation process in an IR repetition is, again, governed by Equation (5.2), but with the following initial condition:

$$M_{z',0} = -M_o(1 - e^{-(TR-TI_{prev})/T_1}) \quad (5.5)$$

where  $(TR-TI_{prev})$  is the time the spins spend relaxing between the time of being sampled in the preceding repetition and the time of the application of the inversion pulse in the current repetition. The minus sign is due to the application of the inversion pulse. The spins will now relax with this initial magnetization until the slice is sampled, in which case, the longitudinal magnetization becomes:

$$\begin{aligned} M_{z'}(TI_{curr}) &= -M_o(1 - e^{-(TR-TI_{prev})/T_1})e^{-TI_{curr}/T_1} + M_o(1 - e^{-TI_{curr}/T_1}) \quad (5.6) \\ &= M_o(1 - 2e^{-TI_{curr}/T_1}) + M_o e^{-(TR+TI_{curr}-TI_{prev})/T_1} \end{aligned}$$

The longitudinal magnetization at each repetition can now be calculated from Equations (5.4) and (5.6).

The GRAPPA reconstruction works by obtaining individual coil images and then combining them through a sum-of-squares reconstruction. From this point on, the notation used in (43) will be adopted with some modifications.

For a receiver system with  $K$  coils, the signal measured at a given voxel in the individual image of coil  $k$  at any given time point can be expressed as:

$$S_k = A_k + n_k = C_k f(M_o, T_1, \mathbf{TI}, TR) + n_k \quad (5.7)$$

where  $A_k$  is the noise-free signal from coil  $k$ ,  $C_k$  is the coil sensitivity,  $f(\cdot)$  performs the operations in Equations (5.4) or (5.6) and outputs  $M_z'$ ,  $M_o$  is the net equilibrium magnetization,  $T_1$  is the longitudinal relaxation time,  $\mathbf{TI}$  is the vector of inversion times, or, put differently, the vector of sampling times at each repetition,  $TR$  is the repetition time of the sequence and, finally,  $n_k$  is the noise term, the distribution of which can be shown to be Gaussian (43). It should be noted that, although  $f(\cdot)$  takes as input the whole  $\mathbf{TI}$  vector, it uses only two of its elements at any given inversion recovery repetition; the inversion time for the previous repetition and that for the current repetition, because the magnetization depends only on these two inversion times as can be seen in Equation (5.6).

The sum-of-squares reconstruction yields:

$$I_{SOS} = \sqrt{\sum_{k=1}^K S_k^2} \quad (5.8)$$

In (43), the authors prefer to give the statistical properties of  $I_{SOS}^2$  rather than  $I_{SOS}$ . It is shown that  $I_{SOS}^2$  approximately follows a non-central  $\chi^2$  distribution with the following mean and standard deviation:

$$E\{I_{SOS}^2\} = A_{SOS}^2 + 2tr(\mathbf{C}) \quad (5.9)$$

$$var\{I_{SOS}^2\} = 4\mathbf{A}^T \mathbf{C} \mathbf{A} + 4\|\mathbf{C}\|_F^2 \quad (5.10)$$

where  $\mathbf{A} = [A_1 A_2 \dots A_K]^T$ ,  $A_{SOS}^2 = \mathbf{A}^T \mathbf{A}$  and  $\mathbf{C}$  is the  $K \times K$  covariance matrix computed between the coils for the pixel of interest.  $M_0$  and  $T_1$  would then be obtained by the minimization of the following weighted least-squares cost function:

$$J_{WLS} = \sum_{i=1}^N \frac{(I_{SOS,i}^2 - A_{SOS,i}^2 - 2tr(\mathbf{C}))^2}{4\mathbf{A}_i^T \mathbf{C} \mathbf{A}_i + 4\|\mathbf{C}\|_F^2} \quad (5.11)$$

where  $N$  is the number of data points to be used during curve-fitting that were acquired at various phases of the recovery process and the subscript  $i$  signifies the quantities obtained at time point  $i$ . Please note that, in this equation,  $A_{SOS,i}^2$  and  $\mathbf{A}_i$  are the noise-free measurements obtained by the model equation given in Equation (5.7). The fitting process begins by calculating these noise-free quantities from the initial values of the parameters. The parameter estimates will then be refined by minimizing  $J_{WLS}$  until convergence is achieved.

## 5.2 Ordinary least-squares (OLS)

The cost function in Equation (5.11) does not look cumbersome, but it does require a large amount of additional data. In order to estimate the coil sensitivities used in Equation (5.7), at least one set of uncombined coil images are needed. Moreover, reliable estimation of the covariance matrix  $\mathbf{C}$  will be possible only if many more sets of uncombined coil images are collected. For a 60-slice acquisition with 32 coils, collecting 100 sets of uncombined coil images amounts to  $60 \times 32 \times 100 = 192,000$  images! Considering the huge memory requirements and the difficulty of data transfer, this is not feasible at all, especially in a clinical setting.

It is also worth noting that the correlation between the receiver coils violates the assumption of having a non-central  $\chi^2$  distribution with  $K$  degrees of freedom,  $K$  being the number of coils. The degrees of freedom thus need to be reduced to arrive at a more accurate model (43). Furthermore, the assumption gets even worse for  $\text{SNR} > 2$ . Looking at the Gaussian approximation to the non-central  $\chi^2$  distribution in (43), Gaussianity can safely be assumed for  $\text{SNR} > 3$  and, when Gaussianity is in place, ordinary least-squares can provide a more straight-forward solution. The question would then be “**Does *in vivo* data exhibit such high SNR?**”. The best answer would come from the data itself. Without loss of generality, let us focus on the putamen. Figure 5.1 depicts a middle slice for the first 6 repetitions of the sequence. The intensity loss in the putamen can clearly be observed in the 3<sup>rd</sup> repetition.

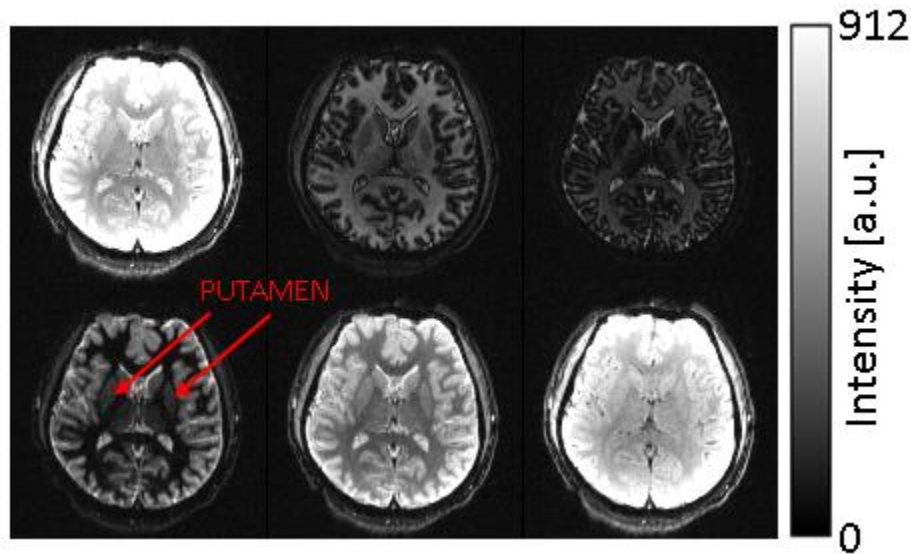


Figure 5.1 – Various phases of inversion recovery for a middle slice which clearly shows the putamen going through intensity variations.

In order to quantitatively assess the average SNR in the putamen, the so-called “difference method” is deployed (44-46) because it has been shown to yield the best result in reference to the gold-standard method of acquiring the images multiple times (47), is much

simpler to implement, and is also more preferable *in vivo* since the long acquisition times associated with the gold-standard method increase the risk of motion. In this method, an image is acquired twice using identical parameters. After computing the sum of and the difference between the two images, the mean value and the standard deviation is computed in a region of interest (ROI). Dividing the mean value by the standard deviation and also by a factor of  $\sqrt{2}$  yields the average SNR in that ROI.

Figure 5.2 plots the average SNR in the putamen area as a function of sequence repetitions so that the SNR in the putamen can be observed at various stages of inversion recovery. It can be readily observed that the SNR never drops below 3. Similar results were obtained for ROIs drawn in the white matter and the cortical gray matter. Thus, the use of ordinary least squares is justified.

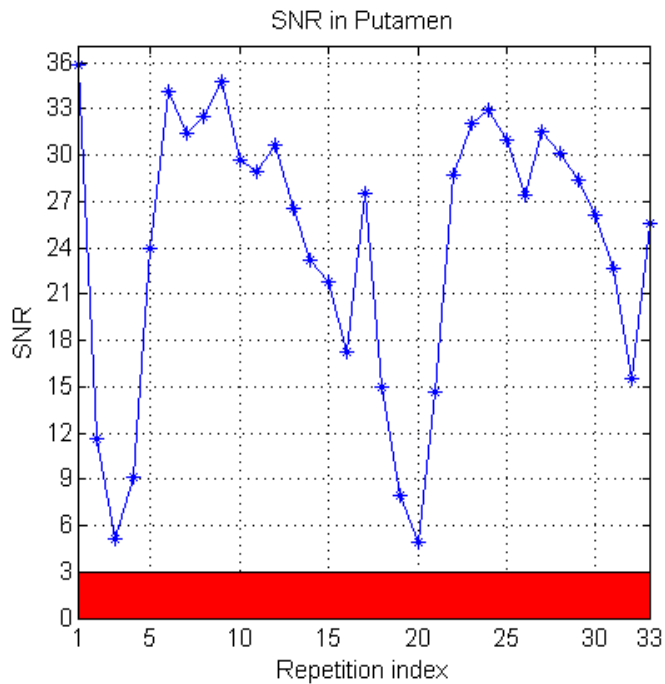


Figure 5.2 – Average SNR in the putamen as a function of sequence repetitions. The red band shows the SNR range for which the Gaussianity assumption is invalid.

The cost function for the ordinary least-squares problem would simply be

$$J_{OLS} = \sum_{i=1}^N (I_{SOS,i} - A_{SOS,i})^2 \quad (5.12)$$

### 5.3 Comparison of WLS and OLS

A single-slice experiment was run where, in addition to images acquired by the proposed method, 100 sets of 32 uncombined images were collected to get a reliable covariance matrix estimate. Equations (5.11) and (5.12) were then used to get the  $T_1$  estimates. All computations were performed on Matlab (Mathworks, Natick, MA).

Figure 5.3 exhibits the means and standard deviations of the  $T_1$  values in an ROI drawn onto the central region of the phantom whereas Figure 5.4 illustrates the associated histograms.

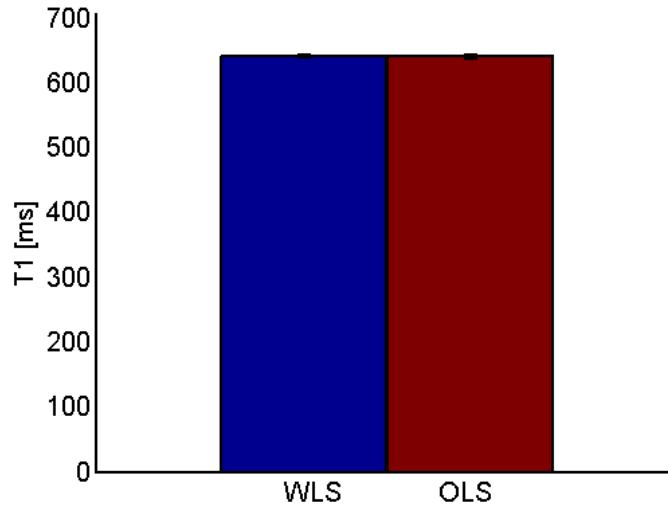


Figure 5.3 – Average  $T_1$  values as measured by WLS and OLS with error bars. Because the standard deviations are small, the error bars are barely visible.

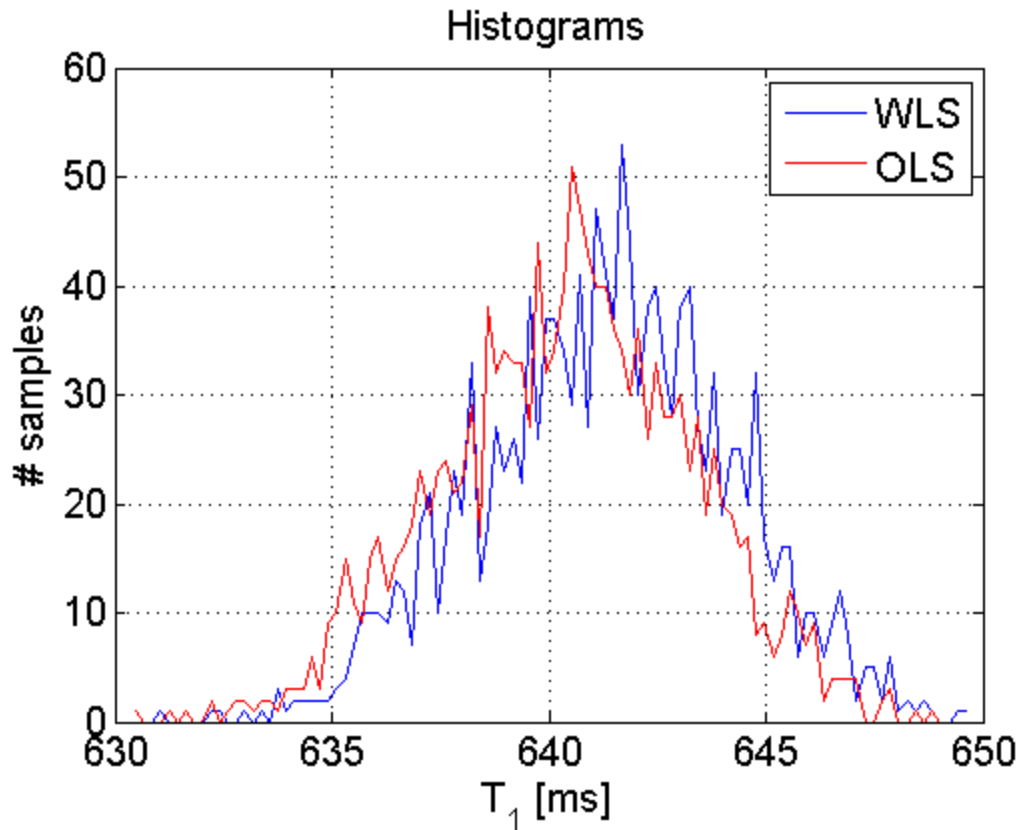


Figure 5.4 – Histograms of  $T_1$  values as measured by WLS and OLS. The distribution of the WLS values shows a very slight shift towards right.

It can be seen that the WLS method yields slightly larger  $T_1$  values. The difference is within the noise floor. It is worth noting that, for a sample with a much larger  $T_1$ , the difference would be larger. However, it is expected that this difference will still be within the variation in the estimates since these variations are generally amplified with increasing  $T_1$ . Careful experimenters are, nevertheless, encouraged to confirm this guess before assuming that it indeed is the case.

Considering the many disadvantages of the WLS scheme, the OLS scheme will be the method of choice for the rest of the study.

#### 5.4 Comparison with the gold standard in phantom

Four different concentrations of  $\text{Ni(II)SO}_4 \cdot 6\text{H}_2\text{O}$  were prepared to mimic the  $T_1$  values encountered in the human brain. The parameters for the gold standard inversion recovery (IR) sequence were as follows: Matrix size =  $128 \times 128$ , FOV =  $200\text{mm} \times 200\text{mm}$ , Slice thickness =  $2\text{mm}$ , TE =  $19\text{ ms}$ , Bandwidth =  $1562\text{ Hz/pixel}$ , GRAPPA R = 2, Number of calibration lines = 30, Partial Fourier Factor =  $6/8$ . (The parameters up to this point were the same for the proposed method.) TR =  $20000\text{ ms}$ , Number of slices = 1, # TI values = 43 with an additional, almost fully relaxed  $M_0$  scan at the very beginning, Minimum TI value =  $25\text{ ms}$ , Maximum TI value =  $14525\text{ ms}$ . In all phantoms, the last sample with TI =  $9925\text{ ms}$  showed ghosting artifacts for unknown reasons, and hence was discarded. The total acquisition time was **about 22 minutes**.

As for the proposed method: TR =  $4000\text{ ms}$ , Number of slices = 60, # repetitions = 33 that includes three saturation recovery (SR) samples – one at the beginning, one in the middle and one at the very end, Slices were shifted by 4, Slice 30 was matched with the single-slice gold standard acquisition above. The total acquisition time was **2 minutes and 32 seconds**. At this point, it is useful to recall the sequence structure given in Chapter 4. Figure 5.5 details the proposed sequence.

The data acquired with the proposed method was post-processed in two ways: 1) including, 2) excluding the SR repetitions (that is, the repetitions that do not involve an inversion pulse). This way, it can be confirmed whether or not the SR samples indeed help alleviate underestimation by bringing in high-amplitude samples.

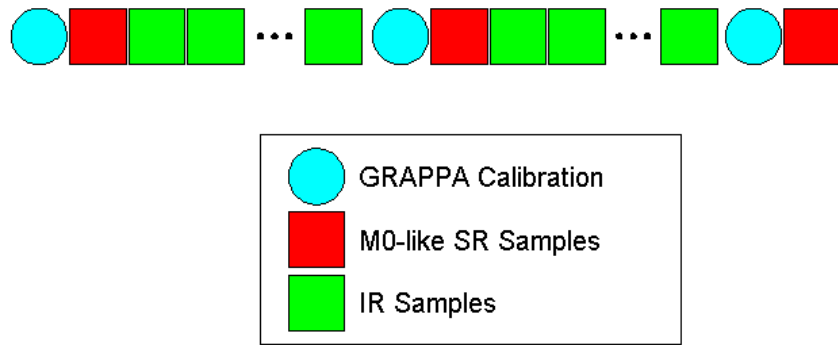


Figure 5.5 – Structure of the proposed sequence

Figure 5.6 shows the means and the standard deviations for the gold standard IR method along with the two post-processing schemes for the proposed method. It can be seen that, regardless of which post-processing scheme is used, the  $T_1$  estimates are quite close to those obtained by the IR method, albeit with some underestimation. The inclusion of the SR samples, however, does help with the underestimation issue, especially for the long- $T_1$  species. This has been confirmed in each of the four phantoms with paired t-tests which yielded p-values that are practically zero. Figure 5.7, on the other hand, exhibits the Bland-Altman plot, which quantifies the percent estimation errors as a function of  $T_1$  values. The proposed method is able to estimate  $T_1$  with less than 5% error.

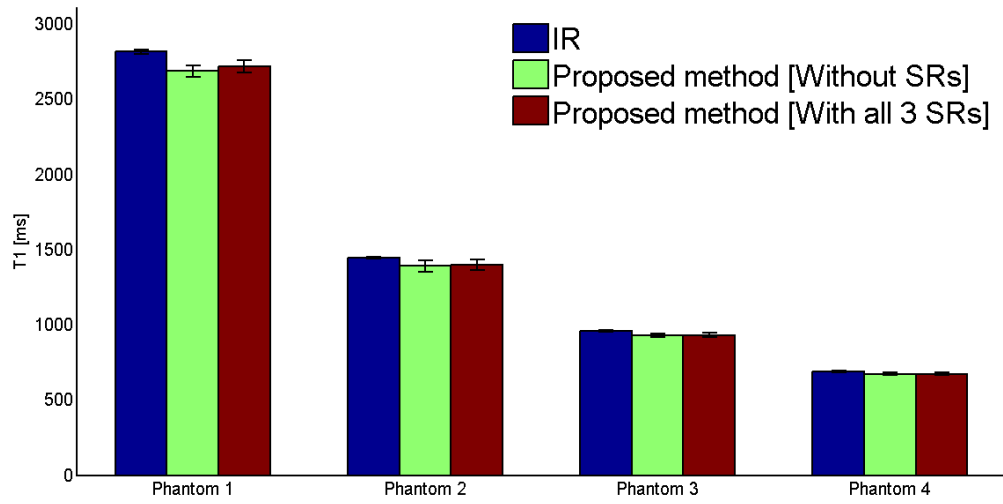


Figure 5.6 – Means and standard deviations for the gold standard IR method and the proposed method

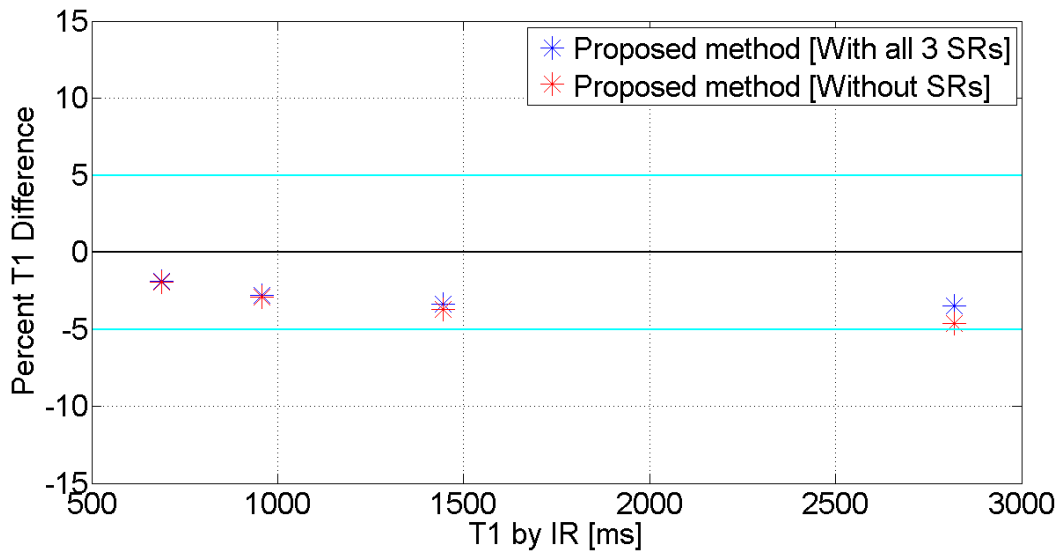


Figure 5.7 – Bland-Altman plot

## 5.5 Comparison with the gold standard *in vivo*

The acquisition parameters were exactly the same as those used in the phantom experiment. However, it is worth noting that, while acquiring the data for the gold-standard method, it was not easy for the subjects to keep still for the whole length of the sequence, which is more than 20 minutes. Fortunately, the motion was mostly in-plane and was corrected by Matlab's *imregister* function. The registration was selected to be rigid and the cost was chosen to be mutual information since the relative intensities would vary by a great deal during the recovery process.

Data was collected from four subjects with ages between 25 and 36 years. Written informed consent was obtained from all participants.

Figure 5.8 qualitatively compares the  $T_1$  values obtained by the proposed method with those obtained by the gold standard IR method while Figure 5.9 yields a more quantitative comparison. Although the errors were within 5% in phantom, the underestimation *in vivo* is much larger. The slice cross-talk, that is, the disturbance of the neighboring slices while exciting the intended slice, has some contribution to the underestimation; however, the magnitude of this effect should not be large. Otherwise, the phantom results would also show that. As also pointed out nicely in (42), the actual effect should be coming from something that does not exist in the phantom: perfusion. Blood flow and the exchange between blood and brain water cause a decrease in the apparent  $T_1$  value (48). Nevertheless, as Figure 5.10 illustrates, the values output by the two methods are almost perfectly correlated.

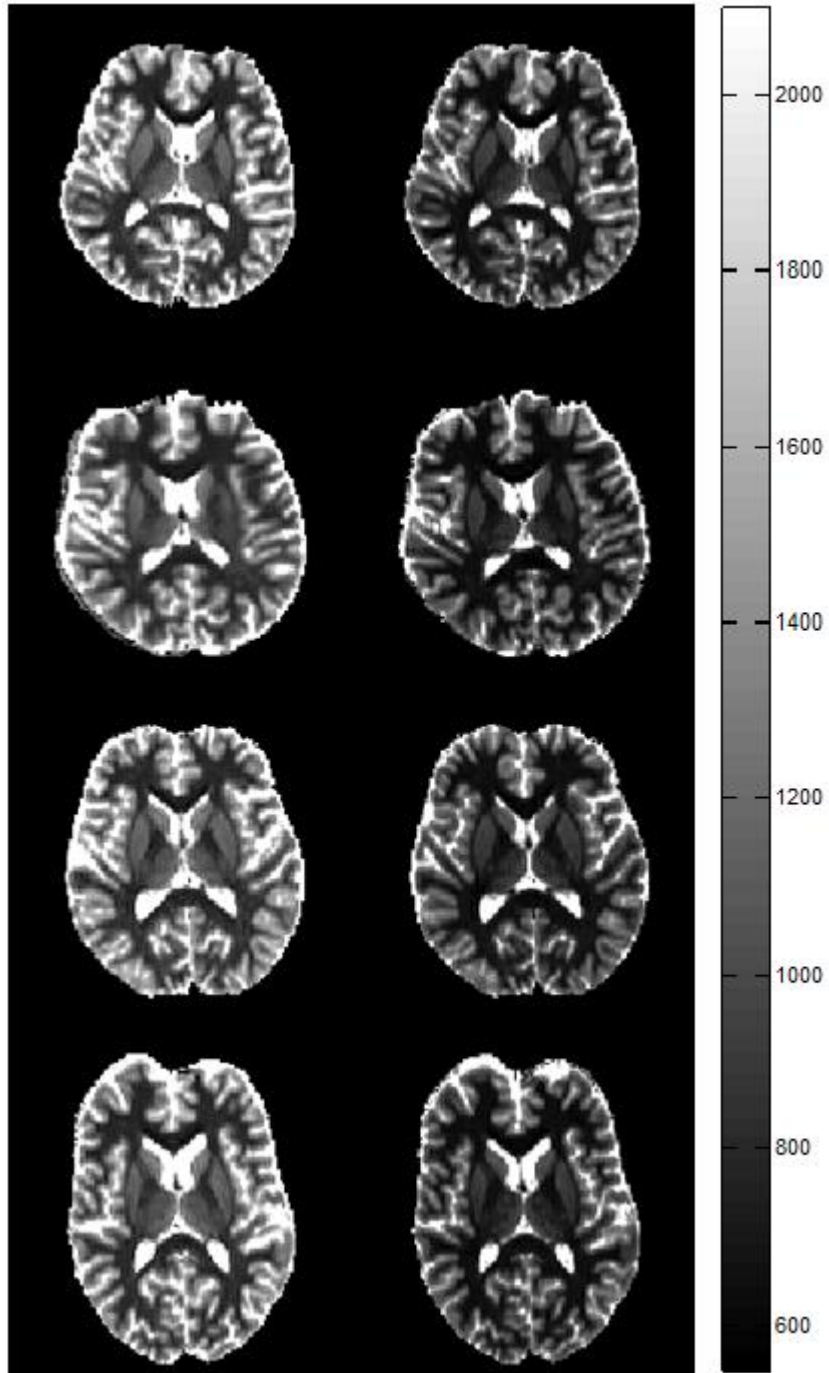


Figure 5.8 – Comparison of the  $T_1$  values obtained by the proposed method (right column) with those obtained by the gold standard method (left column). The values are in milliseconds.

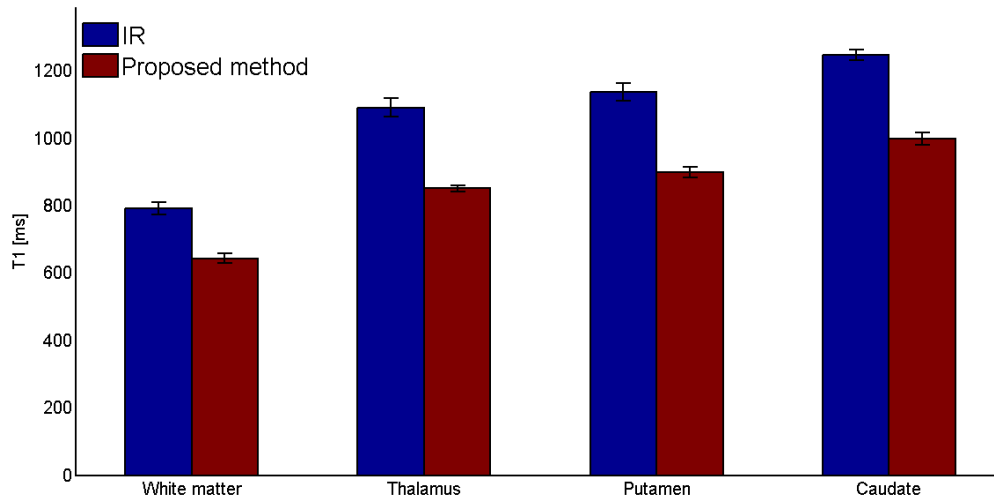


Figure 5.9 – Comparison of the  $T_1$  values obtained by the proposed method with those obtained by the gold standard method across four subjects and in four anatomical regions

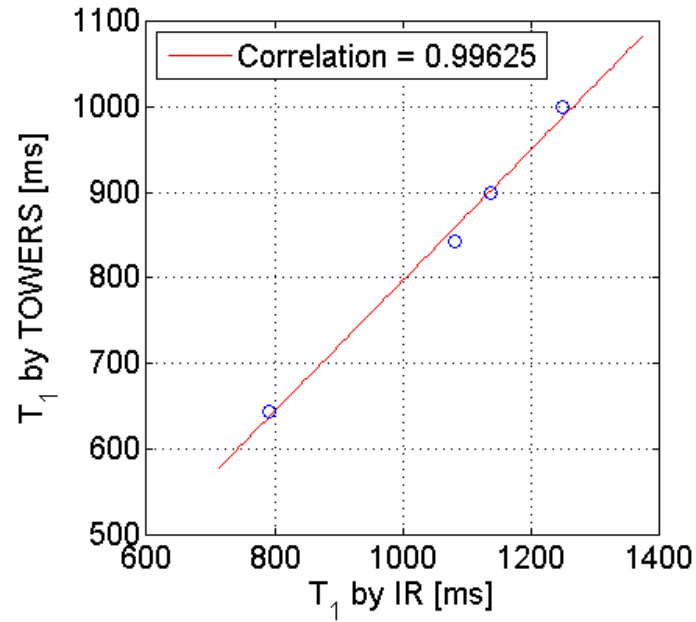


Figure 5.10 – Correlation between the  $T_1$  values obtained by the proposed method with those obtained by the gold standard method across four subjects and in four anatomical regions

Figure 5.11 shows what happens when the repetition time of the sequence is lengthened. In this case, the perfusion effects are alleviated and the underestimation is much less pronounced. However, this long-TR version of the sequence takes about 12.5 minutes, as opposed to 2.5 minutes. This increases the risk of motion. Furthermore, if, while the slices are being shifted 4 by 4, a slice can never get to the slot closest to the inversion pulse, the smallest TI value it can experience in any of the two segments is about 350 ms for this long-TR version. Considering the fact that the early phase of the recovery is faster, this amounts to losing a sample that is very valuable for curve fitting purposes. This long-TR effect is noticeable when one visually goes through all of the slices in the volume. The slices that cannot get temporally very close to the inversion pulse exhibit some underestimation compared to the ones that can.

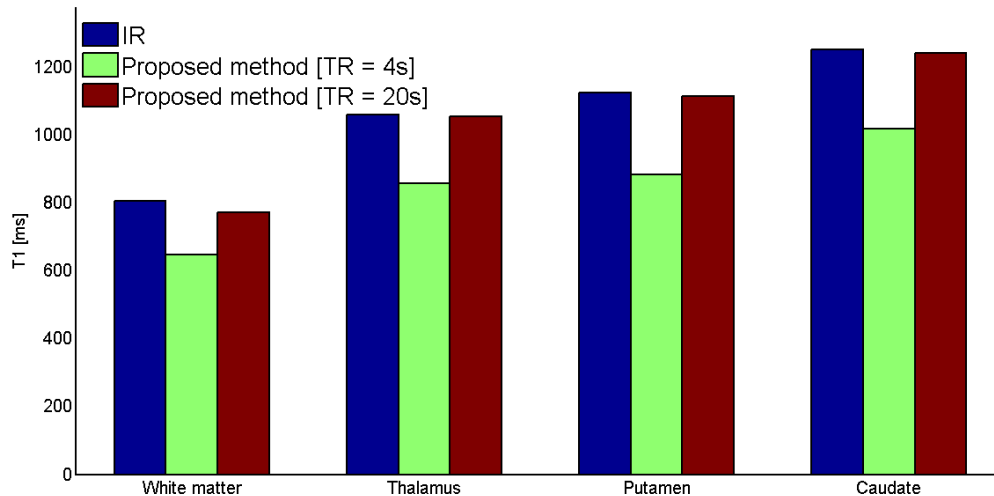


Figure 5.11 – Demonstration of the effect of lengthening the repetition time of the sequence in one of the subjects

One could ask if underestimation is an issue only for TR values below a certain threshold, or if underestimation is always an issue no matter what the TR is and becomes more severe with decreasing values of TR. The answer is perhaps: a combination of both. When the TR is above a certain threshold, the transient perfusion effects mentioned above may have enough time to completely disappear. However, if the amplitude of the samples being collected decreases gradually as the TR of the experiment decreases (which makes full relaxation unachievable), the dynamic range of the experiment decreases and this leads to estimation errors, typically underestimation.

In (42), the authors expressed the true longitudinal relaxation rate, which is simply the reciprocal of the longitudinal relaxation time  $T_1$ , as a linear function of the apparent relaxation rate. This linear relationship was then used to “rectify” the underestimated  $T_1$  values. This approach was not adopted in this study.

## **5.6 Reproducibility**

In order to test the reproducibility of the mapping procedure, three of the four subjects mentioned above were scanned 4 times with identical scan parameters. Figure 5.12 depicts the coefficients of variation (CVs) calculated as the standard deviations divided by the means across all 4 scans. It can be seen that the CVs are all below 3%, which indicates the reliability of method.

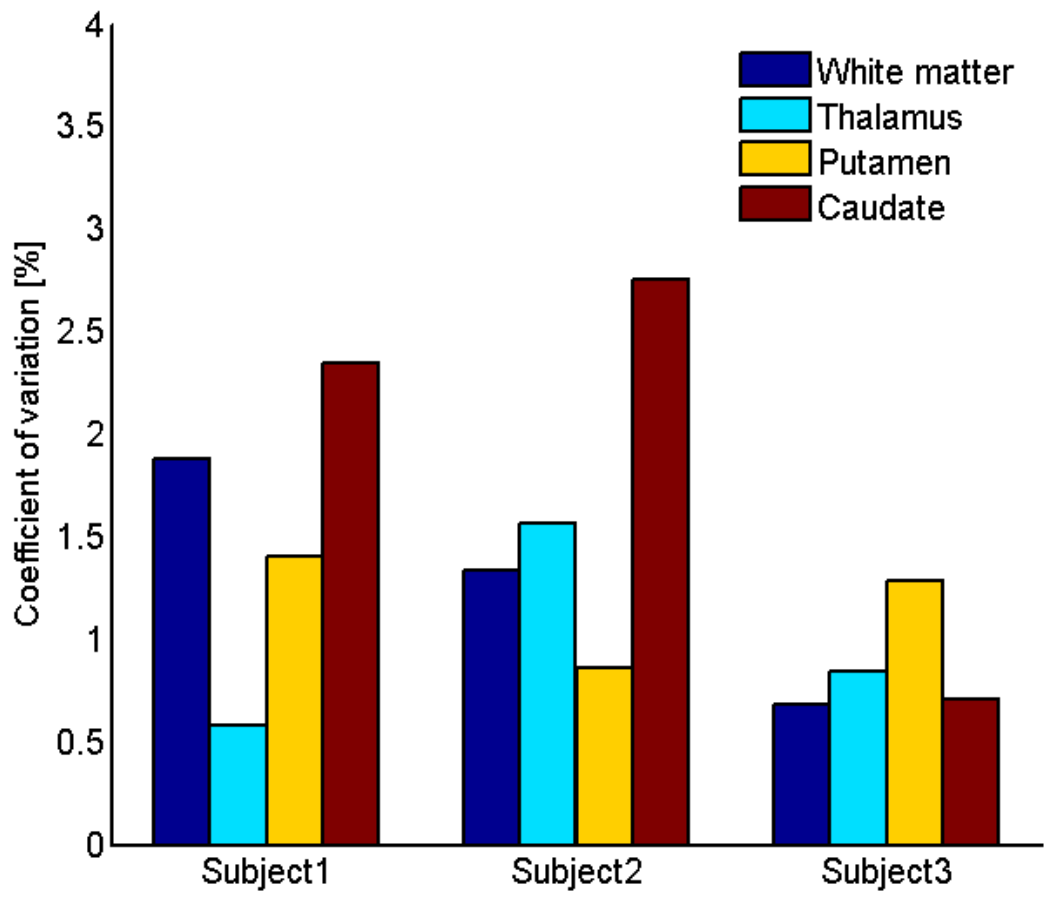


Figure 5.12 – Coefficients of variation across four identical scans

## CHAPTER 6: MOTION

### 6.1 Effects of motion

Motion damages the proposed acquisition scheme mainly in the following three ways:

- 1) The sequence is using single-shot EPI (3), which is capable of, with the help of some acceleration techniques, acquiring the data sufficient to reconstruct a single slice within less than 100 ms. Should significant motion occur, even during this short interval, k-space inconsistencies, and hence image artifacts are inevitable. However, due to the speed of the EPI technique, this first problem is seldom an issue.
- 2) The proposed scheme is making use of GRAPPA (6), a parallel imaging method that makes use of the spatial encoding capability introduced by multiple surface coils to fill in missing k-space lines that have been skipped intentionally to accelerate the acquisition. These missing lines are calculated from the acquired ones through a linear operator whose coefficients are computed using the calibration data acquired typically at the beginning of the acquisition. Motion at any time simply invalidates the reconstruction coefficients and the calibration scan has to be repeated. Otherwise, the newly filled-in k-space lines will be inaccurate, leading to ghosting in the resulting images. Past experience shows that this second problem is substantial if the motion is large in magnitude. For small motion, GRAPPA does not fail very easily, especially when the number of coil elements is sufficiently high. In what follows, the robustness of the proposed sequence is going to be tested under harsh motion scenarios where GRAPPA failure may occur.
- 3) Each slice acquired by the proposed sequence goes through a different magnetization pathway. Therefore, if the slice locations change as a result of motion, the magnetization pathway will also be altered and this needs to be taken into account during post-processing. This third problem is the most significant one, because even a small shift in the slice-select direction causes a substantial change in the magnetization pathway. Furthermore, if motion occurs in one repetition, at least one more sequence repetition is required for the magnetization to completely settle down into one of the predefined pathways.

## **6.2 Redoing the GRAPPA calibration**

In a typical sequence that makes use of the GRAPPA technique, the calibration scans are acquired only at the very beginning and the update of the reconstruction coefficients is thus almost never performed within the sequence. It is a fortunate coincidence that, at the beginning of 2012, Dr. Jürgen Finsterbusch of Institut für Systemische Neurowissenschaften Universitätsklinikum Hamburg-Eppendorf provided a nice solution for this problem. Dr. Finsterbusch's solution is able to place the GRAPPA calibration scans at any given temporal location inside the sequence. It stores the latest set of calibration data and sends it through the reconstruction chain so that each repetition receives the most up-to-date set of calibration data.

## **6.3 Importance of the retrospective approach**

The solution mentioned in the previous section is very elegant. However, the newly acquired calibration scans are useful only for the repetitions that follow those scans, not for the ones that precede it. The following example can better illustrate the problem:

Let us assume that the subject moved only once, but significantly, at the 3<sup>rd</sup> repetition, and that the GRAPPA calibration update is going to be run right before the 11<sup>th</sup> repetition. In this case, the images acquired at repetitions 11, 12, 13 and so on would not show any artifacts because they are going to benefit from the newly acquired calibration data. Nevertheless, repetitions 4, 5, 6, 7, 8, 9 and 10, which are also acquired at the new position, are going to suffer from the use of old, incompatible calibration data. All these seven repetitions need to be discarded, which is clearly a waste of the time spent to acquire them. In this respect, it

would be extremely useful to retrospectively apply the appropriate calibration, and thus turn the images acquired at these repetitions into good-quality, usable pieces of data.

#### 6.4 Usefulness of the SR repetitions

At this point, it is worthwhile to recall the sequence structure. Figure 6.1 depicts the three calibration scans that can be utilized for improved GRAPPA reconstruction.

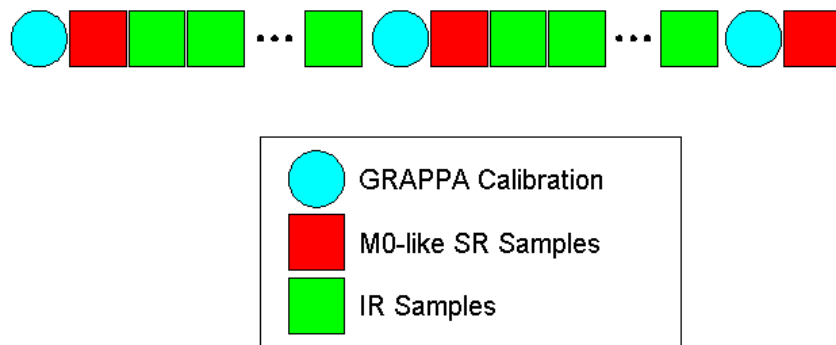


Figure 6.1 – Overall acquisition scheme

As mentioned in Chapter 4 and demonstrated in Chapter 5, the  $M_0$ -like SR repetitions help alleviate underestimation. As far as motion is concerned, however, they serve two other substantial purposes – they behave as solid reference points to be used for the retrospective treatment of motion artifacts and they can be registered onto each other in order to clarify if, and by how much, a given spin changes its location, and hence its magnetization pathway.

#### 6.5 Saving the calibration data

Retrospective reconstruction requires that the calibration information at each SR repetition be saved for later use. Rather than saving the k-space calibration lines themselves, the in-house reconstruction program saves the ultimate piece of information, namely the

reconstruction coefficients, or, equivalently, the information about how the data acquired from all individual coil elements should be combined to reconstruct the missing k-space lines. This way, the memory requirement is much less stringent. Storing the coefficients rather than a large number of k-space lines provides 2 to 3 orders of magnitude savings in disk usage. For instance, for a 32-channel coil, saving the calibration lines would occupy about 1.32 GBs of disk space, whereas saving the coefficients would occupy only about 2.81 MBs. In order for the sequence to be of practical use in an imaging center where large numbers of patients are being scanned daily, this simplification is extremely valuable.

It is also worth noting that the high-SNR phase correction scans mentioned in Chapter 4 that are coming from the SR repetitions are stored together with the GRAPPA reconstruction coefficients and are co-applied during retrospective reconstruction.

With the coefficients and the phase correction scans in place, the next step for retrospective reconstruction is deciding which repetition should be reconstructed with which set of coefficients. A semi-automatic motion detection scheme is proposed in the next section for this purpose.

## **6.6 Semi-automatic motion detection**

Since the intensities can show a great deal of variation from slice to slice during repetitions that play an inversion pulse, which were termed as IR repetitions above, not all slices can be used for motion detection. Instead, for each IR repetition, all voxel values in each slice are summed up, the slices are then sorted with respect to this sum, and the 5 highest-intensity slices are selected. In order to simplify the illustration of the method, these five-slice bundles from each repetition will be termed as *High5*. Each of the slices in the

High5 group of an IR repetition is compared to its counterpart in the most recent SR repetition via the following 2D cross-correlation metric:

$$\rho(s, r, k) = \frac{\sum_x \sum_y I(x, y, s, r) I(x, y, s, k)}{\sqrt{\sum_x \sum_y I(x, y, s, r)^2} \sqrt{\sum_x \sum_y I(x, y, s, k)^2}} \quad (6.1)$$

where  $s$  is the slice index,  $r$  is the repetition index and  $k$  is the SR repetition index. If any of the comparisons yields a correlation value less than 95%, the motion detection scheme issues a warning. The user checks the images and makes the final decision about what set to use for what repetition.

Once the repetitions are matched with the coefficient sets, this information can be instructed to the reconstruction program via a very simple plain text file which has only two columns – the first column keeping the repetition index and the second column indicating which of the three sets of coefficients the retrospective reconstruction should make use of.

Figure 6.2 summarizes the retrospective reconstruction scheme for a 20-slice acquisition.

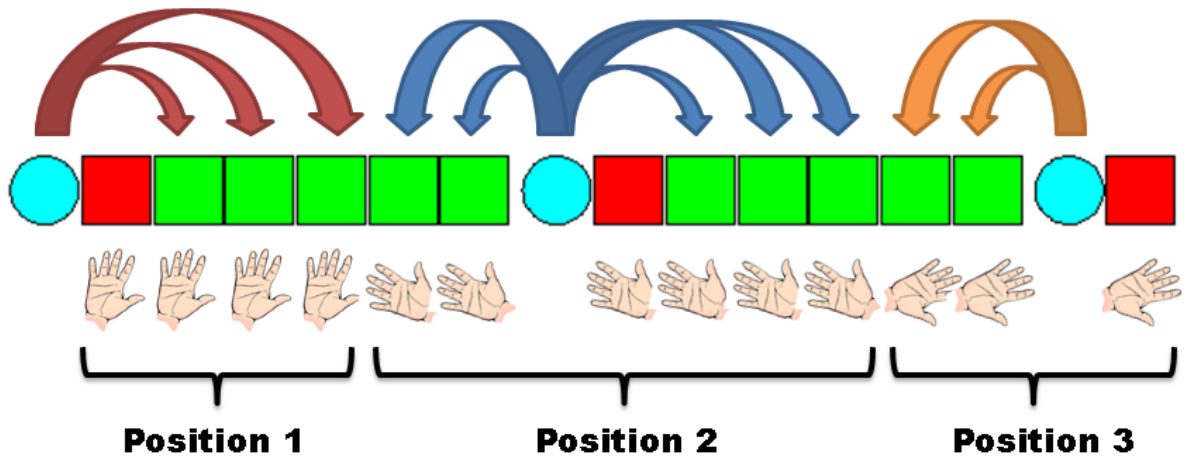


Figure 6.2 – Retrospective reconstruction in the presence of motion. Arrows show to which IR repetitions a given set of calibration data is applied. Hands represent the High5 slices. The change of position is indicated by the change in the orientation of the hands.

### 6.7 Retrospective reconstruction: An example

Figure 6.3 exhibits a sample case for movement-related GRAPPA failure. A 12-channel coil was used for this experiment. Therefore, with its reduced encoding capability compared to a 32-channel coil, the GRAPPA reconstruction should be more vulnerable to motion. The subject moved with some exaggeration and, it can be seen that, although the second and third SR repetitions reduce the strength of the artifact, they cannot completely remove it. This is perhaps because the brain remains far away from some of the channels, and these channels cannot make a sufficiently good contribution to the GRAPPA reconstruction.

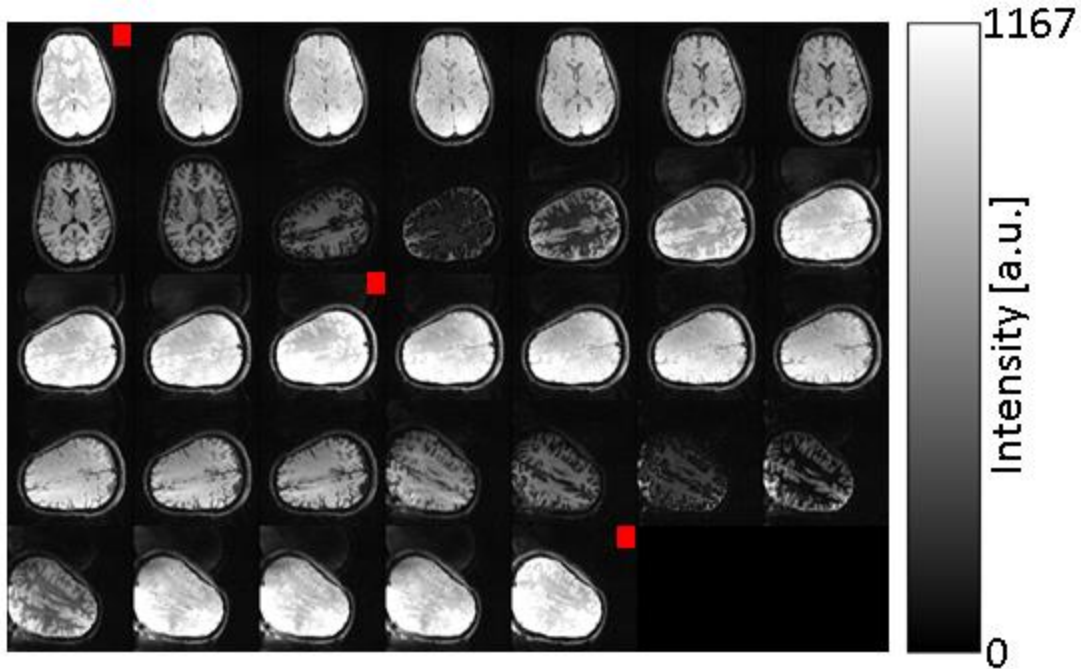


Figure 6.3 – A motion-corrupted data set. Red squares indicate the SR repetitions where the GRAPPA coefficients are being calculated and updated.

Figures 6.4, 6.5 and 6.6 exhibit, respectively, the 2D correlations of all slices in all repetitions with those in the first, second and third SR repetitions. For this particular case, all of the High5 slices in Repetitions 9-16 showed correlation values below 85% when compared with their counterparts in the first SR repetition, whereas those in Repetitions 24-33 showed correlation values below 70% when compared with their counterparts in the second SR repetition. It should be acknowledged that, for such a large motion, it is expected to have correlation values as low as these, making motion detection very easy. However, the true strength of the motion detection scheme can perhaps be better appreciated when applied

onto the other subjects to be mentioned later in the chapter, who did not move as much as this subject.

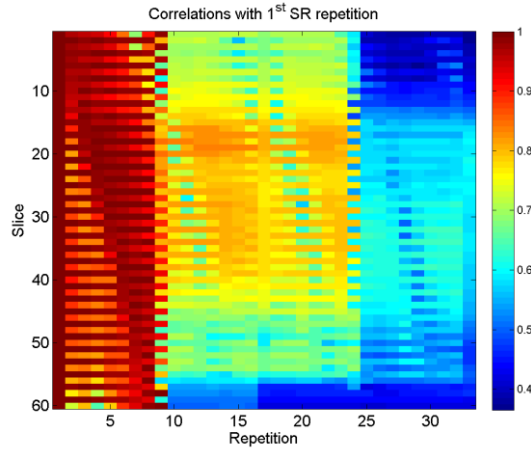


Figure 6.4 – Correlations with the first SR repetition

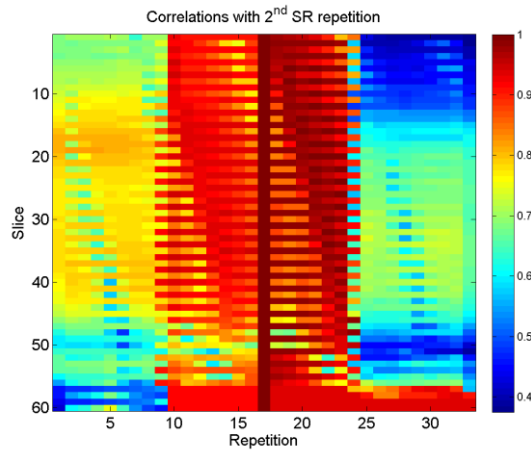


Figure 6.5 – Correlations with the second SR repetition

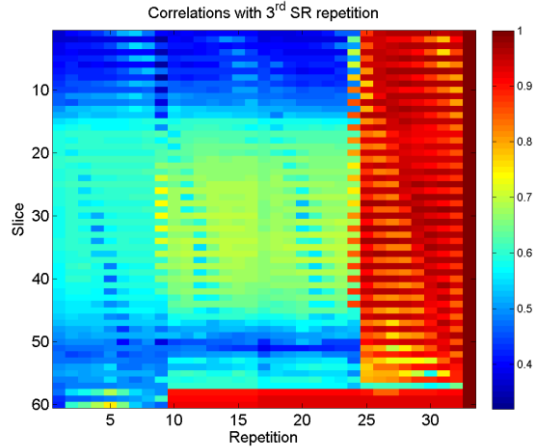


Figure 6.6 – Correlations with the third SR repetition

Figure 6.7 shows the images obtained by the proposed retrospective reconstruction. The artifacts are reduced except for Repetition 24 (row 4, column 3), which is a repetition of motion where some slices are acquired before, some are acquired after, and some are acquired during subject motion. The slice in Repetition 24 was acquired before motion. Therefore, the GRAPPA coefficients do not match. However, as mentioned before, the motion repetition and the repetition thereafter will be discarded during post-processing. Figure 6.8 shows a closer comparison. The bad-quality weight set on the left leads to not only ghosting, but also a slight location shift that can very well blur the resulting  $T_1$  map. It is, however, worth noting that the retrospective reconstruction can yield worse results at times.

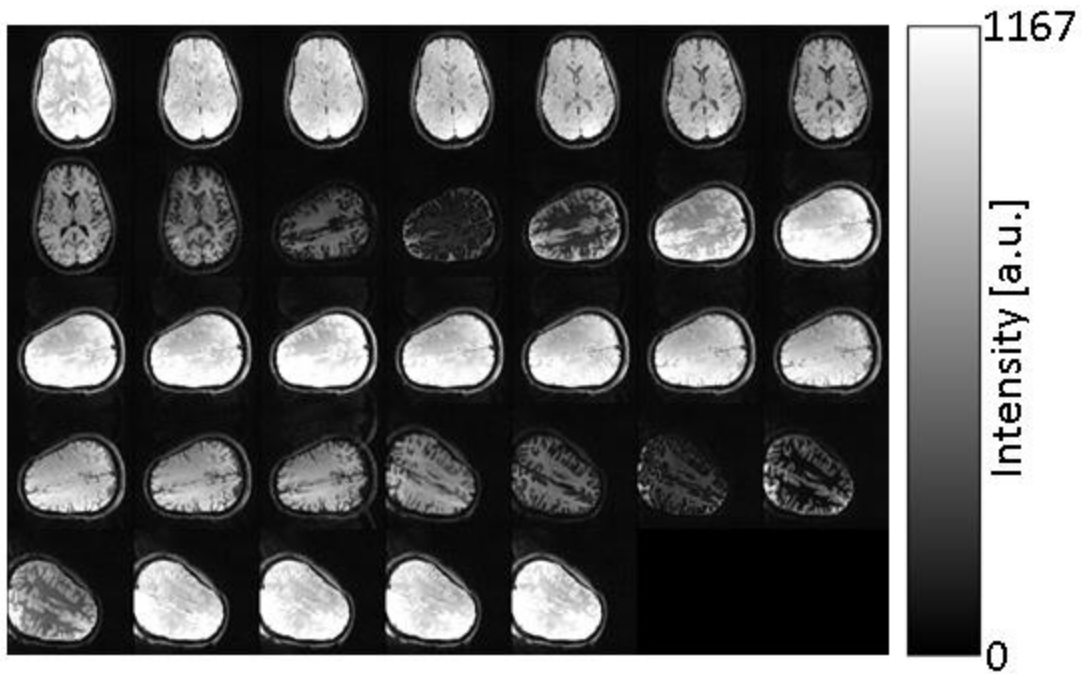


Figure 6.7 – The data set in Figure 6.3 after retrospective reconstruction

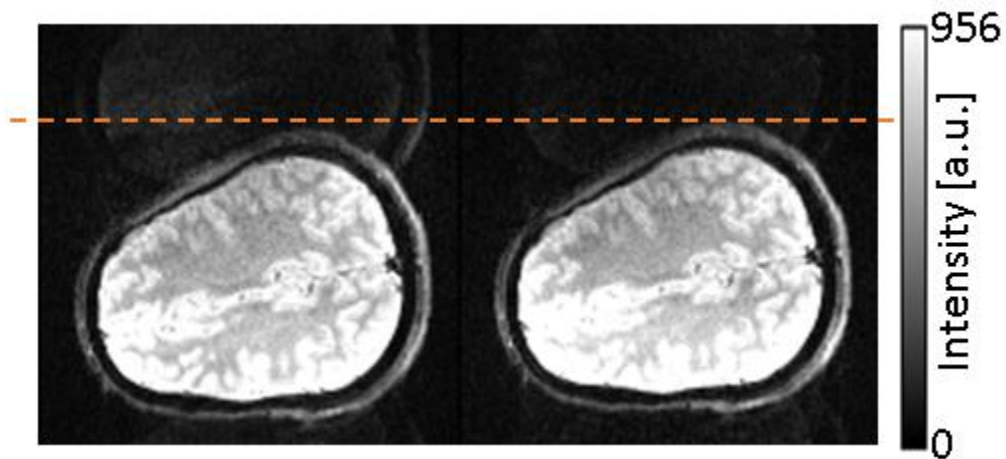


Figure 6.8 – Comparison at 13<sup>th</sup> image. The dashed orange line helps notice the shift of location.

For the 32-channel coil, possibly due to the high encoding capability with a higher number of channels, the amount of ghosting due to motion is less noticeable in most cases. However, it is important to note that the retrospective reconstruction works well only if the coefficients calculated during the SR repetitions are of good quality. It has been observed

that the updated coefficient set can, in some cases, yield worse results for no apparent reason. Figure 6.9 shows an example for this issue in three different slices while Figure 6.10 depicts the opposite on the images from the same repetition. Please note that no images are completely artifact-free, and, when all 60 slices are considered, the retrospective reconstruction yields a better result for the majority of the slices. Figure 6.11 exhibits the middle slice in Figure 6.9 together with the two temporally-adjacent slices. These slices were acquired in succession and the interslice time separation was only 66 milliseconds. It can be clearly seen that the artifact randomly hit the middle slice. The most plausible reason is that the GRAPPA weight set calculation is multi-threaded where synchronization is very critical. However, it is possible, and clearly advisable, to make this calculation single-threaded. As an additional precaution, the retrospective reconstruction can be easily modified to let the user make the weight set assignment in a slice-selective manner so that more than one weight set can be utilized for a single repetition to arrive at the best combination.

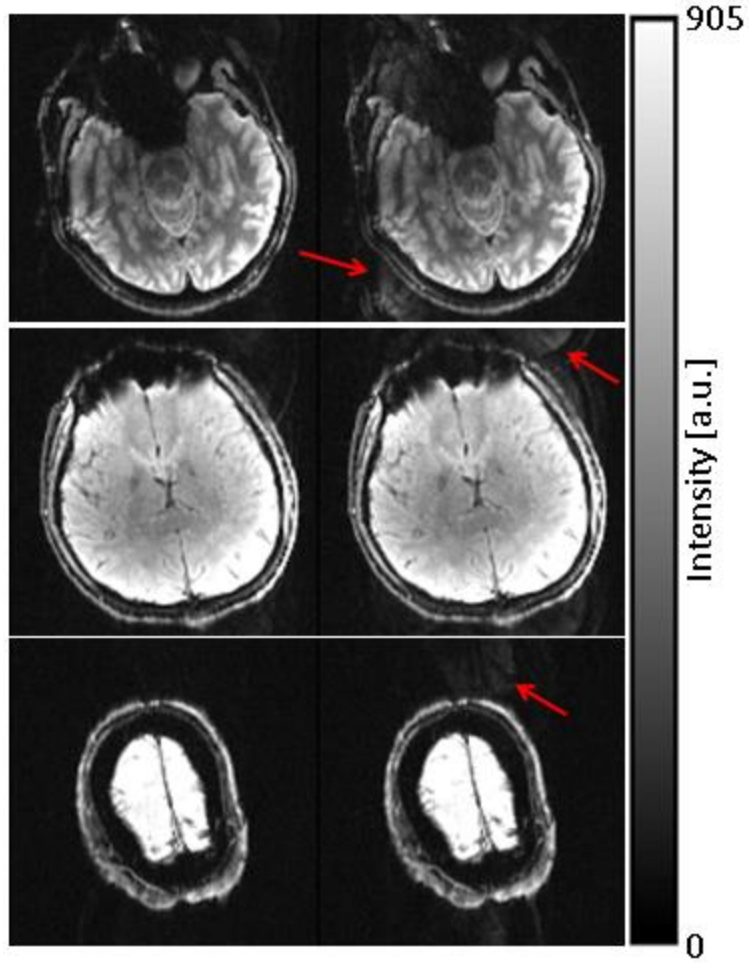


Figure 6.9 – Original (left) and retrospectively-reconstructed (right) images. The red arrows indicate the reconstruction artifacts

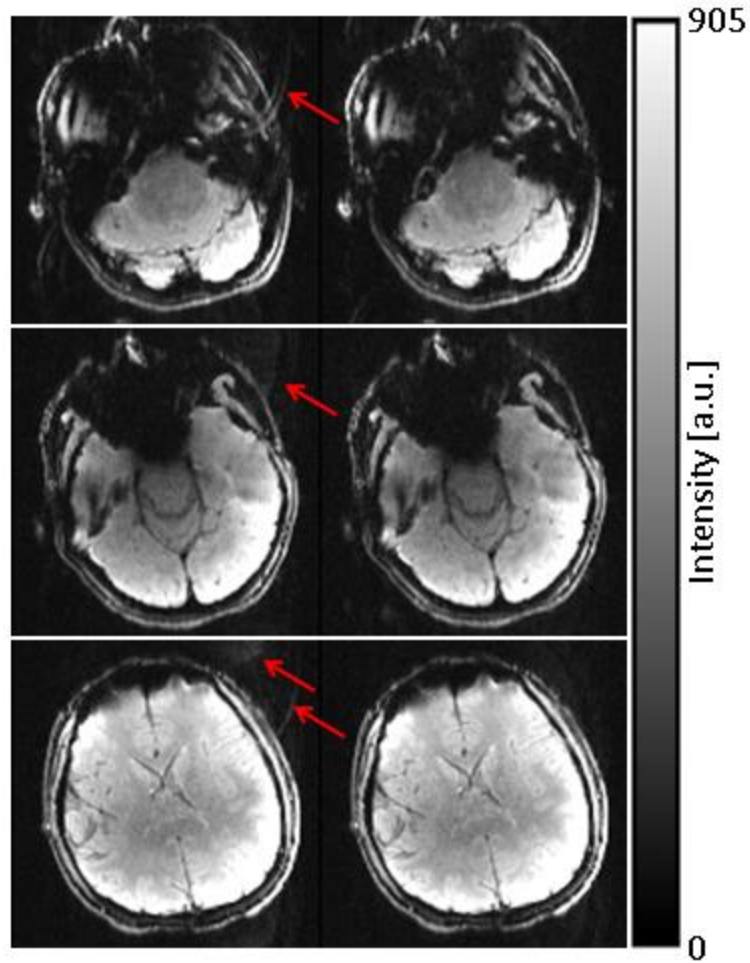


Figure 6.10 – Original (left) and retrospectively-reconstructed (right) images. The red arrows indicate the reconstruction artifacts

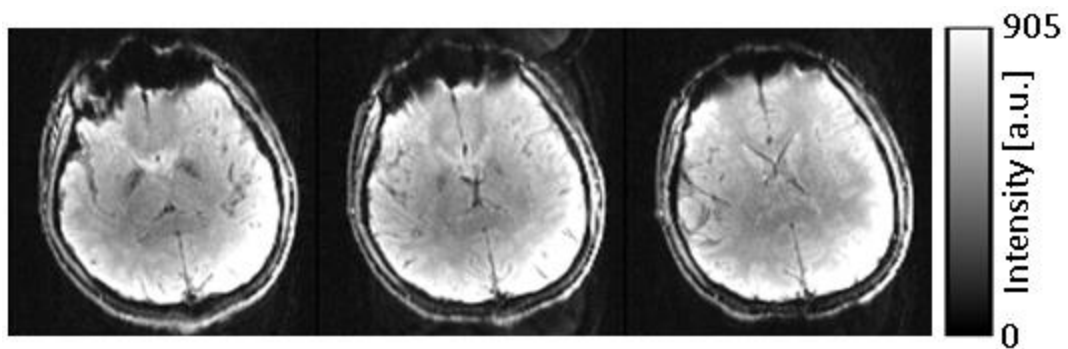


Figure 6.11 – Three consecutively-acquired slices from the retrospectively-reconstructed data set.

## 6.8 Motion relocates spins

The detailed retrospective reconstruction mentioned above aims at reducing the image artifacts that occur due to motion. In other words, the main objective of the retrospective reconstruction is to improve the quality of each individual image. Although this is valuable for good estimation, it does not account for the fact that spins in a given voxel may very well be relocated in the scanner frame of reference. If the spins appear on a different slice after motion, the magnetization pathway they follow will be completely altered, and this needs to be taken into account during curve-fitting.

Figure 6.12 illustrates how a spin can get relocated because of motion while Figure 6.13 depicts how different the magnetization pathways can be on two neighboring slices. The reason for such a significant difference is the fact that even slices are acquired before the odd slices and vice versa. Therefore, spatially adjacent slices are, in fact, temporally very far away from each other.

## 6.9 Spin tracking

The large difference observed in Figure 6.13 is a valuable reminder that, in the case of motion, the location of each individual spin needs to be tracked very carefully. This can be accomplished by the use of SR repetitions, as mentioned in Section 6.4.

The tracking procedure begins by registering the second and third SR images onto the first SR image using FSL's linear registration tool FLIRT (49,50). The registration is rigid with 6 degrees of freedom. The default correlation-based cost function is sufficient in many



source image space to its corresponding point in the target image space, or vice versa. This mapping is absolutely essential for spin tracking. In this respect, an in-house program was developed to calculate this correspondence. With the use of this tool, it is possible to find out to what position a given spin will be relocated. The magnetization pathway can then be modified to take this change into account.

Figure 6.14 presents an example of relocation for three spins on the same slice. It can be seen that the magnetization pathway can be heavily altered for some spins.

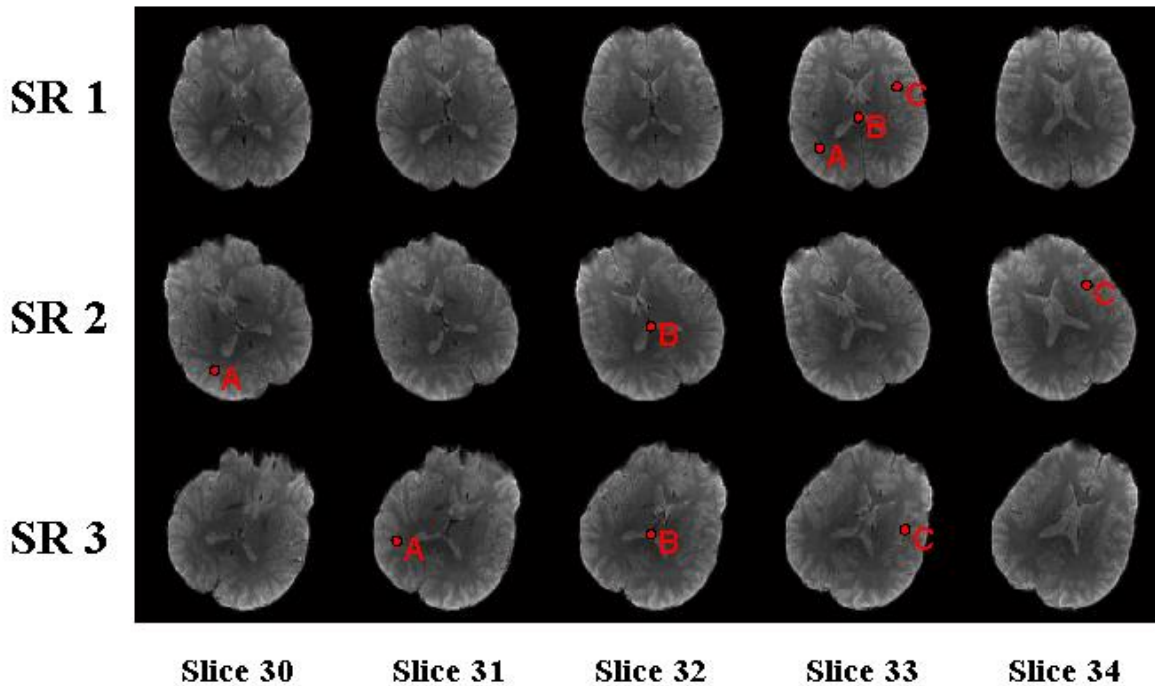


Figure 6.14 – Demonstration of spin relocation due to motion. A, B and C represent three spins on the same slice that get relocated on different slices after the subject moves once before and once after the second SR repetition.

Figure 6.15, on the other hand, indicates an alternative way of looking at the effect of motion. When all of the spins in the first SR image space are taken to the second and third SR image spaces by applying the appropriate transformations, it can be readily observed

from the banding that different portions of the slice of interest in the first SR repetition are relocated onto different slices in the later SR repetitions. This shows the importance of spin tracking for proper estimation.

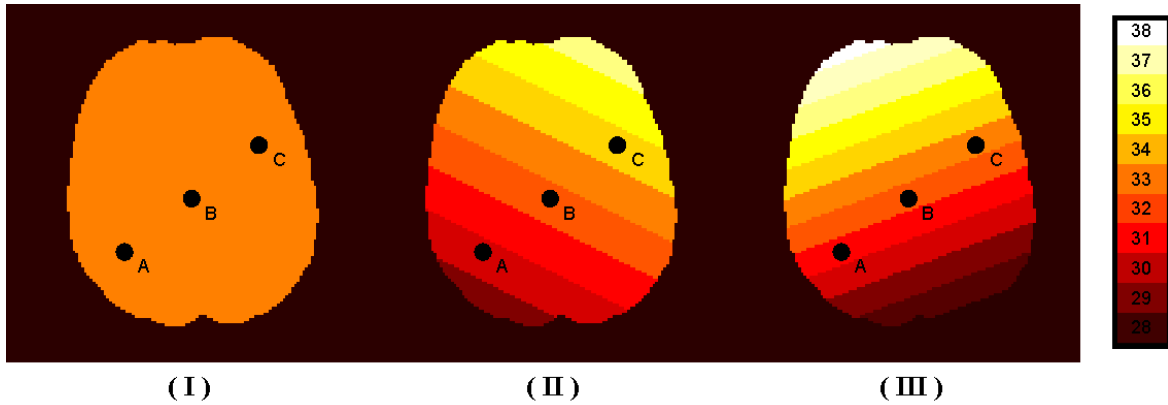


Figure 6.15 – Same spins as in Figure 6.14 with an alternative demonstration where the focus is slice relocation. After the first motion, the slice locations for A, B and C respectively become 30, 32 and 34. And after the second motion, the slice locations become 31, 32 and 33 in respective order.

Figure 6.16 plots the magnetization pathways for Spin A introduced in Figure 6.14. The figure draws a clear picture of how the spin switches from one magnetization pathway to the other as a result of motion. It is worth noting that Pathways 1 and 3 are very similar. This is because Slices 31 and 33 are temporally adjacent except for Repetition 30, in which case the signals are of opposite polarity but still similar in magnitude.

Once the magnetization pathways are identified for a given spin, the model equation used during least-squares fitting will be a composite one. For instance, again for Spin A, the blue pathway in Figure 6.16 will be used as the model for the measurements acquired before the 9<sup>th</sup> repetition. The red one will be used for Repetitions 10-23, and the green one will be used for Repetitions 25-33. Repetitions 9 and 24 will be discarded since the spin history gets

corrupted and becomes unpredictable at these repetitions. All of these error terms will be collected in a single vector of residuals, and the fitting algorithm will try to minimize the norm of this composite vector to arrive at a  $T_1$  estimate for Spin A.

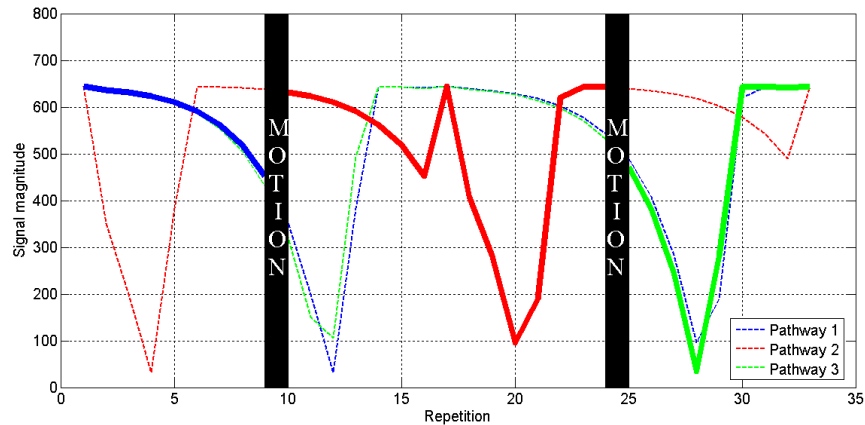


Figure 6.16 – Magnetization pathways for Spin A that was introduced in Figure 6.14

## 6.10 Experiments

Data was collected from four subjects with ages between 23 and 36 years. Written informed consent was obtained from all participants. Each subject has at least one scan with no motion. During the motion experiments, the subjects were asked to change the position of their heads at two different times: 1) About midway between SR1 and SR2, and 2) About midway between SR2 and SR3.

Table 6.1 lists the estimated motion parameters for the cases to be presented. Please note that FSL uses a left-handed coordinate system whose origin is centered at the lower-left voxel of the first slice in the volume. Therefore, the translation estimates may not seem intuitive.

	ROTATION 1 (deg)			TRANSLATION 1 (mm)			ROTATION 2 (deg)			TRANSLATION 2 (mm)		
	x	y	z	x	y	z	x	y	z	x	y	z
<b>Subject 1</b>	7	8	37	-32	72	-16	8	-1	-53	115	-43	21
<b>Subject 2</b>	1	0	-13	20	-21	2	12	2	6	-12	6	18
<b>Subject 3</b>	5	-2	22	-26	44	11	7	3	-32	64	-42	16
<b>Subject 4</b>	14	-10	98	38	225	6	10	17	-120	235	89	59

Table 6.1 – Estimated motion parameters for the cases to be presented

Case 1:

Figure 6.17 shows the motion pattern whereas Figure 6.18 shows the High5 correlations, according to which the motion detection scheme assigns Repetitions 1-10 to SR1, Repetitions 11-21 to SR2, and Repetitions 22-33 to SR3.

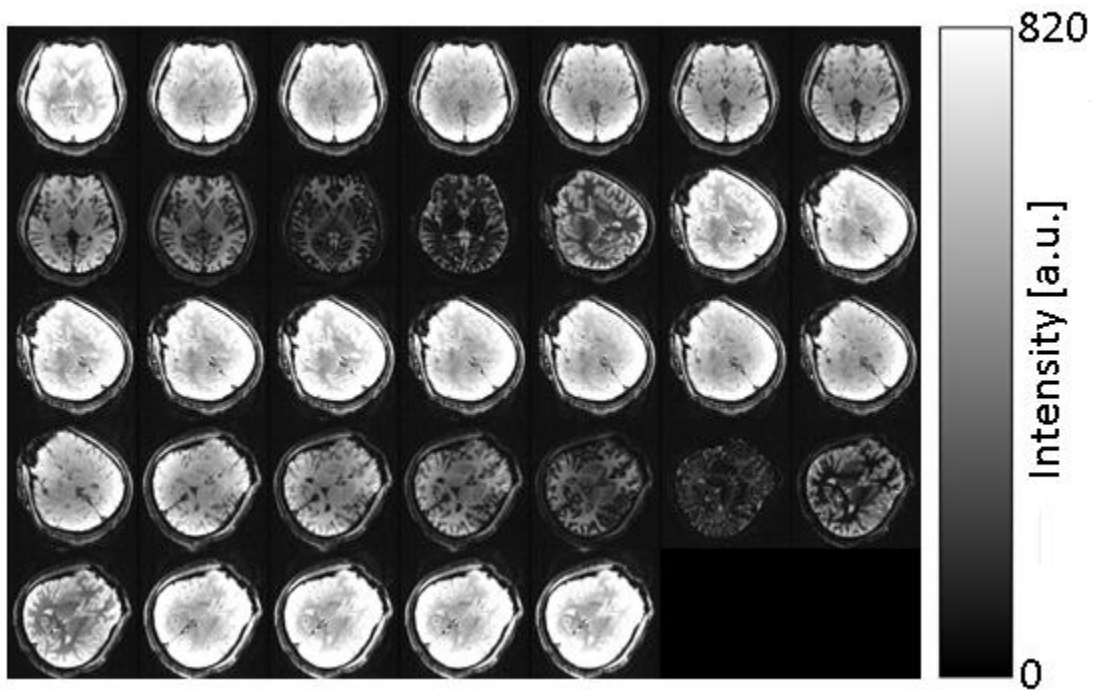


Figure 6.17 – Slice 29 across all repetitions

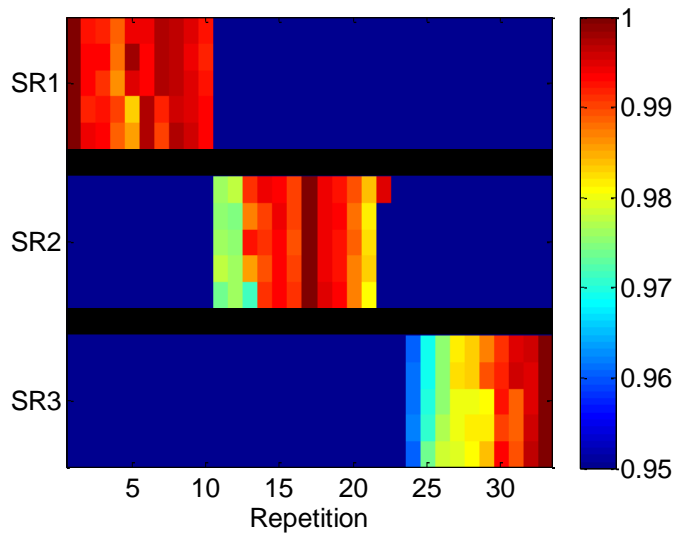


Figure 6.18 – High5 correlations with SRs across all repetitions

Figure 6.19 depicts the  $T_1$  maps for the cases with and without motion. It is worth noting that the images in the bottom row show a banded pattern due to motion. Figure 6.20 provides a clearer picture of this pattern. This issue will be dealt with in the next section, which introduces smoothing into the fitting procedure.

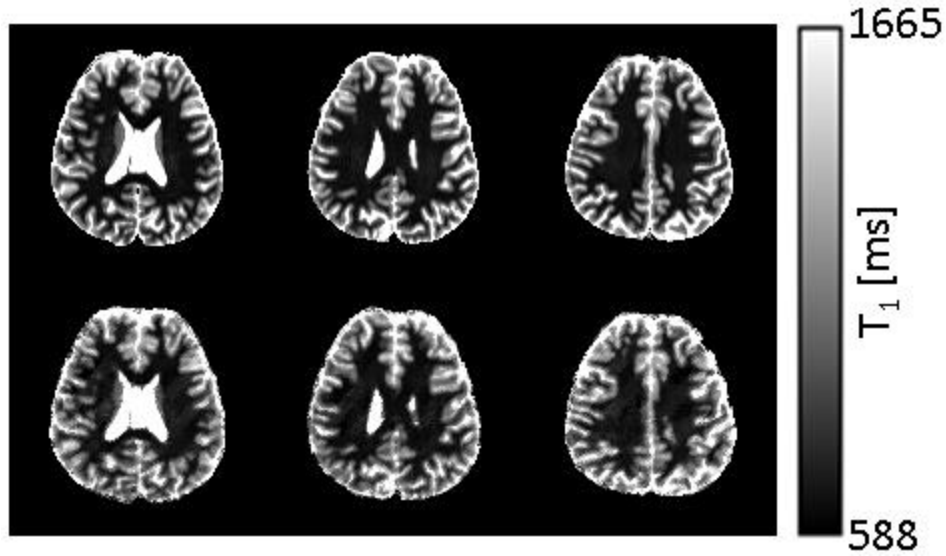


Figure 6.19 –  $T_1$  maps computed using the original (top) and motion-corrupted (bottom) data sets

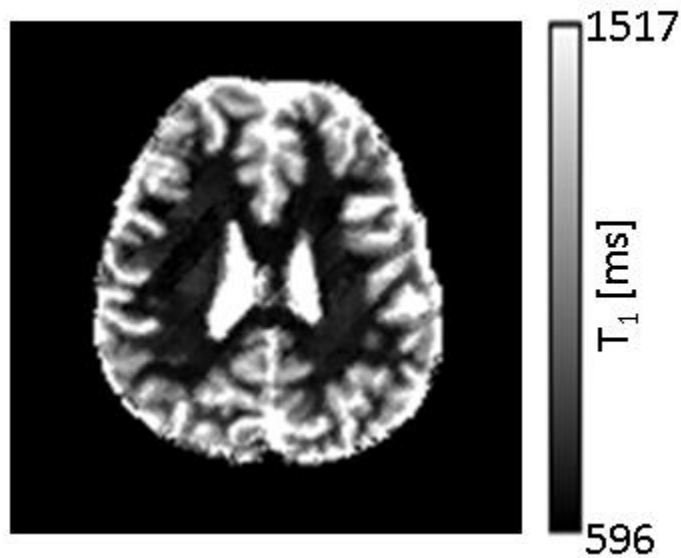


Figure 6.20 – A sample slice showing the banded pattern due to motion

Case 2:

Figure 6.21 shows the motion pattern whereas Figure 6.22 shows the High5 correlations, according to which the motion detection scheme assigns Repetitions 1-8 to SR1, Repetitions 9-24 to SR2, and Repetitions 25-33 to SR3.

Figure 6.23 depicts the  $T_1$  maps for the cases with and without motion. No banding is seen for this case, but rather a black-pepper like noise pattern is observed, as Figure 6.24 shows. Figure 6.25 exhibits the cost functions for a well-behaved voxel and a noise-like voxel. It can be seen that the noise-like voxel has two local minima rather than one. The motion seems to have introduced some irregularity into the cost function. The smoothing operation to be introduced in the next section is going to alleviate this problem to some extent.

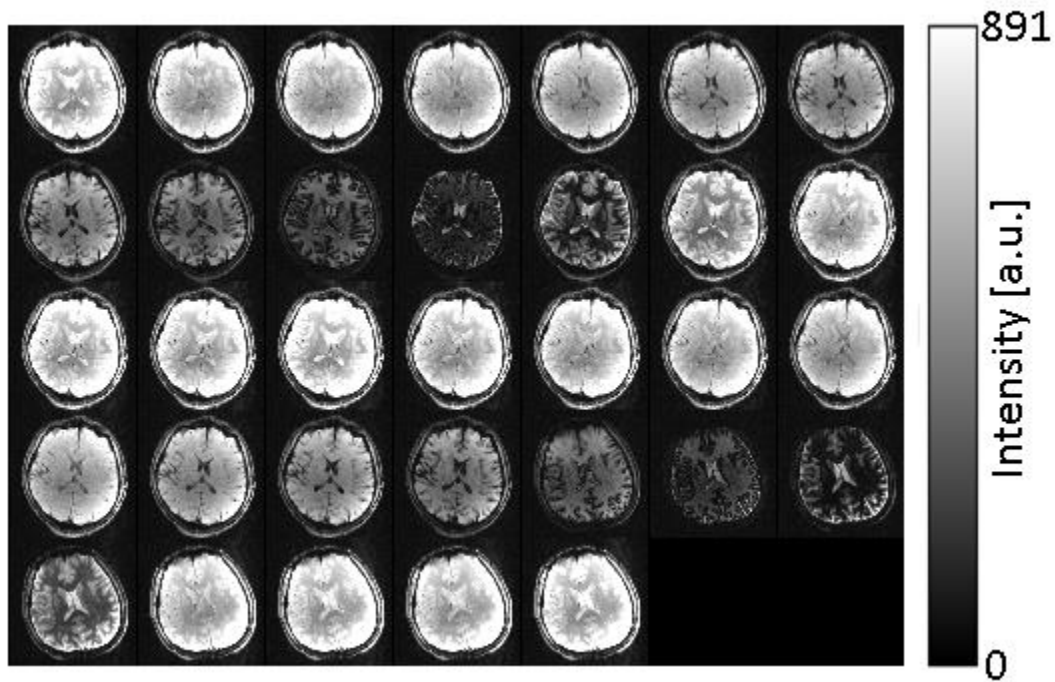


Figure 6.21 – Slice 31 across all repetitions

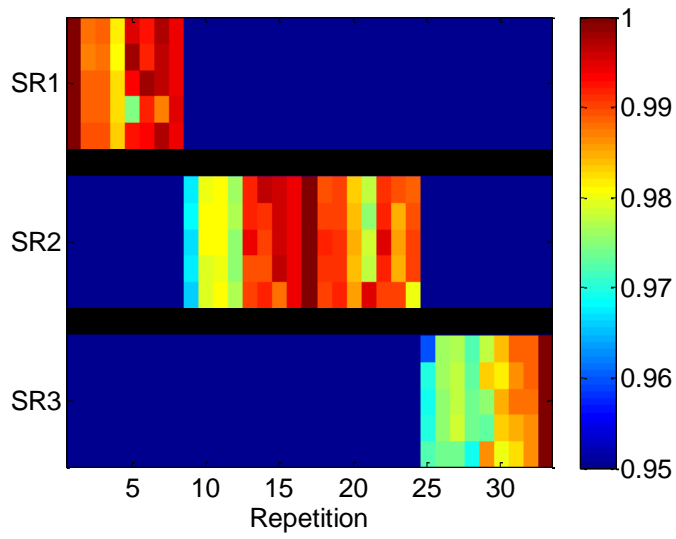


Figure 6.22 – High5 correlations with SRs across all repetitions

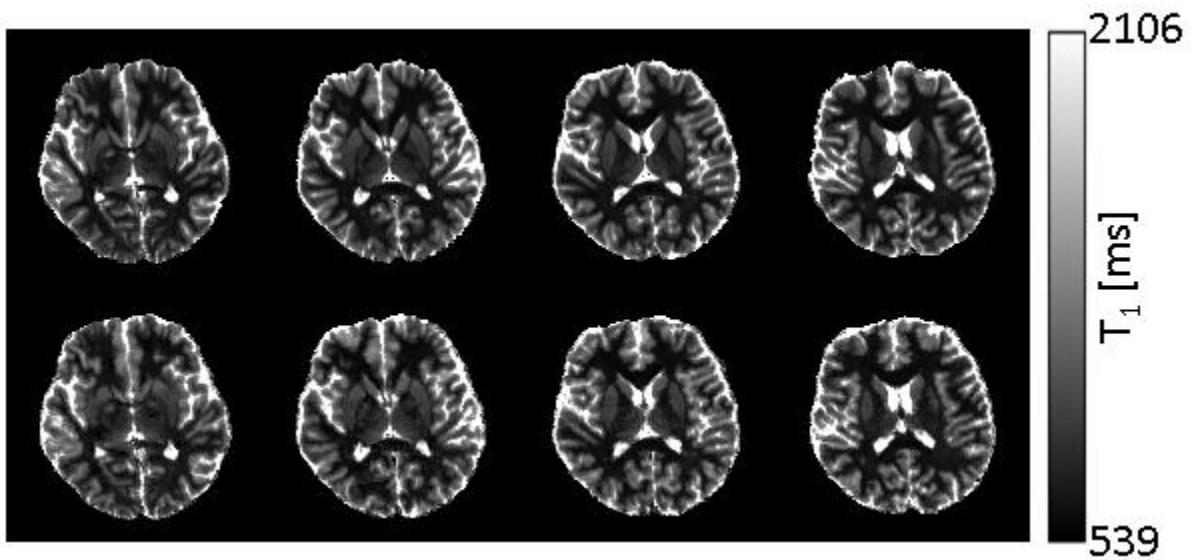


Figure 6.23 –  $T_1$  maps computed using the original (top) and motion-corrupted (bottom) data sets

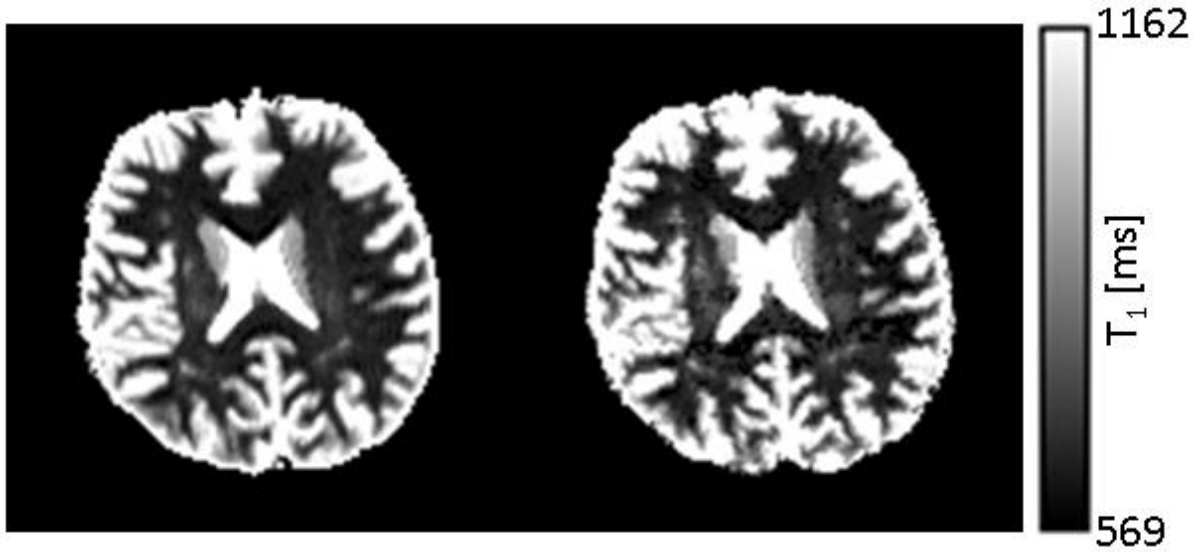


Figure 6.24 – Comparison of the  $T_1$  maps computed using the original (left) and motion-corrupted (right) data sets. A single slice is shown for better visualization

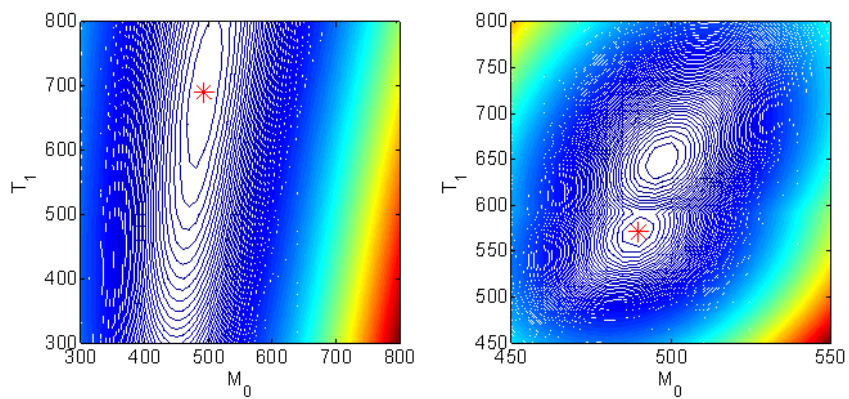


Figure 6.25 – Cost functions for a well-behaved voxel (left) and a noise-like voxel (right). The fitting algorithm converged to the points indicated by the red asterisks.

Case 3:

Figure 6.26 shows the motion pattern, whereas Figure 6.27 shows the High5 correlations, according to which the motion detection scheme assigns Repetitions 1-8 to SR1, Repetitions 9-23 to SR2, and Repetitions 24-33 to SR3.

Figure 6.28 depicts the  $T_1$  maps for the cases with and without motion.

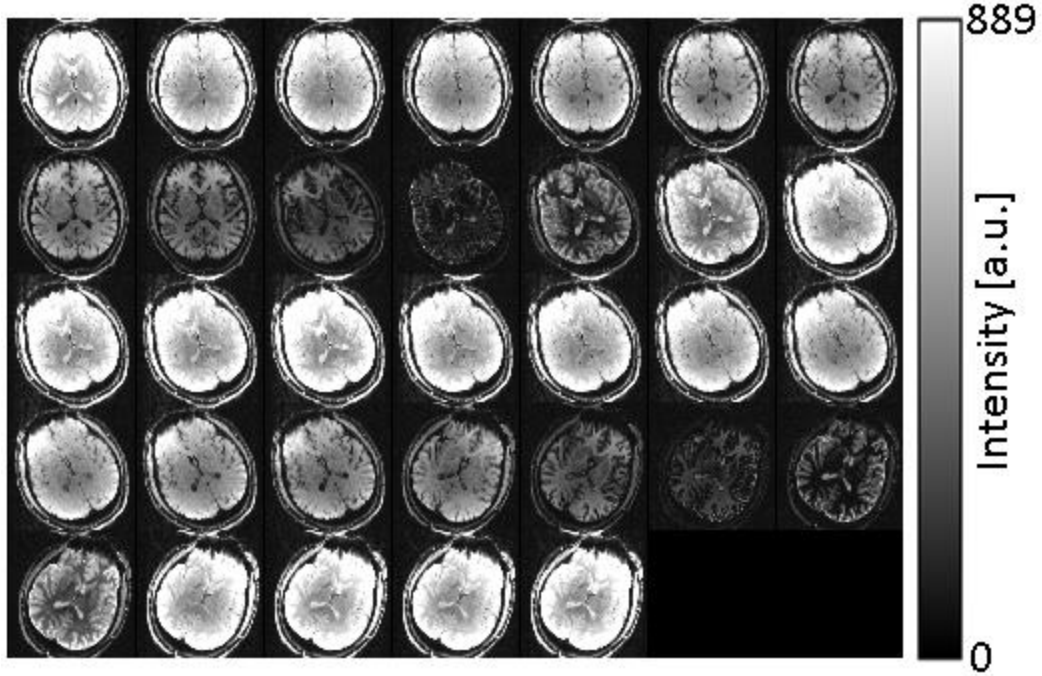


Figure 6.26 – Slice 31 across all repetitions

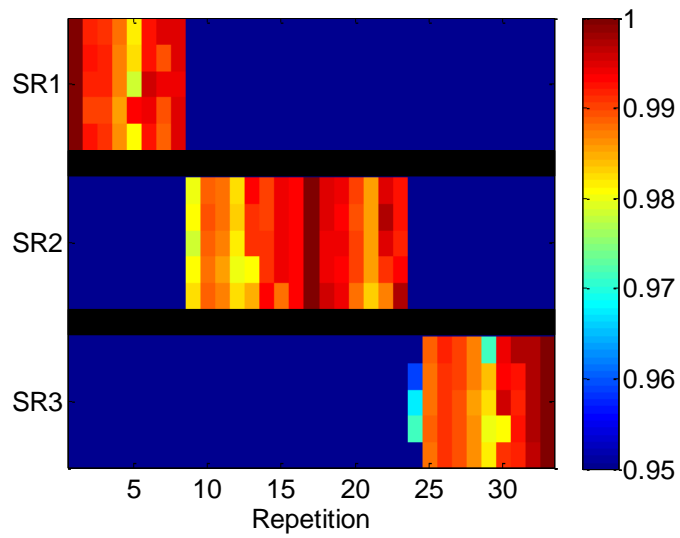


Figure 6.27 – High5 correlations with SRs across all repetitions

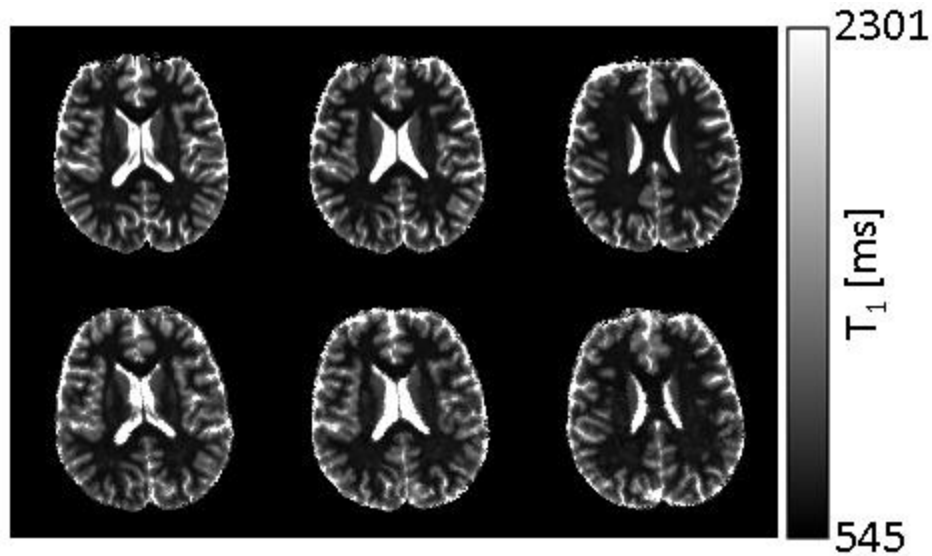


Figure 6.28 –  $T_1$  maps computed using the original (top) and motion-corrupted (bottom) data sets

The maps computed using the motion-corrupted data set manifest some pixelation, as Figure 6.29 indicates. The smoothing operation to be introduced in the next section is going to alleviate this problem as well to some extent.

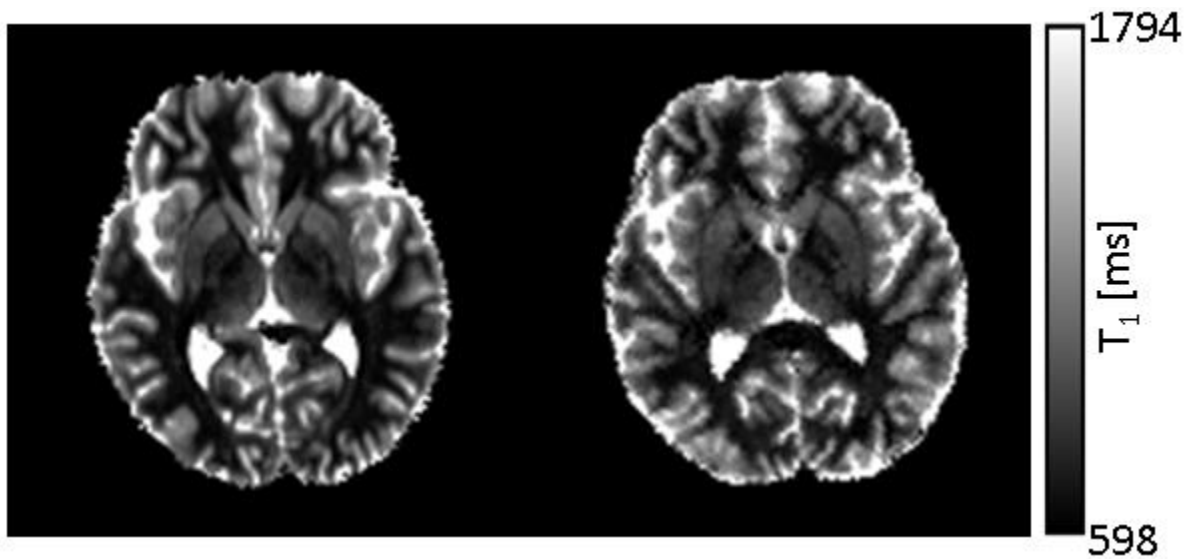


Figure 6.29 – Comparison of the  $T_1$  maps computed using the original (left) and motion-corrupted (right) data sets. A single slice is shown for better visualization.

Case 4:

This case was the most challenging one. Figure 6.30 shows the motion pattern, whereas Figure 6.31 shows the High5 correlations, according to which the motion detection scheme assigns Repetitions 1-8 to SR1, Repetitions 9-23 to SR2, and Repetitions 24-33 to SR3. Please note that, due to the large amount of motion, even the High5 correlation values fall below 95%. This is why Figure 6.31 shows a great deal of dark blue regions. Figure 6.32 displays the same correlations, but with a wider display window so that the values below 95% become visible.

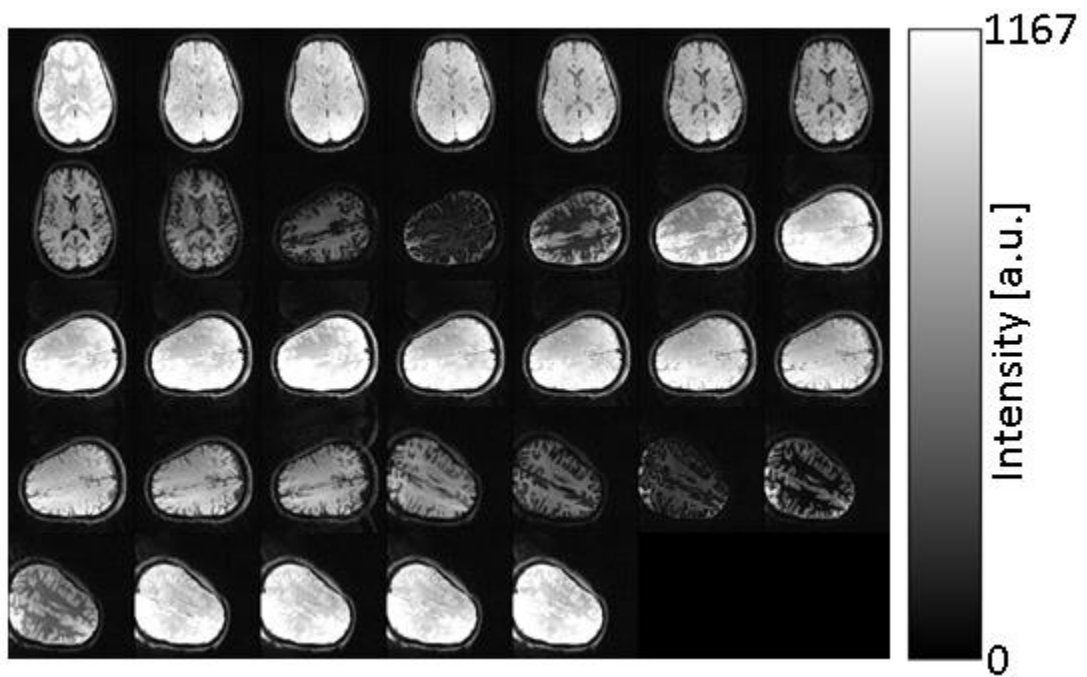


Figure 6.30 – Slice 31 across all repetitions

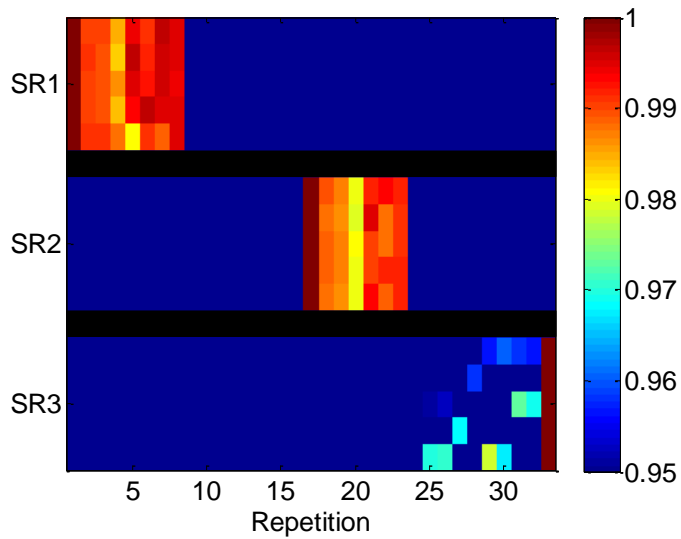


Figure 6.31 – High5 correlations with SRs across all repetitions

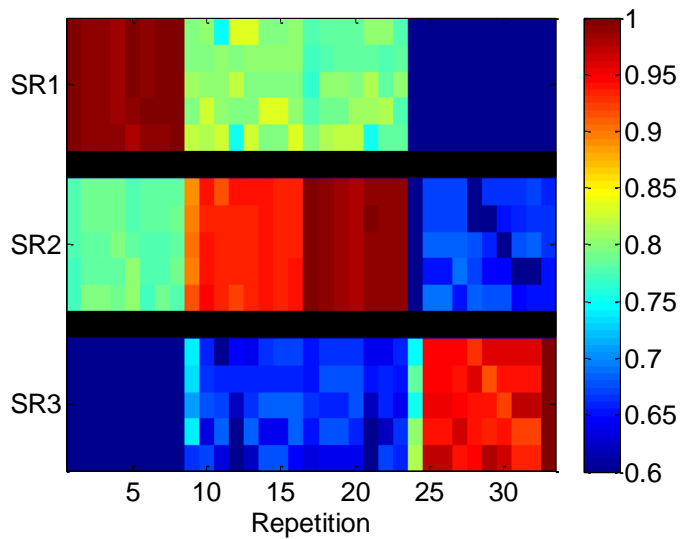


Figure 6.32 – High5 correlations with a different display window

Figure 6.33 depicts the  $T_1$  maps for the cases with and without motion. It can be seen that, even in this difficult situation, the postprocessing scheme was able to get similar  $T_1$  maps. However, it is worth noting that the banded pattern in this case is even stronger compared to Case 1. The smoothing scheme in the next section offers a remedy for this case as well.

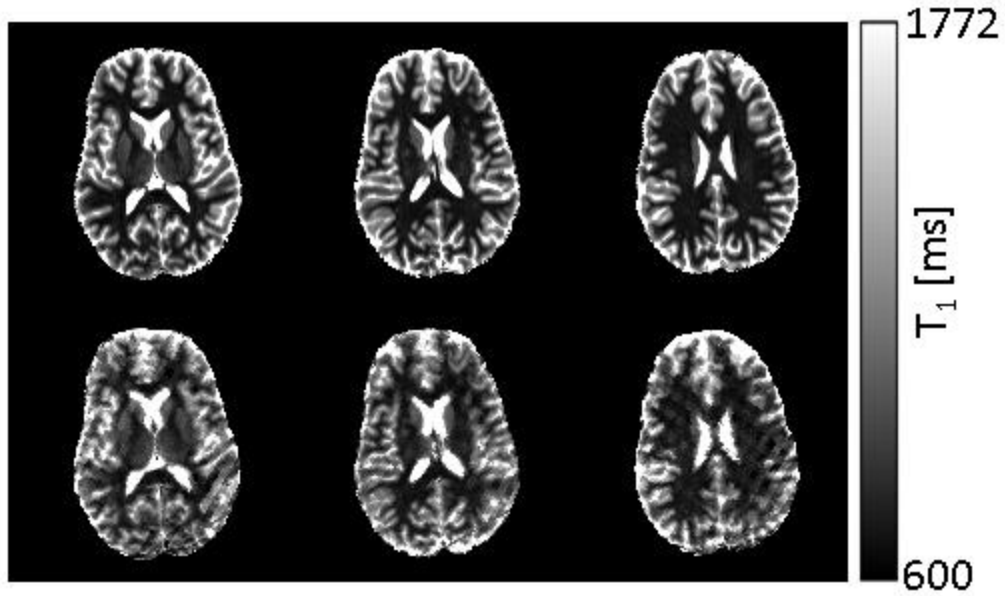


Figure 6.33 –  $T_1$  maps computed using the original (top) and motion-corrupted (bottom) data sets

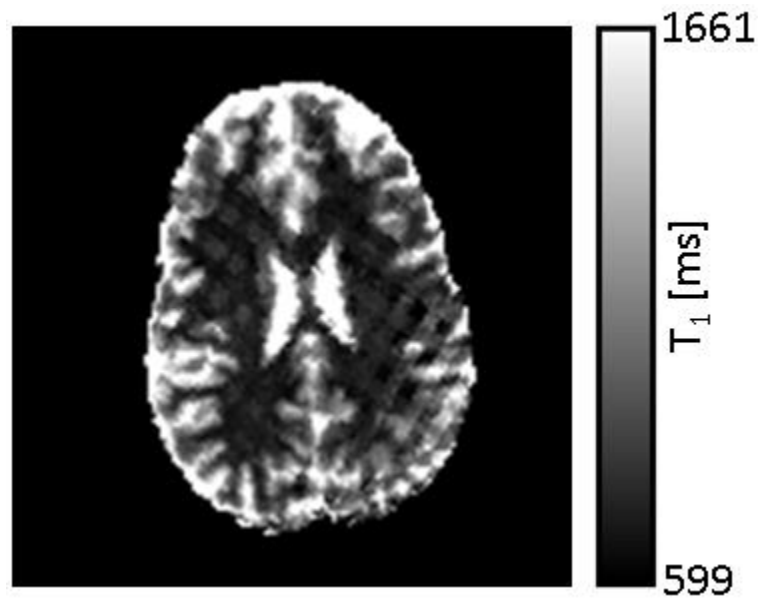


Figure 6.34 – A sample slice showing the banded pattern due to motion. The banding in this case is in two different directions.

Please note that all four cases presented so far manifested bulk motion that could relocate a voxel well beyond the neighboring slices. If the subject moved such that a higher percentage of any given voxel remains in that voxel's original slice, the fitting routine would

process the data as if no motion occurred, because such small motion would be below the detectable threshold while quantizing the voxels by slice. Considering the fact that any given pair of neighboring slices go through very different magnetization pathways, the  $T_1$  estimate for a voxel that dwells upon two adjacent slices after motion would be erroneous, with the amount of error depending on the percentage of the voxel leaving the original slice – the higher the percentage, the higher the error. Sub-voxel smoothing, to be detailed in the next section, is a beautiful remedy for this problem because, in that scheme, the voxels are allowed to be split into a number of sub-voxels that can go through many different magnetization pathways.

### **6.11 Sub-voxel smoothing**

The estimation procedure described so far treated each voxel as a single spin and tracked its trajectory accordingly. However, the spins in the same voxel may show up in different voxels after motion. Therefore, treating the whole voxel as a single spin might be very erroneous as shown by the results in the previous section. In this respect, it is more reasonable to represent each voxel as a 3D lattice of spins.

Figure 6.35 shows various lattice configurations. The single-spin configuration in Figure 6.35 (a) is the configuration that was used in the previous section.

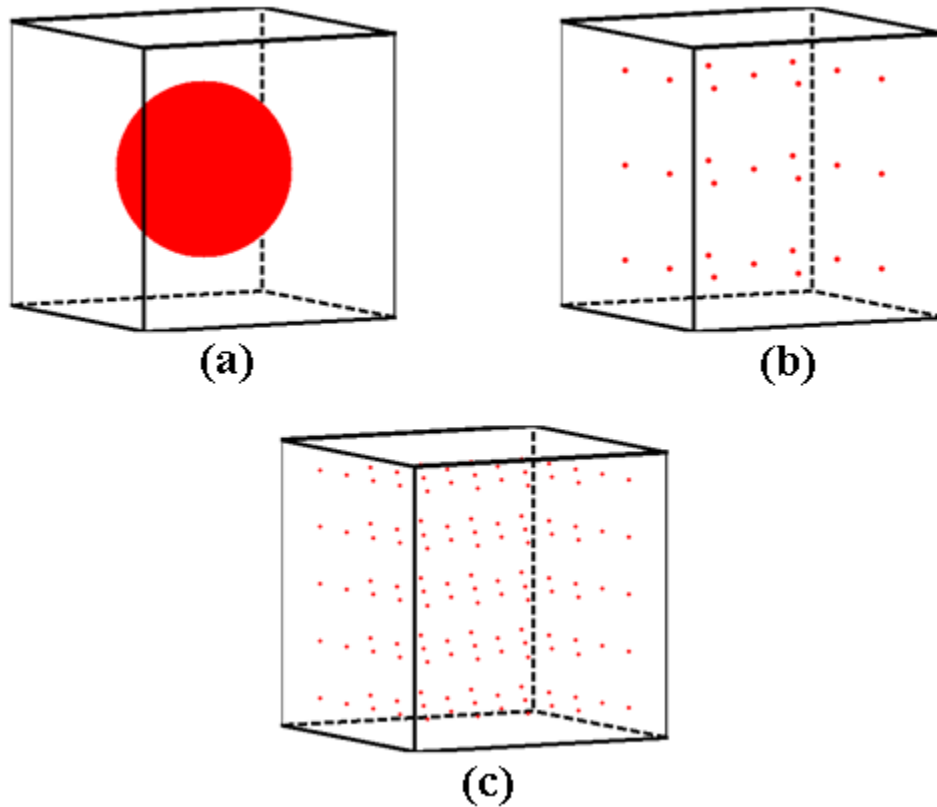


Figure 6.35 – Lattice configurations for a single spin (a), for  $3 \times 3 \times 3 = 27$  spins (b) and for  $5 \times 5 \times 5 = 125$  spins (c)

It should be emphasized that each individual spin will be treated separately while applying the rigid transformations. This way, it will be possible for the spins in a voxel to fall into separate voxels after motion, which is certainly more realistic.

Let  $N_{SpinsPerDim}$  denote the number of spins along a single dimension so that the total number of spins in a given voxel,  $N_{Spins}$ , will be given by  $N_{SpinsPerDim} \times N_{SpinsPerDim} \times N_{SpinsPerDim}$ . The lattice configurations in Figure 6.35 were thus for  $N_{SpinsPerDim} = 1, 3,$  and  $5,$  respectively. During model fitting,  $M_0$  will be replaced with  $M_0$  divided by  $N_{Spins}$  while computing the cost for each individual spin, whereas the  $T_1$  value of each spin will be the same as the  $T_1$  value

for the whole voxel – allowing for no partial volume effects. This is for the model equation. As for the measurements to be used as the target during model fitting, if an individual spin is found to fall into a voxel with intensity  $I$  after motion, the target value will be set to  $I$  divided by  $N_{Spins}$ . With the modeled and the target values at hand, the costs of all spins will be summed up, and this sum will be minimized to arrive at the  $(M_0, T_1)$  pair for the voxel of interest that originally encapsulated all those  $N_{Spins}$  spins. One could imagine that the vector of residuals would be  $N_{SpinsPerDim} \times N_{SpinsPerDim} \times N_{SpinsPerDim}$  times larger than the original scheme detailed in Section 6.9; however, the cost function still has only a single pair of parameters to estimate –  $M_0$  and  $T_1$ .

Figure 6.36 demonstrates a beautiful example – motion distributes the spins in the same voxel into 6 different voxels in 2 different slices. Please note that the subject rotated his head about more than one axes. This is why the bottom slices do not look like the slice in the upper left corner.

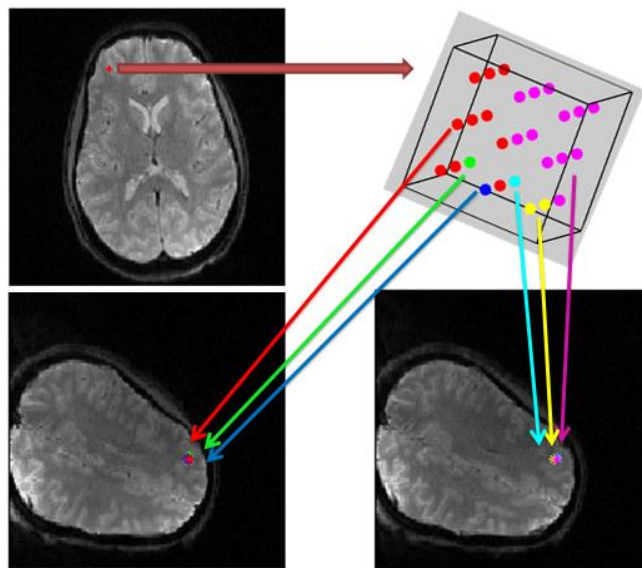


Figure 6.36 – Redistribution of same-voxel spins into 6 different voxels in 2 different slices after motion

Figures 6.37-40 show the alleviation of the problems mentioned in the previous section by the proposed sub-voxel smoothing scheme. As expected, the images computed from motion-corrupted data sets are not as high-quality as the ones computed from motion-free data. However, even in the harshest scenario, namely Case 4, sub-voxel smoothing provides significant improvement.

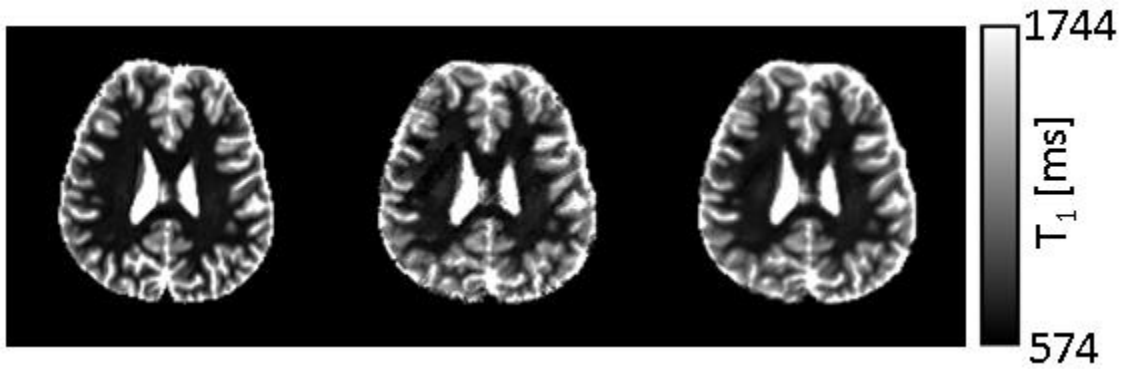


Figure 6.37 – Case 1: Motion-free (left), Motion-corrupted with  $N_{Spins}=1$  (middle), Motion-corrupted with  $N_{Spins}=3$  (right)

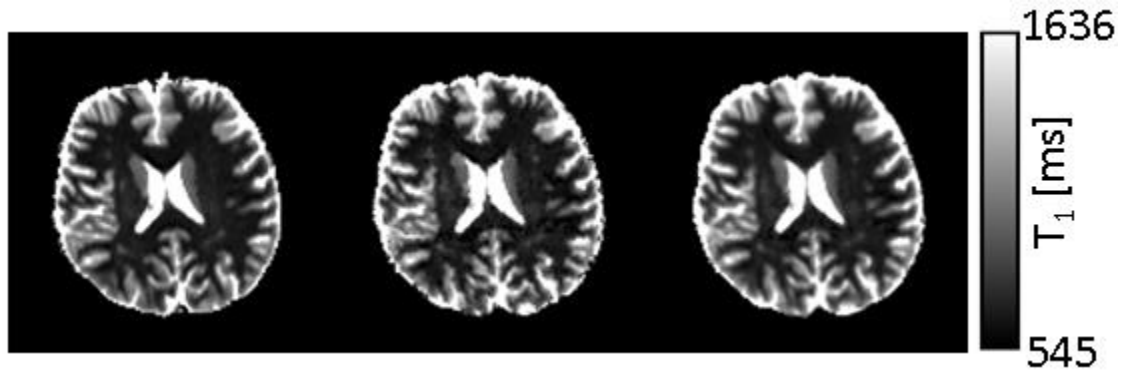


Figure 6.38 – Case 2: Motion-free (left), Motion-corrupted with  $N_{Spins}=1$  (middle), Motion-corrupted with  $N_{Spins}=3$  (right)

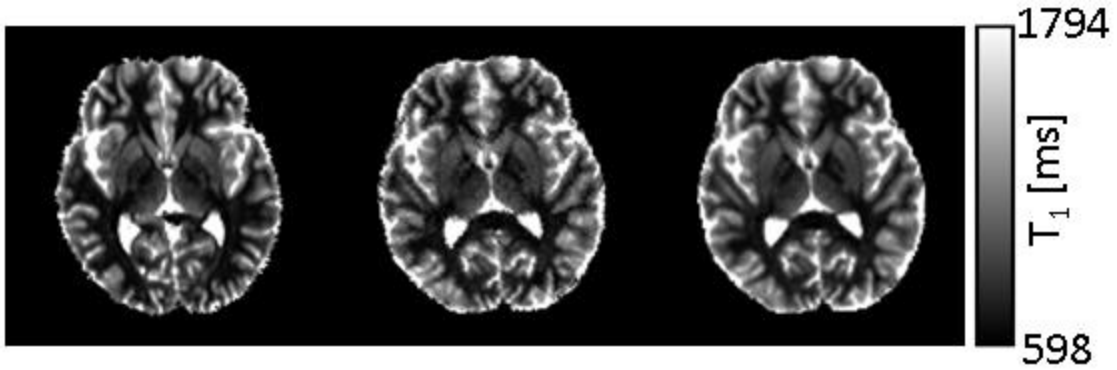


Figure 6.39 – Case 3: Motion-free (left), Motion-corrupted with  $N_{Spins}=1$  (middle), Motion-corrupted with  $N_{Spins}=3$  (right)

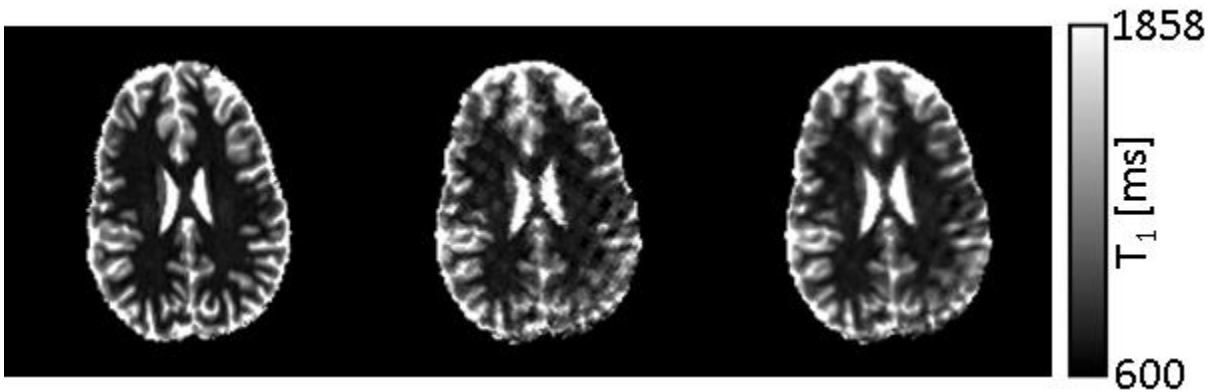


Figure 6.40 – Case 4: Motion-free (left), Motion-corrupted with  $N_{Spins}=1$  (middle), Motion-corrupted with  $N_{Spins}=3$  (right)

What would happen if  $N_{Spins}$  was set to 5? Figure 6.41 compares  $N_{Spins}=3$  and  $N_{Spins}=5$ . It can be seen that they are almost identical. This is a case of diminishing returns because, as  $N_{Spins}$  is increased, the computation time increases substantially. Figure 6.42 provides a comparison of 60-slice computation times for  $N_{Spins}=1, 3,$  and  $5$ . It is clear that the gain in image quality is very little relative to the very long computation time.

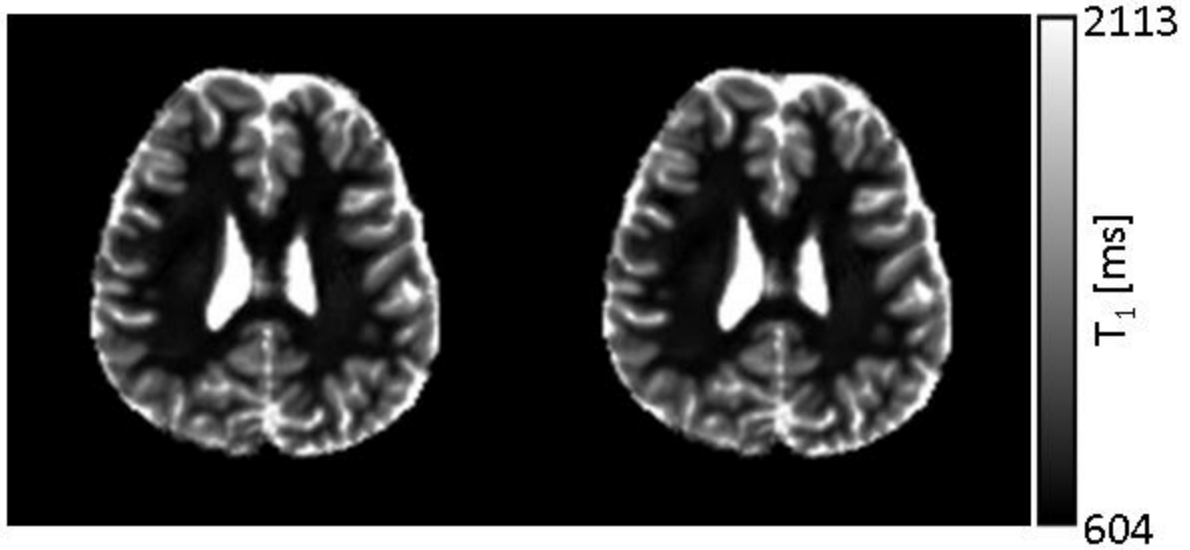


Figure 6.41 – Case 1: Motion-corrupted with  $N_{Spins}=3$  (left), Motion-corrupted with  $N_{Spins}=5$  (right)

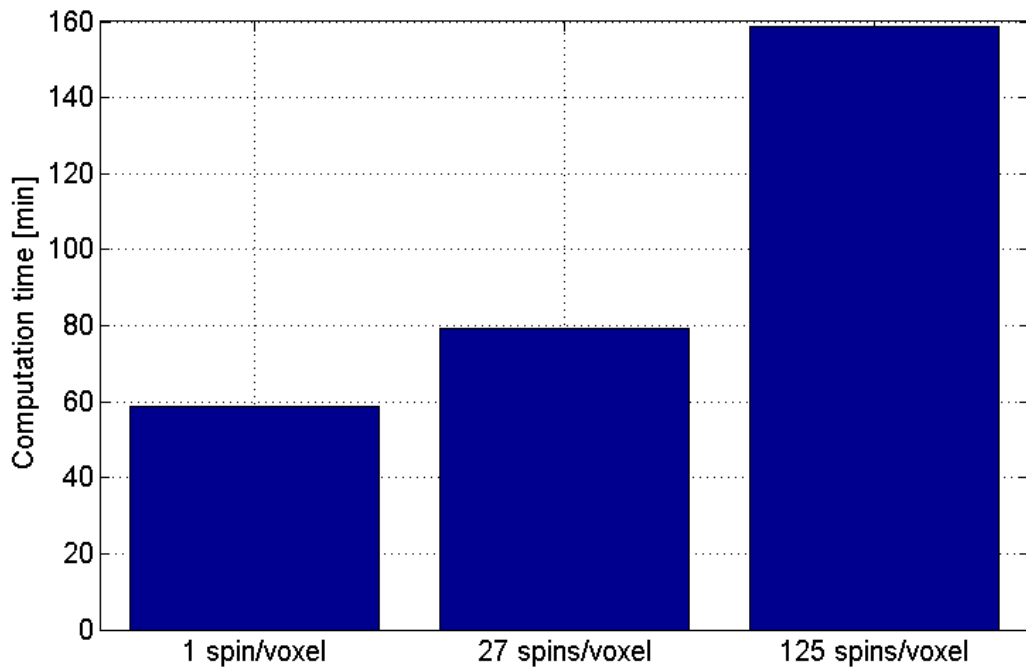


Figure 6.42 – Computation times for Case 1: Motion-corrupted with  $N_{Spins}=1$  (left), Motion-corrupted with  $N_{Spins}=3$  (middle), Motion-corrupted with  $N_{Spins}=5$  (right)

Tables 6.2, 6.3, 6.4, 6.5, and 6.6 show the result of repeated measurements together with the results of spin tracking and sub-voxel smoothing. Subject 4 did not have repeated measurements. It can be seen that the results in the case of motion are quite reasonable.

	T1 in White Matter [ms]					
	No motion				Motion	
	Run1	Run2	Run3	Run4	Nspins=1	Nspins=27
Subject 1	651	639	626	653	656	657
Subject 2	621	622	644	625	627	627
Subject 3	655	656	646	655	658	658
Subject 4	687				721	690

Table 6.2 – T<sub>1</sub> measurements in white matter

	T1 in Putamen [ms]					
	No motion				Motion	
	Run1	Run2	Run3	Run4	Nspins=1	Nspins=27
Subject 1	930	913	908	933	937	939
Subject 2	901	902	889	907	910	909
Subject 3	905	905	892	904	908	878
Subject 4	906				909	910

Table 6.3 – T<sub>1</sub> measurements in putamen

	T1 in Thalamus [ms]					
	No motion				Motion	
	Run1	Run2	Run3	Run4	Nspins=1	Nspins=27
Subject 1	868	883	876	871	875	876
Subject 2	839	840	828	813	847	847
Subject 3	843	843	861	842	845	846
Subject 4	843				847	847

Table 6.4 – T<sub>1</sub> measurements in thalamus

	T1 in Caudate [ms]					
	No motion				Motion	
	Run1	Run2	Run3	Run4	Nspins=1	Nspins=27
<b>Subject 1</b>	1054	1035	1002	996	1000	1002
<b>Subject 2</b>	994	995	981	969	1035	1035
<b>Subject 3</b>	967	968	953	966	971	972
<b>Subject 4</b>	1031				972	972

Table 6.5 – T<sub>1</sub> measurements in caudate

	T1 in Cerebrospinal Fluid [ms]					
	No motion				Motion	
	Run1	Run2	Run3	Run4	Nspins=1	Nspins=27
<b>Subject 1</b>	4247	4323	4288	4294	4436	4382
<b>Subject 2</b>	4443	4198	4047	4126	4141	4045
<b>Subject 3</b>	4307	4277	4182	4301	4008	3887
<b>Subject 4</b>	4279				4171	4047

Table 6.6 – T<sub>1</sub> measurements in cerebrospinal fluid

## CHAPTER 7: SUMMARY AND CONCLUSION

### 7.1 Major contributions

In this study, we proposed a new sequence for whole-brain  $T_1$  mapping. The sequence inherits from the recently-proposed slice reordering methods in order to speed up acquisition. Although speed was one of the objectives, we also put emphasis on accuracy and robustness to motion because, without these two in place, speed by itself has very little to offer.

The slice reordering methods proposed so far depended only on inversion recovery (IR). However, high speed acquisition inherently puts a constraint on how far longitudinal relaxation can take place, and this limits the dynamic range of the experiment, and hence the accuracy. In our sequence, we also included saturation recovery (SR) samples to alleviate this limitation. Phantom data with and without the SR samples justified the usefulness of this addition.

The first thing we did for robustness to motion was introducing a segmented structure so that if the subject moved in one segment, the other segment could still be useful together with what could be salvaged from the motion corrupted segment. The problem was that the reconstruction parameters had to be updated with respect to the new position of the patient; otherwise, if the motion was early in the scan, even the segmented structure could provide no help. As a solution to this problem, SR samples were placed at the beginning of each segment together with calibration scans that updated the reconstruction parameters before each SR

sample. Nevertheless, even this was not enough. Yes, the beginning portion of each segment was being reconstructed properly, but, if the subject moved in the middle of a segment, the portion of the segment after the motion still had to be discarded. This is where the retrospective application of the reconstruction parameters proved useful. The user could now apply the parameters obtained by a calibration scan to the repetitions before that scan. This could salvage the post-motion data within the first segment, but the post-motion data within the second segment still had to be discarded. At this point, a third calibration scan placed at the end of the second segment provided the healthy parameters for the repetitions that would otherwise be discarded. The SR repetitions preceded by the calibration scans and the retrospective application of the reconstruction parameters make our sequence unique.

Mitigating the effects of motion on the reconstructed images was one issue. However, the ultimate goal was to obtain reliable estimates of  $T_1$ , even in the case of motion. Simple rigid registration of the images was not a solution because the spin history was being altered as a result of motion. At this point, it was more prudent to track the changes in the magnetization pathway of each spin and to do the estimation accordingly. An in-house program was developed to find the new coordinates of each voxel after motion, and a composite model function was used to match the measurements collected through different magnetization pathways. The results were promising; however, since the voxels were being quantized by slices, the effects of this quantization were visible in the resulting images. Visualizing a voxel as a lattice of subvoxels, or spins, was the remedy for this issue. This would cause some blurring in the images, but would also fix quantization errors. This postprocessing scheme is another thing that adds to the uniqueness of our method.

## 7.2 Clinical applications

Many things can be done with a good quality  $T_1$  map. Among numerous clinical applications, brain tissue segmentation is an immediate one.

$T_1$ -weighted images are routinely used in order to do tissue segmentation. Typically, these images are acquired with high resolution –  $1 \text{ mm} \times 1 \text{ mm} \times 1 \text{ mm}$ . However, when automatic segmentation is performed, subcortical structures such as the putamen and the thalamus are not very well discriminated from the white matter, due to noise and intensity variations that exist even after bias field removal. At this point, the proposed  $T_1$ -mapping technique provides an improvement over the  $T_1$ -weighted images. This is perhaps because the intensity variations are mostly absorbed into the second parameter in the fitting, namely  $M_0$ , leaving behind a purified  $T_1$  map.

Before presenting an example, it would be very useful to state the difference between a  $T_1$ -weighted image and a  $T_1$  map. A  $T_1$ -weighted image is only a snapshot taken at a single point along the recovery process. Therefore, depending on the sampling time, or more formally, the inversion time, the relative tissue contrast can be very different. A  $T_1$  map, on the other hand, is obtained by making use of many  $T_1$ -weighted images. For instance, the default parameter set for the proposed method yields 33  $T_1$ -weighted images per slice to arrive at a single  $T_1$  map. In this regard, the multi-point  $T_1$ -mapping procedure, perhaps, more successfully captures the underlying recovery process than a single-point  $T_1$ -weighted procedure. However, the main disadvantage with the  $T_1$ -mapping procedure is that a large number of images need to be collected in a short time, which places a constraint on how high

the resolution can be. Nevertheless, for some applications such as dynamic imaging, resolution may not possess the highest priority.

Figure 7.1 demonstrates the superiority of the  $T_1$  map in segmenting out a number of anatomical regions. (The segmentation was performed using FSL's segmentation program FAST (51)). Making use of both  $T_1$  weighted images and  $T_1$  maps would perhaps yield a better segmentation result.

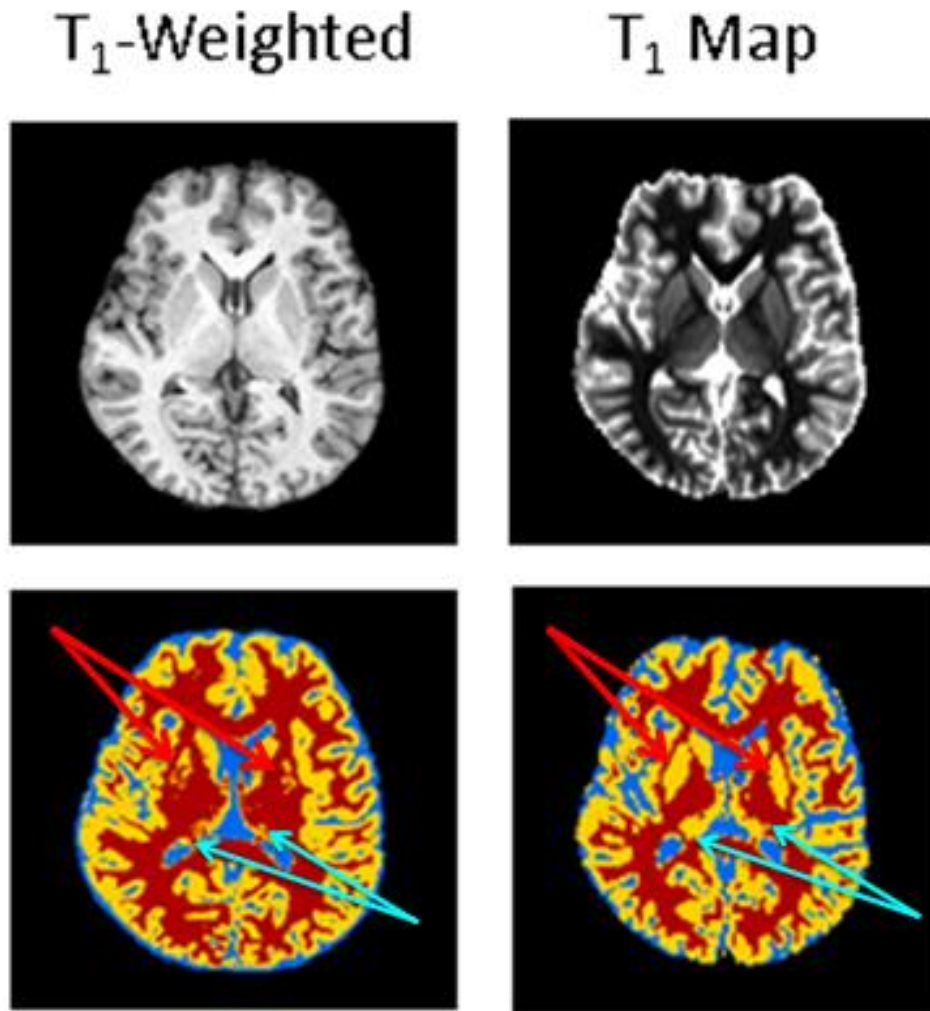


Figure 7.1 – Comparison of segmentation results. Red arrows: Putamen, Cyan arrows: Thalamus

$T_1$  depends on temperature (13). In this respect, temperature mapping is another clinical application. For instance,  $T_1$  mapping can be performed before and after high-SAR MR pulse sequences to monitor the changes in temperature. In order to capture a good quality temperature map,  $T_1$  mapping has to be rapid, and our sequence is therefore a good match for this application.

Finally, motion is always an issue in clinical applications, especially in the case of uncooperative subjects. Thus, our sequence provides a rapid and robust remedy.

### **7.3 Limitations**

One important problem with the current sequence is that, although retrospective reconstruction is useful, the benefits are limited. This is because, for EPI sequences, the sampling bandwidth along the phase encoding axis, typically the anterior-posterior axis, is low, and this leads to geometric distortion. If the subject moves, say, rotates his head by 45 degrees, phase encoding will now take place along an axis that is 45 degrees away from the anterior-posterior axis, which, in turn, changes the direction along which geometric distortion will occur. Some voxels may be relocated, and some of them may split into two or more voxels, affecting intensity, and hence the very measurements used for curve fitting. The images of Subject 4 introduced in Chapter 6 constitute a beautiful example. Figure 7.2 shows what happens when the second saturation recovery volume is rigidly registered onto the first one. It can be clearly seen that the shape of the brain got significantly altered. A better way to deal with motion is, therefore, a prospective correction scheme where the acquisition frame of reference follows the patient frame of reference, keeping the phase encoding direction the same. Siemens has already implemented a prospective acquisition correction scheme that was

previously proposed (52). It may need to be modified to take into account the intensity variations within inversion recovery repetitions to be applicable to our sequence.

Another problem is that, when the subject moves, the relative position of his head changes with respect to the individual elements of the multichannel head coil, introducing a different pattern of receive field inhomogeneity. Figure 7.2 demonstrates this effect very clearly – the anterior portion of the brain appears brighter after motion. The remedy for this issue is bias field removal. The saturation recovery volumes can be used for estimating the bias field at each position, and these estimates can then be utilized for removing the bias from all of the remaining repetitions, taking into account which inversion recovery repetition is assigned to which saturation recovery repetition.

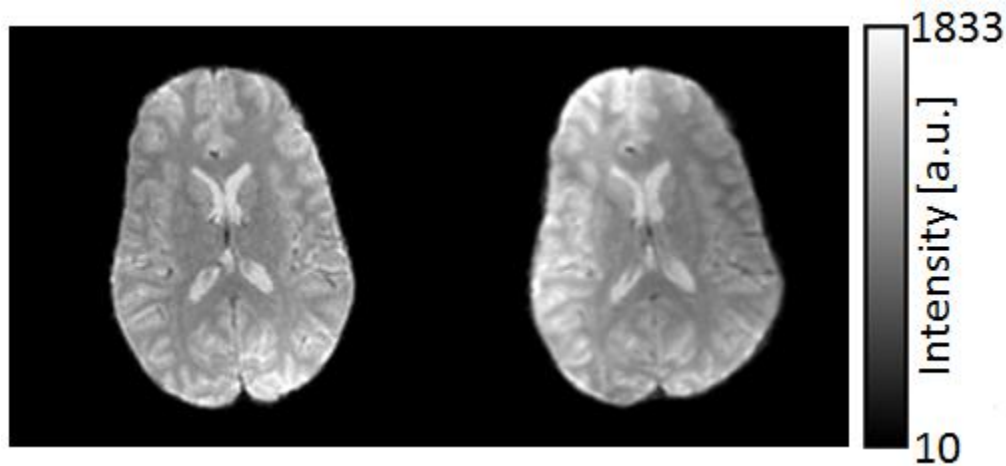


Figure 7.2 – Computation times for Case 1: Motion-corrupted with  $N_{Spins}=1$  (left), Motion-corrupted

One final problem is that the sequence can currently handle, at most, three different positions, because GRAPPA calibration is performed only at three predefined locations. This can be overcome by performing calibration whenever there is motion. The calibration

module should work in cooperation with the prospective acquisition scheme mentioned above.

#### **7.4 Future work**

Future work includes implementing the prospective acquisition correction scheme mentioned in the previous section, performing the calibration scans whenever there is motion, removing the bias field from the images to avoid the negative effects of motion-related changes in the receive field inhomogeneity pattern, and taking under control the random errors occurring during retrospective reconstruction.

## REFERENCES

1. Zhi-Pei “” L, Lauterbur PC. Principles of Magnetic Resonance Imaging: A Signal Processing Perspective: “The” Institute of Electrical and Electronics Engineers Press; 2000.
2. Haacke EM, Brown RW, Thompson MR, Venkatesan R. Magnetic resonance imaging: physical principles and sequence design: Wiley-Liss New York.; 1999.
3. Mansfield P. Multi-planar image formation using NMR spin echoes. *Journal of Physics C: Solid State Physics* 1977;10(3):L55.
4. Bernstein MA, King KF, Zhou XJ. Handbook of MRI pulse sequences: Academic Press; 2004.
5. Pruessmann KP, Weiger M, Scheidegger MB, Boesiger P. SENSE: sensitivity encoding for fast MRI. *Magnetic Resonance in Medicine* 1999;42(5):952-962.
6. Griswold MA, Jakob PM, Heidemann RM, Nittka M, Jellus V, Wang J, Kiefer B, Haase A. Generalized autocalibrating partially parallel acquisitions (GRAPPA). *Magnetic Resonance in Medicine* 2002;47(6):1202-1210.
7. Tofts P. Quantitative MRI of the brain: measuring changes caused by disease: Wiley; 2005.
8. Kaldoudi E, Williams SCR. Relaxation time measurements in NMR imaging. Part I: Longitudinal relaxation time. *Concepts in Magnetic Resonance* 1993;5(3):217-242.
9. Tofts PS. Modeling tracer kinetics in dynamic Gd-DTPA MR imaging. *Journal of Magnetic Resonance Imaging* 1997;7(1):91-101.
10. Larsson HB, Courivaud F, Rostrup E, Hansen AE. Measurement of brain perfusion, blood volume, and blood-brain barrier permeability, using dynamic contrast-enhanced T1-weighted MRI at 3 tesla. *Magnetic Resonance in Medicine* 2009;62(5):1270-1281.
11. Bergamino M, Saitta L, Barletta L, Bonzano L, Mancardi GL, Castellani L, Ravetti JL, Roccatagliata L. Measurement of Blood-Brain Barrier Permeability with T1-Weighted Dynamic Contrast-Enhanced MRI in Brain Tumors: A Comparative Study with Two Different Algorithms. *ISRN Neuroscience* 2013;2013:6.
12. Bottomley PA, Hardy CJ, Argersinger RE, Allen-Moore G. A review of H nuclear magnetic resonance relaxation in pathology: Are T and T diagnostic? *Medical physics* 1987;14:1.
13. Parker DL, Smith V, Sheldon P, Crooks LE, Fussell L. Temperature distribution measurements in two-dimensional NMR imaging. *Medical physics* 1983;10:321.

14. Dickinson RJ, Hall AS, Hind AJ, Young IR. Measurement of changes in tissue temperature using MR imaging. *Journal of computer assisted tomography* 1985;10(3):468-472.
15. Peller M, Reinf HM, Weigel A, Meininger M, Issels RD, Reiser M. T1 relaxation time at 0.2 Tesla for monitoring regional hyperthermia: feasibility study in muscle and adipose tissue. *Magnetic Resonance in Medicine* 2002;47(6):1194-1201.
16. Shin W, Geng X, Gu H, Zhan W, Zou Q, Yang Y. Automated brain tissue segmentation based on fractional signal mapping from inversion recovery Look-Locker acquisition. *NeuroImage* 2010;52(4):1347-1354.
17. Kullberg J, Angelhed JE, Lönn L, Brandberg J, Ahlström H, Frimmel H, Johansson L. Whole-body T1 mapping improves the definition of adipose tissue: Consequences for automated image analysis. *Journal of Magnetic Resonance Imaging* 2006;24(2):394-401.
18. Fleckenstein JL, Archer BT, Barker BA, Vaughan JT, Parkey RW, Peshock RM. Fast short-tau inversion-recovery MR imaging. *Radiology* 1991;179(2):499-504.
19. De Coene B, Hajnal JV, Gatehouse P, Longmore DB, White SJ, Oatridge A, Pennock JM, Young IR, Bydder GM. MR of the brain using fluid-attenuated inversion recovery (FLAIR) pulse sequences. *American journal of neuroradiology* 1992;13(6):1555-1564.
20. Carr HY, Purcell EM. Effects of Diffusion on Free Precession in Nuclear Magnetic Resonance Experiments. *Phys Rev* 1954;94(3):630-638.
21. Gupta RK, Becker ED, Weiss GH. A modified fast inversion-recovery technique for spin-lattice relaxation measurements. *Journal of Magnetic Resonance* (1969) 1980;38(3):447-452.
22. Freeman R, Hill HDW. Fourier Transform Study of Nmr Spin-Spin Relaxation. *J Chem Phys* 1971;55(4):1985-&.
23. Fram EK, Herfkens RJ, Johnson GA, Glover GH, Karis JP, Shimakawa A, Perkins TG, Pelc NJ. Rapid calculation of T1 using variable flip angle gradient refocused imaging. *Magn Reson Imaging* 1987;5(3):201-208.
24. Freeman R, Hill HDW, Kaptein R. An adaptive scheme for measuring NMR spin-lattice relaxation times. *Journal of Magnetic Resonance* (1969) 1972;7(1):82-98.
25. Redpath TW. Calibration of the Aberdeen NMR imager for proton spin-lattice relaxation time measurements in vivo. *Physics in Medicine and Biology* 1982;27(8):1057.
26. Edelstein WA, Hutchison JM, Johnson G, Redpath T. Spin warp NMR imaging and applications to human whole-body imaging. *Physics in Medicine and Biology* 1980;25(4):751.

27. Kurland RJ. Strategies and tactics in NMR imaging relaxation time measurements. I. Minimizing relaxation time errors due to image noise—the ideal case. *Magnetic Resonance in Medicine* 1985;2(2):136-158.
28. Lin MS, Fletcher JW, Donati RM. Two-point T1 measurement: Wide-coverage optimizations by stochastic simulations. *Magnetic Resonance in Medicine* 1986;3(4):518-533.
29. Gowland PA, Leach MO, Sharp JC. The use of an improved inversion pulse with the Spin-Echo/inversion-recovery sequence to give increased accuracy and reduced imaging time for T1 measurements. *Magnetic Resonance in Medicine* 1989;12(2):261-267.
30. Crawley AP, Henkelman RM. A comparison of one-shot and recovery methods in T1 imaging. *Magnetic Resonance in Medicine* 1988;7(1):23-34.
31. Frahm J, Merboldt KD, Hänicke W, Haase A. Stimulated echo imaging. *Journal of Magnetic Resonance (1969)* 1985;64(1):81-93.
32. Haase A, Frahm J. NMR imaging of spin-lattice relaxation using stimulated echoes. *Journal of Magnetic Resonance (1969)* 1985;65(3):481-490.
33. Look DC, Locker DR. Time saving in measurement of NMR and EPR relaxation times. *Review of Scientific Instruments* 1970;41:250.
34. Graumann R, Barfuss H, Fischer H. TOMROP: a sequence for determining the longitudinal relaxation time in magnetic resonance tomography. *Electromedica* 1987;55:67-72.
35. Gowland PA, Leach MO. Fast and accurate measurements of T1 using a multi-readout single inversion-recovery sequence. *Magnetic Resonance in Medicine* 1992;26(1):79-88.
36. Hinson WH, Sobol WT. A new method of computing spin-lattice relaxation maps in magnetic resonance imaging using fast scanning protocols. *Medical physics* 1988;15:551.
37. Brix G, Schad LR, Deimling M, Lorenz WJ. Fast and precise  $T_1$  imaging using a TOMROP sequence. *Magn Reson Imaging* 1990;8(4):351-356.
38. Kay I, Henkelman RM. Practical Implementation and Optimization of One-shot T1 imaging. *Magnetic Resonance in Medicine* 1991;22(2):414-424.
39. Zhang YT, Yeung HN, Carson PL, Ellis JH. Experimental analysis of T1 imaging with a single-scan, multiple-point, inversion-recovery technique. *Magnetic Resonance in Medicine* 1992;25(2):337-343.
40. Ordidge RJ, Gibbs P, Chapman B, Stehling MK, Mansfield P. High-speed multislice T1 mapping using inversion-recovery echo-planar imaging. *Magnetic resonance in*

- medicine: official journal of the Society of Magnetic Resonance in Medicine/Society of Magnetic Resonance in Medicine 1990;16(2):238.
41. Clare S, Jezzard P. Rapid T1 mapping using multislice echo planar imaging. *Magnetic Resonance in Medicine* 2001;45(4):630-634.
  42. Zhu DC, Penn RD. Full-brain T1 mapping through inversion recovery fast spin echo imaging with time-efficient slice ordering. *Magnetic Resonance in Medicine* 2005;54(3):725-731.
  43. Aja-Fernandez S, Tristan-Vega A, Hoge WS. Statistical Noise Analysis in GRAPPA Using a Parametrized Noncentral Chi Approximation Model. *Magnetic Resonance in Medicine* 2011;65(4):1195-1206.
  44. Murphy BW, Carson PL, Ellis JH, Zhang YT, Hyde RJ, Chenevert TL. Signal-to-Noise Measures for Magnetic-Resonance Imagers. *Magn Reson Imaging* 1993;11(3):425-428.
  45. Firbank MJ, Coulthard A, Harrison RM, Williams ED. A comparison of two methods for measuring the signal to noise ratio on MR images. *Physics in Medicine and Biology* 1999;44(12):N261-N264.
  46. Reeder SB, Wintersperger BJ, Dietrich O, Lanz T, Greiser A, Reiser MF, Glazer GM, Schoenberg SO. Practical approaches to the evaluation of signal-to-noise ratio performance with parallel imaging: Application with cardiac imaging and a 32-channel cardiac coil. *Magnetic Resonance in Medicine* 2005;54(3):748-754.
  47. Dietrich O, Raya JG, Reeder SB, Reiser MF, Schoenberg SO. Measurement of signal-to-noise ratios in MR images: Influence of multichannel coils, parallel imaging, and reconstruction filters. *Journal of Magnetic Resonance Imaging* 2007;26(2):375-385.
  48. Detre JA, Leigh JS, Williams DS, Koretsky AP. Perfusion imaging. *Magn Reson Med* 1992;23(1):37-45.
  49. Jenkinson M, Smith S. A global optimisation method for robust affine registration of brain images. *Med Image Anal* 2001;5(2):143-156.
  50. Jenkinson M, Bannister P, Brady M, Smith S. Improved optimization for the robust and accurate linear registration and motion correction of brain images. *NeuroImage* 2002;17(2):825-841.
  51. Zhang YY, Brady M, Smith S. Segmentation of brain MR images through a hidden Markov random field model and the expectation-maximization algorithm. *IEEE Trans Med Imaging* 2001;20(1):45-57.
  52. Thesen S, Heid O, Mueller E, Schad LR. Prospective acquisition correction for head motion with image-based tracking for real-time fMRI. *Magn Reson Med* 2000;44(3):457-465.